NASA Contractor Report 196703

A New Higher-Order Composite Theory for Analysis and Design of High Speed Tilt-Rotor Blades

Thomas Robert McCarthy

CONTRACT NAG2-771
October 1996

National Aeronautics and
Space Administration

NASA Contractor Report 196703

A New Higher-Order Composite Theory for Analysis and Design of High Speed Tilt-Rotor Blades

Thomas Robert McCarthy

Arizona State University
Department of Mechanical and Aerospace Engineering
P. O. Box 876106
Tempe, AZ 85287-6106

Prepared for
Ames Research Center
CONTRACT NAG2-771
October 1996

National Aeronautics and
Space Administration

Ames Research Center
Moffett Field, California 94035-1000

ABSTRACT

A higher-order composite box beam theory is developed to model rectangular beams with arbitrary wall thicknesses. The theory, which is based on a refined displacement field, is a three-dimensional model which approximates the elasticity solution so that the beam cross-sectional properties are not reduced to one-dimensional beam parameters. Both inplane and out-of-plane warping are included automatically in the formulation. The model can accurately capture the transverse shear stresses through the thickness of each wall while satisfying stress free boundary conditions on the inner and outer surfaces of the beam.

Numerical results are presented for beams with different wall thicknesses and aspect ratios. The static results are correlated with available experimental data and show excellent agreement. The dynamic results which are correlated with a general purpose finite element code show the importance of including inplane and out-of-plane warping deformations in the formulation.

The developed beam theory is then used to model the load carrying member of a tilt-rotor blade which has thick-walled sections. A procedure is developed for computing the aeroelastic stability of the tilt-rotor blade based on the composite box beam model. The aerodynamic loads are calculated using the classical blade element momentum theory. Analytical expressions for the lift and drag are obtained based on the blade planform with corrections for the high lift capability of rotor blades. The aerodynamic analysis is coupled with the structural model to formulate the complete coupled equations of motion for aeroelastic analyses.

Finally, a multidisciplinary optimization procedure is developed to improve the aerodynamic, structural and aeroelastic performance of the tilt-rotor aircraft. The objective functions include the figure of merit in hover and the high speed cruise propulsive efficiency. Structural, aerodynamic and aeroelastic stability criteria are imposed as constraints on the problem. The Kreisselmeier-Steinhauser function is used to formulate

the multiobjective function problem and a hybrid approximate analysis is used to reduced the computational effort. The search direction is determined by the Broyden-Fletcher-Goldfarb-Shanno algorithm. The optimum results are compared with the baseline values and show significant improvements in the overall performance of the tilt-rotor blade.

To my parents, Tere and Steve Ross and Joe and Loredana McCarthy.

For supporting me throughout my entire scholastic career,

helping me to make this dissertation a reality.

A special thank you to my girlfriend, Marti Spencer.

For her love and encouragement, especially during the difficult times.

ACKNOWLEDGMENTS

I would like to thank my advisor, Dr. Aditi Chattopadhyay, for investing six years in me to ensure that I became a better researcher. Without her guidance and assistance, this dissertation would not have been. I would also like to thank the other members of my advisory committee, Dr. David H. Laananen, Dr. Marc P. Mignolet, Dr. Subramaniam Rajan and Dr. Robert L. Rankin for taking the time to help me with my research. I also need to thank all of my fellow graduate students, especially Charles E. Seeley, Narayanan S. Pagaldipti and Haozhong Gu. Special thanks to Bruce Tachoir for his unbelievable patience and help for all matters pertaining to computers.

Finally I wish to thank the NASA Ames Research Center for supporting me throughout the entire duration of my doctoral studies through grant numbers, NAG2-771 and NCC2-795, technical monitors, Dr. Sesi Kottapalli and John F. Madden, III. In particular, I wish to thank Dr. Sesi Kottapalli, Dr. William Warmbrodt, John F. Madden, III., William Snyder, Peter Talbot and Joe Totah.

TABLE OF CONTENTS

LIST OF TABLES

LIST OF FIGURES

Figure Page

NOMENCLATURE

A_{ij}	Zeroth order laminate stiffness matrix (lb./in.)
B_{ij}	First order laminate stiffness matrix (lb.)
c	Beam width (in.)
c_l	The sectional coefficients of lift
c_d	The sectional coefficients of and drag
d	Beam height (in.)
D_{ij}	Second order laminate stiffness matrix (lb.-in.)
E_{ij}	Third order laminate stiffness matrix (lb.-in.^{2})
e^o	Zeroth order strain tensor
f	Forcing vector (lb.)
F_{ij}	Fourth order laminate stiffness matrix (lb.-in.^{3})
F_k	Individual objective functions
FM	Hover figure of merit
g_j	Constraint function vector
h	Wall thickness (in.)
H_{ij}	Sixth order laminate stiffness matrix (lb.-in.^{5})
K	Stiffness matrix (lb./in.)
L	Beam length (in.)
M	Mass matrix (slugs)
NC	Number of constraints
NDV	Number of design variables
NF	Number of objective functions
NSEG	Number of blade segments
O_{ij}	Seventh order laminate stiffness matrix (lb.-in.^{6})

P_{ij}	Eighth order laminate stiffness matrix (lb.-in.^{7})
$\mathbf{q}$	Nodal degree of freedom vector
Q_{ij}	Constitutive matrix (p.s.i.)
R	Blade radius (ft.)
r	Radial location (ft.)
$\mathbf{S}$	Nodal displacement relationship matrix
T	Kinetic Energy (lb.-in.)
$\hat{T}_{ij}$	Transformation matrix between the strains
$\hat{t}_1, \hat{t}_2, \hat{t}_3$	Applied surface tractions (lb./in.^{2})
t/c	Thickness to chord ratio
$\mathbf{T}_{ur}$	Transformation matrix between the displacements
U	Strain energy (lb.-in.)
u_1, u_2, u_3	Local displacements (in.)
U_o	Strain energy density (p.s.i.)
u_o, v_o, w_o	Displacements at midplane of walls (in.)
V_∞	Aircraft forward velocity (ft/s)
W	Resultant velocity (ft/s)
W_e	Applied external work (lb.-in.)
X, Y, Z	Global coordinate system
X′, Y′, Z′	Global, rotated coordinate system
$\bar{X}_1, \bar{X}_2, \bar{X}_3$	Body forces (lb./in.^{3})
x, y, z	Local, untwisted coordinate system
x^*, y^*, z^*	Local, twisted, unswept coordinate system
$Y_{a/c}$	Lifting line offset (in.)
α	The effective angle of attack (deg.)

α_a	Physical angle of attack of the blade (deg.)
α_{zl}	Zero lift angle (deg.)
$\mathbf{B}$	Nodal strain relationship matrix
χ, η, ζ	Local, twisted and swept coordinate system
Δ_{ij}^k	Density matrix of kth order
ε	Strain tensor
$\tilde{\varepsilon}_j^o$	Strain in the local, twisted coordinate
Φ	Design variable vector
ϕ	Elastic twist (rad.)
η_{ax}	Rotor propulsive efficiency
$\kappa^1, \kappa^2, \kappa^3$	Higher order strain tensors (1/in., 1/in.^{2} and 1/in.^{3})
$\hat{\Lambda}$	Blade sweep angle (deg.)
Λ	The total inflow angle of the blade section (deg.)
Λ_a	Aerodynamic inflow angle (deg.)
Λ_s	Inflow angle due to blade dynamic effects (deg.)
$\tilde{\mu}_j$	Additional strain components due to pre-twist
θ	Twist by an angle (rad.)
θ_p	Blade twist (deg.)
ρ	Air density (slug/ft^3)
$\hat{\rho}$	K-S function multiplier
σ	Stress tensor (p.s.i.)
υ_i	Blade inflow velocity (ft/s)
u_T	Blade swirl velocity (ft/s)
Ω	Rotor angular velocity (r.p.m.)
ψ_x, ψ_y	Higher-order displacement functions (rad.)

1. Introduction

The tilt-rotor aircraft has become an increasingly viable concept over the last several years [1-4]. The goal is to combine the hover performance of a helicopter in take-off and landing with fixed-wing aircraft like efficiencies in high speed cruise. The aircraft is similar in appearance to conventional fixed-wing aircraft, however, large diameter rotors are tip mounted on the wings. These rotors are mounted on pylon assemblies which are capable of rotation through 90 degrees so that the aircraft can convert between the various flight regimes (e.g. hover, transition and cruise) required of this aircraft (Figs. 1 - 3).

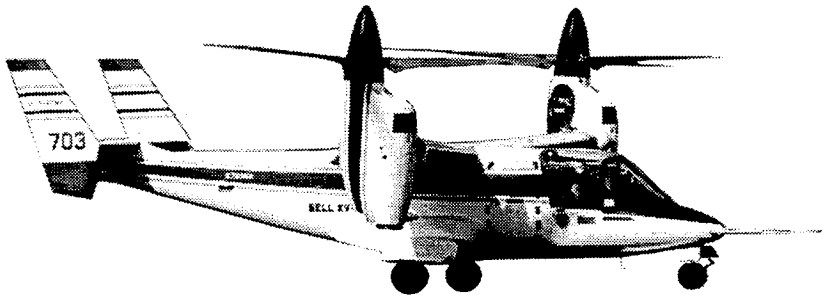

Fig. 1.1 XV-15 tilt-rotor in helicopter mode.

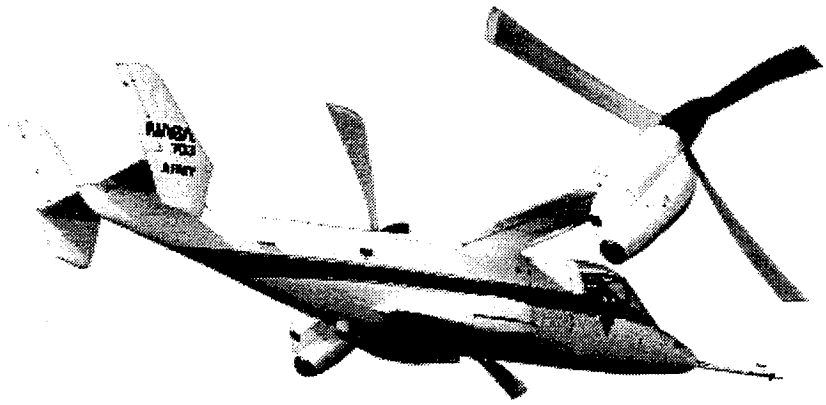

Fig. 1.2 XV-15 tilt-rotor in transition/conversion mode.

There are many design requirements associated with tilt-rotor performance including a low disc loading in the hover configuration and the ability to rotate the rotors forward to achieve cruise speeds up to 450 knots [5]. The problem becomes more complex since in vertical flight and in hover, a large portion of the rotor is directly over the wing which

produces a large downwash effect upon the wing. The downwash effect increases thrust requirement of the aircraft by approximately 10 - 12 percent [6]. Other problems associated with this configuration are related to high helical tip Mach numbers (M_{tip}) which represent a critical performance issue in high speed cruise (350 - 450 knots). Aeroelastic stability is an important consideration in the design of tilt-rotors. Due to the large thrust requirement in hover, the prop-rotors have a much greater radius than standard propellers. This increases the tip speed which in cruise may cause individual blade flutter or a coupled flexible motion between the rotor, wing and pylon known as whirl flutter. Since civil tilt-rotors are required to be stable at a 20 percent margin above their dive speed (defined to be 15 percent larger than the cruise speed), this means that the flutter speed must be larger than 621 knots for a tilt-rotor with a cruise speed of 450 knots.

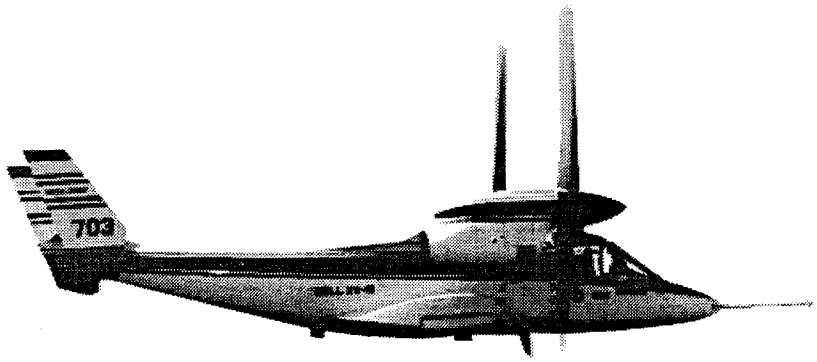

Fig. 1.3 XV-15 in cruise mode.

There are several different techniques which can be used to address these issues. For example, the tip Mach number can be reduced through rotor tip speed reduction or through the use of blade sweep which reduces the effective Mach number. Another alternative is to increase the drag divergence Mach number (M_{dd}) at the tip to values above M_{tip}. This can be accomplished through reductions in the blade thickness. However, each of these options will adversely affect the hover performance, drive system weight or aeroelastic stability of the rotor blade. In the helicopter mode, to maintain a high figure of merit in

hover, the solidity of the blade must be increased since thinner airfoils are used for maintaining efficiency in cruise.

1.1 Tilt-Rotor Design

Due to the many conflicting requirements imposed on prop-rotor performance between hover, conversion and airplane mode, the use of formal numerical optimization techniques is well suited for studying the design trade-offs associated with such aircraft. Although there has been a significant amount of research performed on the optimization of rotary wing aircraft, only very few studies have investigated tilt-rotor design issues. Recently, research efforts have been initiated by Chattopadhyay et al. [7-16] to develop formal optimization techniques to address these issues. In Refs. 7 - 9, optimization procedures were developed to maximize the high speed cruise propulsive efficiency without degrading the hover figure of merit. An optimization procedure was developed in Ref. 10 to address the problem of aeroelastic stability of high speed proprotors. In Ref. 11, the drive system weight was minimized and the associated trade-offs in cruise efficiency were investigated. The integrated aerodynamic, aeroelastic and structural optimization problem was addressed in Ref. 12. A purely aerodynamic multiobjective optimization procedure for improved high speed cruise and hovering performance using planform and airfoil characteristics as design variables was developed by McCarthy et al. [13]. In Refs. 14 and 15, a two level decomposition technique was developed by Chattopadhyay et al. for the combined aerodynamic/structural design of high speed prop-rotor blades. At the upper level, the aerodynamic performance was improved using continuous optimization techniques. The structural performance was improved at the lower level using composite ply orientations a of thin-walled box beam as design variables. More recently, McCarthy and Chattopadhyay [16], developed a procedure for a combined wing/rotor optimization study of high speed tilt-rotors. The analysis was based on comprehensive rotorcraft algorithms and design criteria from both the rotor and the wing were included in the formulation.

1.2 Aeroelastic Stability

Rotor dynamics and aeroelastic response are critical to the design of vertical take-off and landing and short take-off (V/STOL) aircraft. In 1966, Reed [17] described the basic phenomenon of propeller whirl flutter instability for V/STOL aircraft. Since this time, several survey papers have attempted to address the critical issues associated with aeroelastic stability. In 1976, Kvaternik [18] noted that the blade inplane flexibility can have a significant effect on the stability of the system. More recently, Friedmann [19] described the necessary requirements in aeroelastic stability modeling. The significant potential for aeroelastic tailoring from using composite rotors in a comprehensive aeroelastic stability analysis was discussed.

There has also been a significant amount of in depth research efforts to investigate the physics of aeroelastic stability. Edenborough [20] investigated the stability of rotor-pylon configuration for a tilt-rotor aircraft. It was concluded from the study that stable rotor/pylon configuration can be designed for high speed operation. The configuration studied in the paper was modeled analytically up to speeds of 250 knots which was then validated by experimental data up to a speed of about 195 knots. Kaza [21] investigated the effect of steady-state coning angle and damping of the flapping hinge of the blades on the whirl flutter stability boundary. This analytical study was based on one-dimensional beam analysis. More recently, Johnson [22,23] has identified the modeling requirements to accurately predict aeroelastic stability. From these studies it was concluded that an accurate structural representation of the blade is essential to properly model dynamic stability.

Johnson [24] calculated the performance, loads and stability of the XV-15 tilt-rotor and compared the results to wind-tunnel and flight test measurements to assess the requirements for additional experimental data and further analytical development. The basic dynamic problems of advanced rotor system, including aeroelasticity of tilt-rotor blades, was also

investigated by Johnson in Ref. 25. In this study the need for accurate elastic representation of the blade dynamics was established.

1.3 Aeroelastic Tailoring

Due to the fact that aeroelastic stability is critical in the design of rotary wing aircraft, a significant amount of research has been performed investigating aeroelastic tailoring for rotary wing aircraft over the years. The aeroelastic tailoring of composite rotor blades based on the Classical Laminate Theory (CLT) for a thin-walled cylindrical tube was investigated by Mansfield and Sobey [26]. A detailed investigation of aeroelastic stability of helicopter blades was performed by Chopra and Sivaneri [27]. Quasi-steady airloads were used and the equations of motion were linearized using a small perturbation theory. The equations of motion were then solved using a finite element technique based on one-dimensional isotropic beam approach.

The aeroelastic stability of composite helicopter blades was investigated using finite element techniques by Hong and Chopra [28]. The structural element in the blade was modeled as a thin-walled composite box beam. Only axial and inplane shear stresses were included in the formulation. This approach was then modified by the authors to investigate the stability of a bearingless rotor by modeling the rotor flex beam as an I-beam [29].

Rosen and Rand [30] developed a theory which describes the aeroelastic behavior of curved helicopter blades for hovering and axial flight. In this approach, the blade was modeled as a solid, isotropic beam. The control of tilt-rotor flutter was analyzed by Nasu [31] using a rotor model consisting of a straight, fixed wing, a pylon attached to the wing tip and a three-bladed rotor. Each rotor blade had two bending degrees of freedom and one torsional degree of freedom about the elastic axis. Torok and Chopra [32] used a comprehensive rotor aeroelastic analysis to investigate the stability of a hingeless helicopter blade. The aeroelastic response and blade loads of a helicopter blade were investigated by Smith and Chopra [33]. A thin-walled box beam model based on the CLT was used as the

load carrying member of the blade in this study. Using the same structural model, Smith [34] performed a parametric study to investigate composite tailoring effects on helicopter blade vibration and flutter.

The influence of several system design parameters on tilt-rotor aeroelastic stability in high speed cruise was addressed by Nixon using a parametric study [35]. The study indicates that the separation of the beam and torsion frequencies can have a significant effect on the stability of the beam mode. It was also shown that the rotor thrust level has a negligible effect on the stability. This study was later enhanced by the author to investigate possibilities of elastic tailoring using composite rotors [36].

A investigation of aeroelastic stability of an advanced geometry helicopter blade which includes fuselage dynamic effects included in the formulation was performed by Bir and Chopra [37]. The aeromechanical stability of bearingless composite helicopter blade in forward flight was investigated by Tracy and Chopra [38]. Transverse shear effects were included in the formulation although it was assumed that the transverse displacements can be decoupled into bending terms and shear terms. A further assumption made in the study is that the transverse shear forces were equal to zero.

Nonlinear, large amplitude aeroelastic behavior of composite rotor blades was investigated using one-dimensional beam theory by Kim and Dugundji [39]. The nonlinear equations of motion were solved using a Newton-Raphson technique. Yen [40] investigated the effects of the blade tip shape on rotor dynamics and aeroelastic response using a parametric study. Several conflicting requirements were observed including the fact that the blade weight had to be increased in order to achieve reductions in the vibratory behavior. The aeroelastic analysis of a fixed wing and a rotating wing in hover were addressed by Nibbeling and Peters [41] using inflow dynamics and a linear structural model which included only elastic bending and torsion. The main focus of this study was inflow dynamics and the structural model was relatively simplistic in nature. Yuan and

Friedmann [42] used an anisotropic one-dimensional beam model to investigate aeroelastic stability of swept tip composite helicopter blades. A detailed finite element model was required to reduce the three-dimensional behavior of the blade to one-dimensional beam like parameters. Only extensional and transverse shear stresses were included in the formulation.

The use of composite materials also allows tailoring capabilities which can be used to improve the rotor structural and dynamic behavior. Structural tailoring using composite blades has recently been investigated as a means for improving the aeroelastic stability of rotary wing aircraft [33,35,36,42-44]. Parametric studies have been performed to investigate composite tailoring in rotary wing applications in Refs. 33, 35, 36 and 42. Of these, only Refs. 35 and 36 investigate tilt-rotor aircraft. Formal optimization techniques have been developed by Ganguli and Chopra for the optimization of composite rotor blades in helicopters [43,44]. In these studies, continuous values for the ply angles were used as design variables.

Improvements in aeroelastic stability through structural tailoring without consideration of other requirements such as aerodynamic and structural performance can lead to unrealistic designs. These criteria can be effectively addressed using multidisciplinary optimization techniques.

1.4 Structural Modeling

For the tilt-rotor, the combination of the low disk-loading of the prop-rotors and the high inflow ratio (the ratio of axial velocity to rotor tip speed) make the dynamics and aeroelastic response of this configuration unique and more complex than that of a helicopter. It is therefore very important that the issues of individual blade flutter and whirl flutter be addressed very early in the design process. As noted in the literature, this can be accomplished by structurally tailoring the rotor for proper stiffness and elastic couplings in an effort to raise blade frequencies and minimize inplane motions at the rotor hub.

However, in order to adequately model the dynamics and aeroelasticity of tilt-rotors, it is essential that an accurate structural model of the rotor be incorporated into the analysis [23,24]. Since efficient structural modeling of the rotor is key to the overall analysis of the aircraft, research efforts have been initiated to investigate this issue.

1.4.1 Beam theories: Beam theories associated with isotropic materials have been well understood for years and these theories tend to predict the structural and dynamic response quite accurately [45,46]. In recent years, the use of composite materials in rotary wing applications has increased due to the favorable strength-to-weight characteristics of these anisotropic materials. However, beam theories for anisotropic materials are not as well established as they are for isotropic materials. Recently some research has been reported in deriving composite beam theories [47-80].

A complex finite element methodology capable of modeling anisotropic beams with arbitrary cross sections was developed by Wörndle [47]. The method was based on a fully three-dimensional finite element theory in which the cross-sectional warping was superimposed on the assumed displacement field. A comprehensive theory for modeling anisotropic material was developed by Giavotto et al. [48]. In this methodology, the three-dimensional behavior of the beam was reduced to one-dimensional beam like parameters based on a cross-sectional analysis. St. Venant type warping was superimposed on the assumed displacement field.

Krenk and Gunneskov [49] formulated a theory for pre-twisted turbine blades which included finite shear flexibility. The pre-twist was accounted for, in this theory, through the axial derivative of the St. Venant warping function and the shear stresses were decoupled into torsion and shear contributions. Using this approach, the shear flexibility could only be approximated in blades with moderate wall thicknesses.

Another beam theory for anisotropic materials was due to Bauchau [50]. Out-of-plane warping was included in the formulation but the model assumed that each section was

infinitely rigid in its own plane, therefore inplane warping was neglected. The out-of-plane warping was based on so-called "eigenwarping functions" which was an improvement to the St. Venant warping. Only the axial strain and torsional related shear strain were included in the formulation. The theory was extended by the author to include the large displacement analysis of naturally curved and twisted composite beams [51]. Although shearing deformations and torsion related warping were included in this formulation, it was assumed that the cross sections do not deform in their own plane. Further, the beam theory was only derived for thin-walled beams.

The static and dynamic behavior of helicopter blades using a finite element approach was addressed by Bauchau and Hong [52]. This study represented a first step towards developing a complete aeroelastic analysis. However, the theory used in this report was based on the Classical Laminate Theory which is valid only for thin-walled beams. Bauchau and Hong later developed a nonlinear composite beam theory to model helicopter rotor blades [53]. The modeling included arbitrarily large displacements and rotations but assumed small strains. Although warping effects were included, only the axial strain and the inplane and transverse shear strain appeared in the formulation. Shearing and warping deformations were investigated by Bauchau et al. [54] for a thin-walled composite sandwich beam and were compared with experimental data. The study once again assumed thin-walled sections.

A nonlinear analysis of pre-twisted rods was developed by Rosen et al. [55]. Small strains were assumed in the formulation. This theory was later extend for modeling the dynamics of moving and rotating rods [56-57]. Large deformations were included in the formulation. A finite element model for the analysis of composite box beams was developed by Stemple [58]. The warping function, in this formulation, was assumed to be only out-of-plane and it was superimposed upon a displacement field consisting of three translations and three rotations. The warping was determined based upon a two-

dimensional cross-sectional analysis. The results from this theory have been shown to be as accurate as a full three-dimensional solution for thin-walled box beams [59].

Standard means of representing finite rotation in rigid-body kinematics, including orientation angles, Euler parameter and Rodrigues parameters were reviewed and compared by Hodges [60]. General kinematical relations for a beam which include moderate rotations were presented. Hinnant and Hodges [61] used a finite element methodology, which included geometric nonlinearities, to obtain results for a cantilevered beam with a tip mass which were compared to experimental values. A nonlinear formulation for the dynamics of initially curved and twisted beams in a moving frame was presented by Hodges [62]. Both inplane and out-of-plane St. Venant warping displacements were assumed. The three-dimensional beam behavior was reduced to one-dimensional beam parameters and only unrestrained warping effects were included in the formulation. Rehfield et al. [63] investigated the nonclassical behavior of thin-walled composite beams with closed cross sections. The nonclassical behavior refers to elastic bending-shear coupling and restrained torsional warping. A decay length parameter was defined which approximates the effects of the restrained warping.

Several refined composite beam theories based on the Variational Asymptotical method [64] have been developed by Hodges et al. [65-70]. The variational asymptotical method is a mathematical technique by which the three-dimensional analysis of the composite beam deformation can be split into a linear, two-dimensional cross-sectional analysis and a nonlinear, one-dimensional analysis. An ordering scheme is required to identify "small" terms which are then eliminated from the strain energy formulation. The method requires the energy functional to be expanded in terms of a small parameter and the theory is therefore truly only valid for thin-walled beams.

An analytical model was developed by Kosmatka [71] for assessing the extension-bending-torsion coupling effects associated with anisotropic beams having non

homogeneous irregular cross sections and initial twist. The model was based on beam theory which reduces the three-dimensional behavior to one-dimensional beam equations based on a cross-sectional analysis. The vibration analysis of composite turbopropellers using a nonlinear beam-type finite element approach was studied by Kosmatka and Friedmann [72]. Constitutive relations were obtained by setting the three stresses within the cross section equal to zero, thus assuming that the cross section is rigid in its own plane. In Ref. 73, an analytical model was presented by Kosmatka and Dong for determining the displacement and stress distributions of the St. Venant extension, bending, torsion and flexural problem for prismatic, anisotropic beams of arbitrary cross sections. The problem was reduced to a state of plane stress. However, using this approach a finite element analysis must be performed for each unique cross section before the beam equations of motion can be solved. The behavior of a tip-loaded cantilever beam with an arbitrary cross section was investigated by Kosmatka using a power series solution for the out-of-plane flexural and torsional warping [74,75]. For complex cross sections, the warping results represented a best fit approximation to the exact St. Venant warping function. A beam theory based on a first-order displacement field with superimposed warping functions was used in the formulation which requires a complex two-dimensional finite element analysis of the cross section.

A theoretical modeling of slender composite rotating beams was developed by Rand [76,77]. In addition to the classical degrees of freedom used in this theory, a three-dimensional warping field was superimposed on the displacement field. The developed theory is only valid for thin-walled structures. The author extended this theory to include a nonlinear formulation and a finite difference based numerical solution to investigate the structural behavior of solid orthotropic beams of arbitrary cross sections [78]. Kalfon and Rand [79] developed a theory for the nonlinear modeling of thin-walled composite helicopter blade. Inplane warping was neglected in this formulation.

A free vibration analysis of composite I-beams with elastic couplings under rotation was presented by Chandra and Chopra [80]. The developed theory was a linear analysis based on Vlasov theory. Constrained warping and transverse shear effects were included. A quasi-analytical method for the evaluation of composite box beams has also been developed by Smith and Chopra [59]. The cross-sectional analysis in the theory was performed analytically to reduce the problem to a one-dimensional beam problem which was solved using the finite element method. The cross-sectional analysis was based on the Classical Laminate Theory (CLT). The out-of-plane warping used in the formulation was determined using a contour analysis. Due to the many simplifying assumptions associated with this theory, this approach must be restricted to use as a preliminary design tool.

Among the theories presented above, the more comprehensive anisotropic theories rely upon a full three-dimensional finite element solution which can become very computationally intensive [47,48]. References [49,55-57,60-62,83,74,75,78] address comprehensive modeling of beams with solid cross sections. All of the closed section analysis procedures are based on thin-wall assumptions [50-54,58,59,63,65-73,76,77,79] which is not an adequate assumption when modeling the load carrying structures of tilt-rotor blades. It must be also be noted that when traditional beam analyses are performed in which the three-dimensional behavior of the structure is reduced to one-dimensional beam like parameters [50-54,58,59,63,65-73,76,77,79,80] (e.g. extension and three rotations), it is necessary to perform the cross-sectional analysis at each unique cross section. In many of the formulations presented above, this cross-sectional analysis may require several thousand degrees of freedom. As a result, this type of modeling can become quite complex and computationally intensive for beams which have arbitrary spanwise distributions. Further, many assumptions are made about the warping distributions assumed in these theories. As a result, the beam warping is typically determined in a manner such that the

average warping over the cross section is equal to zero. This, however, does not satisfy the condition of stress free boundary conditions on the surfaces of the beam.

1.4.2 Composite plate theories: In all of the previously developed closed-section beam models, some type of thin-walled assumption is made. However, the composite spar typically used in tilting prop-rotor configurations, e.g. the Advanced Technology Blades (ATB's), have thicker wall sections which makes such models incapable of properly modeling these beams. Therefore, the need for a more general theory for adequate analysis of such sections is obvious. A composite box beam theory which can model sections with arbitrary thicknesses is, of course, more accurate as well as more realistic, since it eliminates all the uncertainties associated with the aforementioned assumptions.

An objective of the present study is to develop a beam theory in which the three-dimensional behavior of the composite structure is not reduced to one-dimensional beam like parameters. By decomposing the beam into the individual walls which make up the beam, a beam theory is developed in which the solution approximates the exact three-dimensional elasticity solution. Further, the warping of the beam is determined in a manner such that the stress free boundary conditions on the inner and the outer surfaces of the beam will be automatically satisfied. To adequately model thick-walled structures, it is necessary to utilize an appropriate composite laminate theory in each of the walls. Several such theories are discussed below.

As a first approximation to a more refined displacement field, first-order shear correction theories and other approximate techniques have been proposed. A first-order shear deformation theory (FST) was developed for general anisotropic laminated plates by Whitney and Pagano [81]. This theory introduces a constant shear correction term and the displacement field does not satisfy the necessary stress free boundary conditions on the upper and lower surfaces of the laminate. Despite the approximate nature of the theory, results for moderately thick plates were found to be more accurate than the Classical

Laminate Theory (CLT). Reissner [82] developed variational principles for deriving the plate equations from three-dimensional elasticity based on first-order shear deformation theories.

A reliable six-node triangle plate/shell element was developed by Kosmatka [83] for the analysis of laminated composite structures based on the first-order shear deformation theory. Bhumbla et al. [84] used the first-order shear deformation theory to predict the free vibration frequencies and mode shapes of spinning laminated composite plates. The results from the study indicate that the Classical Laminate Theory over predicts the stiffness and natural frequencies. The authors later extended this work to study the buckling speed of spinning, laminated composite plates offset from the axis of rotation [85].

Rehfield and Valisetty [86,87] formulated a simple theory for the bending and stretching of homogeneous plates. In this theory the classical assumption that the transverse normal strain and the two transverse shear strains are set to zero was replaced with a hypothesis that the statically equivalent stresses obtained from CLT can be used to estimate the transverse normal strain and transverse shear strains.

The variational asymptotical approach was used by Hodges et al. [88-90] to decompose the three-dimensional plate problem into a linear through-the-thickness, one-dimensional analysis to obtain plate elastic constants and a two-dimensional analysis to analyze plate deformations. Although the possibility of large deflections and rotations was considered, small strains were assumed in the formulation. The variational asymptotical method expands the strain energy in Taylor series expansion based on a small parameter, defined to be the thickness of the plate in this case, and as a result the application of the theory was confined to thin plates.

It has long been recognized that higher-order theories are adequate for modeling composite laminates with arbitrary thicknesses. A third-order theory which includes the transverse normal stress was developed by Lo et al. [91]. The developed general theory

was compared to exact elasticity equations and showed excellent correlation. However, the retention of transverse normal shear stress terms introduces a significant amount of complexity to the formulation. An alternative higher-order composite laminate theory was developed by Reddy [92] in which the transverse shear effects were included, but the transverse normal stress was neglected. In this third-order theory, unlike first-order theories, the stress free boundary conditions were exactly satisfied on the upper and lower surfaces of the plate. This relatively simple theory, which has only two additional unknown functions from the Classical Laminate Theory or the first-order shear deformation theory, has been shown to be extremely accurate when compared to exact elasticity solutions for thick plates [93]. In a subsequent review of all third-order, two-dimensional theories for plates, it was shown by Reddy that all third-order theories developed over the last two decades are based on the same displacement field [94]. The third-order theory due to Reddy [92] was compared with a first-order shear deformation theory and the Classical Laminate Theory, for cross-ply laminates with various boundary conditions, in a study performed by Khdeir et al. [95]. It was found that the third-order theory out performed both the first-order theory and the CLT.

Murakami [96] introduced the concept of superimposing a zig-zag linear function upon a FST to improve the accuracy of inplane responses. The theory was shown to be very accurate, but in this layerwise approach the number of unknown functions was directly proportional to the number of composite plies. As a result, the technique was computationally expensive. This work was later extended by Toledano and Murakami [97] such that the piecewise linear continuous displacements were superimposed upon a quadratic transverse shear stress distribution. In another study performed by the authors [98], a zig-zag shape function was superimposed on Legendre polynomials to approximate the inplane displacement contributions across the plate thickness. Like the original study,

these theories are dependent on the number of plies and are therefore computationally expensive.

A similar study was performed by Cho and Parmerter [99,100] in which a higher-order plate theory for composite laminates was obtained by superimposing a cubic varying displacement field over a zig-zag linearly varying displacement. In this theory, Heaviside functions were used to ensure continuity of the transverse shear stresses at the interface between the laminae. The results, however, were not shown to be more accurate than traditional third-order theories. Robbins and Reddy [101] developed a procedure for the modeling of thick composites using a layerwise laminate theory. The resulting layerwise finite element model used in this theory was capable of computing interlaminar stresses and other localized effects as accurately as three-dimensional finite element models. However, the number of degrees of freedom required in this model was approximately the same as a full three-dimensional finite element model and a result, the layerwise theory was computationally intensive.

Chattopadhyay and Gu developed a new higher-order laminate theory for the modeling of delamination buckling of composite plates and shells [102,103]. Delaminations between layers of composite plates were modeled by jump discontinuity conditions at the delaminated interfaces. These discontinuities were modeled in both the lower and higher-order terms of displacements using Heaviside step functions. Excellent correlation with experimental results was obtained. An exact elasticity solution was presented by Chattopadhyay and Gu [104] for the buckling of simply supported orthotropic plates. The solutions presented in the theory indicated that the third-order theory was the most accurate plate theory with less than eight percent error in all cases, while the Classical Laminate Theory was the least accurate theory with errors of more than 100 percent for thick laminates.

1.4.3 Extension of plate theories for beam modeling: No effort has been reported in using such higher-order composite plate theories in modeling composite box beams. The reason being the complexity of the process, especially when pre-twist and taper are included in the formulation as they are in the present approach. In the present research, the refined displacement field of Reddy [92] is used to analyze the individual walls of a composite box beam. As a result, the developed theory is capable of modeling box beams with arbitrary wall thicknesses. By decomposing the beam in this manner, the developed theory is an approximation to the three-dimensional elasticity solution. Therefore, there is no reduction of the box beam behavior to one-dimensional beam like parameters. Thus, several simplifying assumptions are avoided.

2. Objectives

The objective of this research is to develop a more general, but computationally efficient, theory for the adequate analysis of composite box beam sections with moderately thick walls. A refined higher-order displacement field is used to accurately represent the transverse shear stress distributions in composite laminates of arbitrary thickness which represent the box beam walls. The procedure developed is capable of analyzing composite box beam sections with pre-twist, taper and sweep to model load carrying structural members used in aerospace applications. Unlike previous beam theories, the present theory approximates the three-dimensional elasticity solution rather than reducing the beam properties to one-dimensional quantities. Further, the warping of the cross section in this theory is determined such that stress free boundary conditions are exactly satisfied on the inner and the outer surfaces. As a result, the model is capable of accurately describing thick-walled load-carrying members typically found in tilt-rotor blades such as the Advanced Technology Blades (ATB) on the XV-15 tiltrotor [102,103]. The developed beam model is general enough for applications to a wide range of wing and rotor blade sections.

Next, the box beam model is used to represent the principal load carrying member in a tilt-rotor blade and an aeroelastic analysis is performed. The aerodynamic loading is obtained through an analysis based on a two-dimensional blade element momentum theory [104]. The coupled equations of motion are solved to determine the structural response, the aeroelastic stability and the aerodynamic performance of the trimmed rotor.

Finally, a formal multidisciplinary optimization procedure is developed to investigate the trade-offs associated with aeroelastic stability, aerodynamic and structural design requirements of prop-rotors. The optimization procedure developed can be coupled with other analysis codes being used by the industry allowing trade-off studies to be performed during both preliminary and detailed design stages of the tilt-rotor aircraft development.

The objectives of the proposed research are summarized below.

1. Development and validation of a higher-order composite beam theory capable of modeling box beams of arbitrary shape and wall thicknesses. The theory is capable of modeling short aspect ratio beams with pre-twist, taper and sweep.

2. Development of the coupled aerodynamic and structural equations of motion to investigate aeroelastic stability and blade structural response.

3. Development of a multidisciplinary optimization procedure which includes formal multiobjective formulation technique and an approximate analysis technique based on hybrid expansions.

4. Optimization for multiple flight conditions to investigate the effects of composite tailoring on the overall performance of high speed prop-rotor blades.

3. Composite Structural Modeling

The box beam is modeled using composite laminates to represent the four walls (Fig. 3.1). Several different coordinate systems are used throughout this paper and are defined as follows. The global coordinate system (X, Y, Z) is the untwisted coordinate system located on the axis of rotation (Figs. 3.1 and 3.2). The global, rotated coordinate system (X′, Y′, Z′) represents the coordinate system obtained by rotating the global coordinate system about the axis of twist by an angle $\theta(x)$. In addition, there are three more coordinate systems defined locally in each wall of the box beam. The local, untwisted coordinate system of the i-th wall is defined by (x_i, y_i, z_i). The local, twisted wall coordinate system for the i-th wall which results from the global rotation (θ) of the beam is denoted (x_i^*, y_i^*, z_i^*) as depicted in Figs. 3.3 and 3.4. The introduction of sweep adds complexity to the formulation. For this model, sweep is defined to be in the X′-Y′ plane (Fig. 3.5). The horizontal walls are parallel to this plane and as a result, no

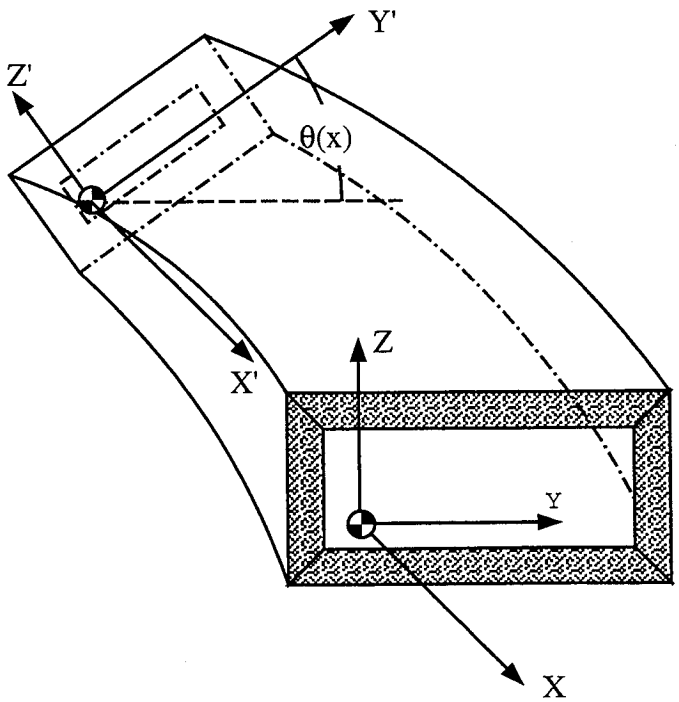

Fig. 3.1 Composite box beam.

additional coordinate system needs to be introduced for these walls. In the vertical walls, however, the sweep is normal to the walls and therefore an additional coordinate system must be introduced. This local, twisted and swept coordinate system is defined by (χ_i, η_i, ζ_i). (Note that in case of the horizontal walls the coordinate system defined by (χ_i, η_i, ζ_i) is identical to the coordinate system defined by (x_i^*, y_i^*, z_i^*).) Detailed explanations of the transformations between the coordinate systems are presented in Appendix A.

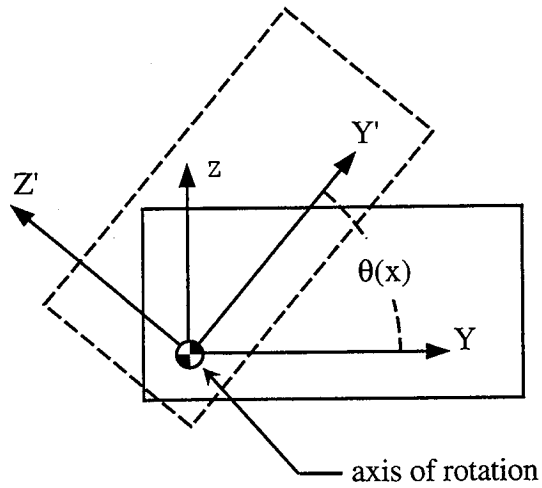

Fig. 3.2 Beam cross section and axis of rotation.

3.1 Refined Displacement Field

A higher-order theory [92] is used to define the displacement field for each wall in the local, twisted and swept coordinate system (χ, η, ζ) as follows. The subscript 'i' has been omitted for convenience throughout the remainder of the study.

$$\tilde{u}_1(\chi,\eta,\zeta) = u_o(\chi,\eta) + \zeta\left(-\frac{\partial \tilde{u}_3(x,\eta)}{\partial \chi} + \psi_x(\chi,\eta)\right) + \zeta^2\phi_x(\chi,\eta) + \zeta\gamma_x(\chi,\eta) \tag{3.1a}$$

$$\tilde{u}_2(\chi,\eta,\zeta) = v_o(\chi,\eta) + \zeta\left(-\frac{\partial \tilde{u}_3(\chi,\eta)}{\partial \eta} + \psi_y(\chi,\eta)\right) + \zeta^2\phi_y(\chi,\eta) + \zeta\gamma_y(\chi,\eta) \tag{3.1b}$$

$$\tilde{u}_3(\chi,\eta) = w_o(\chi,\eta) \tag{3.1c}$$

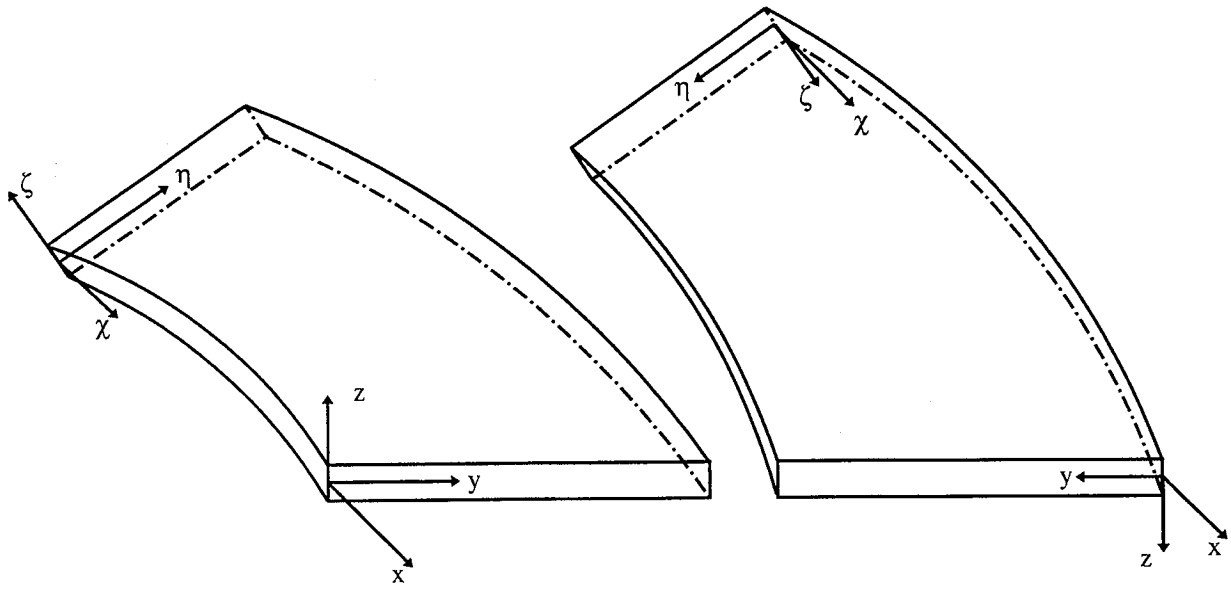

Top wall Bottom wall

Fig. 3.3 Horizontal wall coordinate systems.

where u_o, v_o and w_o represent the displacements at the midplane of each plate and ψ_x and ψ_y represent the rotations of the normals to the midplane. The beam warping in each plate is represented by the functions ϕ_x, ϕ_y, γ_x and γ_y. The local wall deformations $(\tilde{u}_1, \tilde{u}_2, \tilde{u}_3)$ in the twisted coordinate system are related to local deformations (u_1, u_2, u_3) in the untwisted coordinate system (x, y, z) through the following relationship.

$$\begin{Bmatrix} u_1 \\ u_2 \\ u_3 \end{Bmatrix} = \begin{bmatrix} 1 & 0 & 0 \\ 0 & \cos\theta & -\sin\theta \\ 0 & \sin\theta & \cos\theta \end{bmatrix} \begin{Bmatrix} \tilde{u}_1 \\ \tilde{u}_2 \\ \tilde{u}_3 \end{Bmatrix}$$

or

$$\mathbf{u} = \mathbf{T}_{ur}\tilde{\mathbf{u}} \tag{3.2}$$

where $\mathbf{T}_{ur}$ is the transformation matrix between the local, twisted displacements and the local, untwisted displacements. The local deformations in each of the plates (u_1, u_2, u_3) are related to the global deformations (u, v, w) as follows (Figs. 3.1, 3.3 and 3.4).

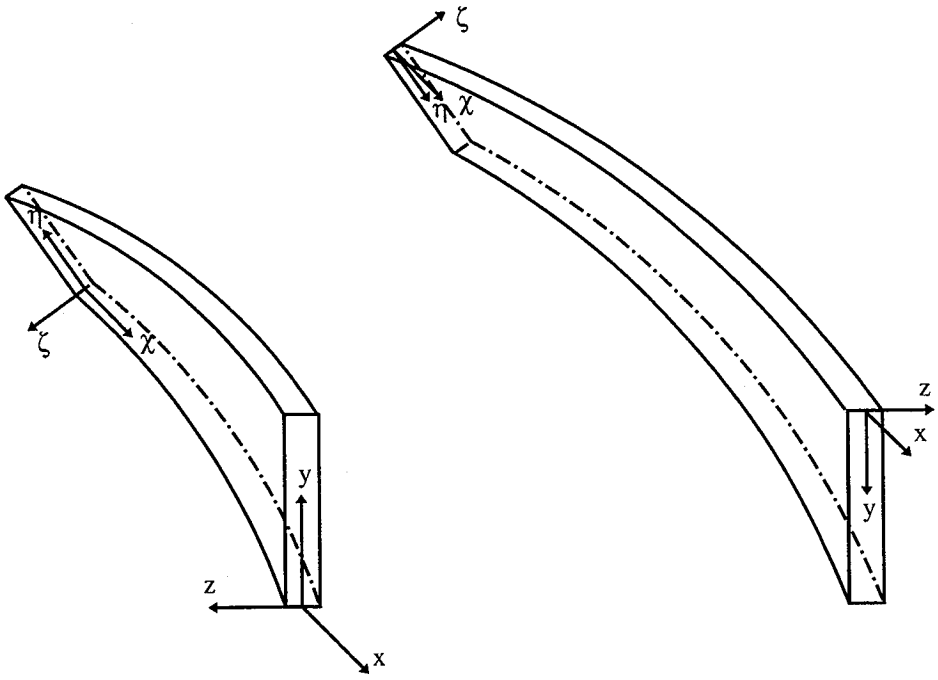

Fig. 3.4 Vertical wall coordinate systems.

$$\left.\begin{aligned} u(X,Y,Z) &= u_1(x,y,z) \\ v(X,Y,Z) &= -u_2(x,y,z) \\ w(X,Y,Z) &= -u_3(x,y,z) \end{aligned}\right\} \quad \forall \quad \{X, Y(y,z), Z(y,z)\} \qquad \textit{wall 1} \qquad (3.3a)$$

$$\left.\begin{aligned} u(X,Y,Z) &= u_1(x,y,z) \\ v(X,Y,Z) &= -u_3(x,y,z) \\ w(X,Y,Z) &= u_2(x,y,z) \end{aligned}\right\} \quad \forall \quad \{X, Y(y,z), Z(y,z)\} \qquad \textit{wall 2} \qquad (3.3b)$$

$$\left.\begin{aligned} u(X,Y,Z) &= u_1(x,y,z) \\ v(X,Y,Z) &= u_2(x,y,z) \\ w(X,Y,Z) &= u_3(x,y,z) \end{aligned}\right\} \quad \forall \quad \{X, Y(y,z), Z(y,z)\} \qquad \textit{wall 3} \qquad (3.3c)$$

$$\left.\begin{aligned} u(X,Y,Z) &= u_1(x,y,z) \\ v(X,Y,Z) &= u_3(x,y,z) \\ w(X,Y,Z) &= -u_2(x,y,z) \end{aligned}\right\} \quad \forall \quad \{X, Y(y,z), Z(y,z)\} \qquad \textit{wall 4} \qquad (3.3d)$$

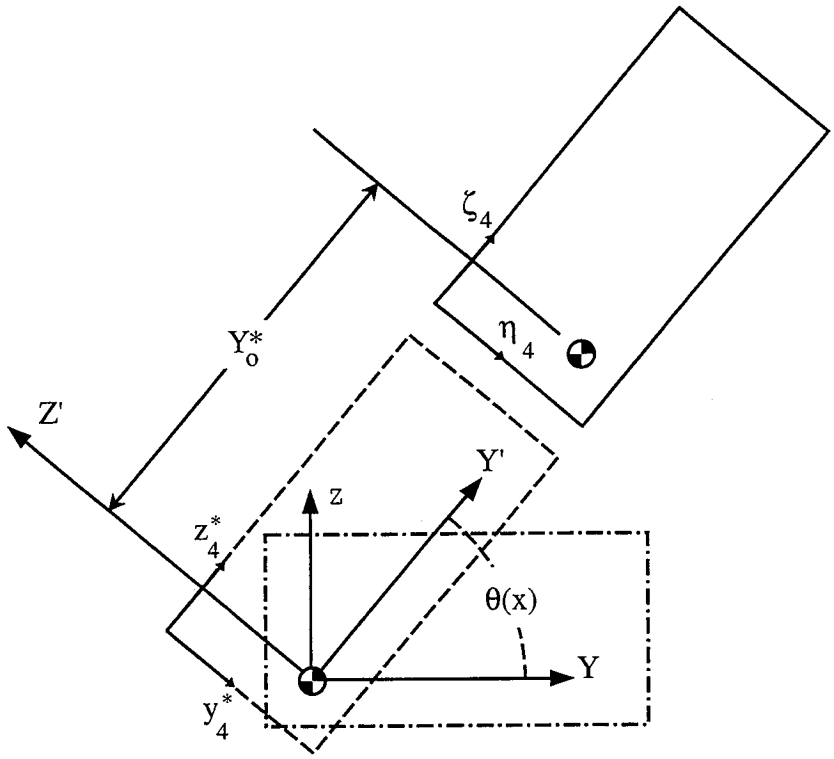

Fig. 3.5 Swept and twisted beam cross section.

3.2 Boundary Conditions

It is necessary to satisfy shear stress free boundary conditions at each free surface of the beam. This implies that in each wall, the shear stresses must be zero on both the outer and the inner surfaces. The imposition of these boundary conditions allow some of the higher-order terms to be determined in terms of some lower-order terms. This procedure, which is explained next, reduces the number of unknowns in the displacement field (Eqns. 3.1). For each wall, the stress free boundary conditions are stated as

$$\sigma_{\chi\zeta}(\chi, \eta, \zeta = \pm h/2) = 0, \tag{3.4}$$

$$\sigma_{\eta\zeta}(\chi, \eta, \zeta = \pm h/2) = 0, \tag{3.5}$$

where h is the total wall thickness. For composite laminates made up of layers of orthotropic lamina, the above requirements imply that the corresponding strains must be zero on these surfaces. That is,

$$\varepsilon_{\chi\zeta}(\chi, \eta, \zeta = \pm h/2) = 0, \tag{3.6}$$

$$\varepsilon_{\eta\zeta}(\chi, \eta, \zeta = \pm h/2) = 0, \tag{3.7}$$

where

$$\varepsilon_{\chi\zeta} = \frac{\partial \tilde{u}_1}{\partial \zeta} + \frac{\partial \tilde{u}_3}{\partial \chi} = \psi_x + 2\zeta\phi_x + 3\zeta^2\gamma_x = 0, \tag{3.8}$$

$$\varepsilon_{\eta\zeta} = \frac{\partial \tilde{u}_2}{\partial \zeta} + \frac{\partial \tilde{u}_3}{\partial \eta} = \psi_y + 2\zeta\phi_y + 3\zeta^2\gamma_y = 0. \tag{3.9}$$

This yields the following relationships

$$\phi_x = 0, \tag{3.10a}$$

$$\gamma_x = -\frac{4}{3h^2}\psi_x, \tag{3.10b}$$

and

$$\phi_y = 0, \tag{3.11a}$$

$$\gamma_y = -\frac{4}{3h^2}\psi_y. \tag{3.11b}$$

Using these conditions (Eqns. 3.10 - 3.11), the individual plate displacement fields (Eqns. 3.1) are now written as

$$\tilde{u}_1 = u_o + \zeta\left(-\frac{\partial w_o}{\partial \chi} + \psi_x\right) - \frac{4}{3h^2}\zeta^3\psi_x, \tag{3.12a}$$

$$\tilde{u}_2 = v_o + \zeta\left(-\frac{\partial w_o}{\partial \eta} + \psi_y\right) - \frac{4}{3h^2}\zeta^3\psi_y, \tag{3.12b}$$

$$\tilde{u}_3 = w_o, \tag{3.12c}$$

where the functions u_o, v_o, w_o, ψ_x and ψ_y represent unknown functions of χ and η.

3.3 Stress - Strain Relations

Due to the fact that the stress and strain tensors are symmetric there are only six unique values of these quantities. Therefore, the following notation is used to define the stress and strain tensors in the local, untwisted coordinate system.

$$\begin{Bmatrix}\sigma_1\\ \sigma_2\\ \sigma_3\\ \sigma_4\\ \sigma_5\\ \sigma_6\end{Bmatrix}^T = \begin{Bmatrix}\sigma_{xx}\\ \sigma_{yy}\\ \sigma_{zz}\\ \sigma_{yz}\\ \sigma_{xz}\\ \sigma_{xy}\end{Bmatrix}^T \quad \text{and} \quad \begin{Bmatrix}\varepsilon_1\\ \varepsilon_2\\ \varepsilon_3\\ \varepsilon_4\\ \varepsilon_5\\ \varepsilon_6\end{Bmatrix}^T = \begin{Bmatrix}\varepsilon_{xx}\\ \varepsilon_{yy}\\ \varepsilon_{zz}\\ 2\varepsilon_{yz}\\ 2\varepsilon_{xz}\\ 2\varepsilon_{xy}\end{Bmatrix}^T \tag{3.13a,b}$$

The stress and strain tensors in the local, twisted and swept coordinate system are expressed similarly. The generalized Hooke's law is used to relate the stresses and the strains. Assuming the products of the derivatives of the displacements to be small in the strain formulation and using Eqn. 3.2, the strains in the local, untwisted coordinate system are expressed as

$$\begin{Bmatrix}\varepsilon_1\\ \varepsilon_2\\ \varepsilon_3\\ \varepsilon_4\\ \varepsilon_5\\ \varepsilon_6\end{Bmatrix} = \begin{Bmatrix}\tilde{u}_{,x}\\ \tilde{v}_{,y}c\theta - \tilde{w}_{,y}s\theta\\ \tilde{v}_{,z}s\theta + \tilde{w}_{,z}c\theta\\ \tilde{v}_{,z}c\theta + \tilde{v}_{,y}s\theta + \tilde{w}_{,y}c\theta - \tilde{w}_{,z}s\theta\\ \tilde{u}_{,z} + \tilde{v}_{,x}s\theta + \tilde{w}_{,x}c\theta + \tilde{v}\,c\theta\,\theta_{,x} - \tilde{w}\,s\theta\,\theta_{,x}\\ \tilde{u}_{,y} + \tilde{v}_{,x}c\theta - \tilde{w}_{,x}s\theta - \tilde{v}\,s\theta\,\theta_{,x} - \tilde{w}\,c\theta\,\theta_{,x}\end{Bmatrix}. \tag{3.14}$$

In the above expressions, the short hand notations $c\theta$ and $s\theta$ are used to denote $\cos\theta$ and $\sin\theta$, respectively. It is important to note, however, that the displacement equations (Eqn. 3.1) are written in the local, twisted and swept coordinate system. The relationship between the derivatives in the local, untwisted coordinate system and the local, twisted and swept coordinate system are written as

$$\frac{\partial}{\partial x} = \frac{\partial}{\partial \chi} + (\zeta - Z_o)\theta_{,x}\frac{\partial}{\partial \eta} - \left[(\eta - Y_o)\theta_{,x} + z^*_{o,x}\right]\frac{\partial}{\partial \zeta}, \tag{3.15a}$$

$$\frac{\partial}{\partial y} = \cos\theta \frac{\partial}{\partial \eta} - \sin\theta \frac{\partial}{\partial \zeta}, \tag{3.15b}$$

$$\frac{\partial}{\partial z} = \sin\theta \frac{\partial}{\partial \eta} + \cos\theta \frac{\partial}{\partial \zeta}. \tag{3.15c}$$

Details of the transformation relationship between the coordinate systems are found in Appendix A. Using Eqns 3.1, 3.14 and 3.15, the strains are written as follows.

$$\begin{aligned}\varepsilon_1 = {} & u_{o,\chi} + \zeta\left(-w_{o,\chi\chi} + \psi_{x,\chi}\right) - \frac{4}{3h^2}\zeta^3\psi_{x,\chi} \\ & + \left\{u_{o,\eta} + \zeta\left(-w_{o,\chi\eta} + \psi_{x,\eta}\right) - \frac{4}{3h^2}\zeta^3\psi_{x,\eta}\right\}(\zeta - Z_o)\,\theta_{,x} \\ & - \left\{\left(-w_{o,\chi\eta} + \psi_{x,\eta}\right) - \frac{4}{h^2}\zeta^2\psi_{x,\eta}\right\}\left[(\zeta - Z_o)\,\theta_{,x} + z^*_{o,x}\right]\end{aligned} \tag{3.16a}$$

$$\begin{aligned}\varepsilon_2 = {} & \left\{v_{o,\eta} + \zeta\left(-w_{o,\eta\eta} + \psi_{y,\eta}\right) - \frac{4}{3h^2}\zeta^3\psi_{y,\eta}\right\}\cos^2\theta \\ & - \psi_y\left(1 - \frac{4}{h^2}\zeta^2\right)\cos\theta\sin\theta\end{aligned} \tag{3.16b}$$

$$\begin{aligned}\varepsilon_3 = {} & \left\{v_{o,\eta} + \zeta\left(-w_{o,\eta\eta} + \psi_{y,\eta}\right) - \frac{4}{3h^2}\zeta^3\psi_{y,\eta}\right\}\sin^2\theta \\ & + \psi_y\left(1 - \frac{4}{h^2}\zeta^2\right)\cos\theta\sin\theta\end{aligned} \tag{3.16c}$$

$$\begin{aligned}\varepsilon_4 = {} & \left\{v_{o,\eta} + \zeta\left(-w_{o,\eta\eta} + \psi_{y,\eta}\right) - \frac{4}{3h^2}\zeta^3\psi_{y,\eta}\right\}2\cos\theta\sin\theta \\ & + \psi_y\left(1 - \frac{4}{h^2}\zeta^2\right)\left(\cos^2\theta - \sin^2\theta\right)\end{aligned} \tag{3.16d}$$

$$\varepsilon_5 = \left\{u_{o,\eta} + v_{o,\chi} + \zeta\left(-2w_{o,\chi\eta} + \psi_{x,\eta} + \psi_{y,\chi}\right) - \frac{4}{3h^2}\zeta^3\left(\psi_{x,\eta} + \psi_{y,\chi}\right)\right\}\sin\theta$$
$$+ \psi_x\left(1 - \frac{4}{h^2}\zeta^2\right)\cos\theta$$
$$+ \left\{v_o + \zeta\left(-w_{o,\eta} + \psi_y\right) - \frac{4}{3h^2}\zeta^3\psi_y - Z_o w_{o,\eta}\right\}\cos\theta\,\theta_{,x}$$
$$+ \left[\left\{v_{o,\eta} + \zeta\left(-w_{o,\eta\eta} + \psi_{y,\eta}\right) - \frac{4}{3h^2}\zeta^3\psi_{y,\eta}\right\}(\zeta - Z_o)\right.$$
$$\left. - \left\{-w_{o,\eta} + \psi_y - \frac{4}{h^2}\zeta^2\psi_y\right\}(\eta - Y_o) - w_o\right]\sin\theta\,\theta_{,x} \qquad (3.16e)$$
$$- \left\{-w_{o,\eta} + \psi_y - \frac{4}{h^2}\zeta^2\psi_y\right\}\sin\theta\, z^*_{o,x}$$

$$\varepsilon_6 = \left\{u_{o,\eta} + v_{o,\chi} + \zeta\left(-2w_{o,\chi\eta} + \psi_{x,\eta} + \psi_{y,\chi}\right) - \frac{4}{3h^2}\zeta^3\left(\psi_{x,\eta} + \psi_{y,\chi}\right)\right\}\cos\theta$$
$$- \psi_x\left(1 - \frac{4}{h^2}\zeta^2\right)\sin\theta$$
$$- \left\{v_o + \zeta\left(-w_{o,\eta} + \psi_y\right) - \frac{4}{3h^2}\zeta^3\psi_y - Z_o w_{o,\eta}\right\}\sin\theta\,\theta_{,x}$$
$$+ \left[\left\{v_{o,\eta} + \zeta\left(-w_{o,\eta\eta} + \psi_{y,\eta}\right) - \frac{4}{3h^2}\zeta^3\psi_{y,\eta}\right\}(\zeta - Z_o)\right.$$
$$\left. - \left\{-w_{o,\eta} + \psi_y - \frac{4}{h^2}\zeta^2\psi_y\right\}(\eta - Y_o) - w_o\right]\sin\theta\,\theta_{,x} \qquad (3.16f)$$
$$- \left\{-w_{o,\eta} + \psi_y - \frac{4}{h^2}\zeta^2\psi_y\right\}\cos\theta\, z^*_{o,x}$$

From the above equations, the following relationship between the local strains in the untwisted and the twisted coordinate systems is obtained.

$$\varepsilon_i = \hat{T}_{ij}\left(\tilde{\varepsilon}^o_j + \theta_{,x}\tilde{\mu}_j - z^*_{o,x}\tilde{\vartheta}_j\right) \qquad (3.17)$$

where $\tilde{\varepsilon}^o_j$ is the strain in the local, twisted coordinate system in the absence of pre-twist and sweep, $\tilde{\mu}_j$ is the additional strain components due to pre-twist and $\theta_{,x}$ is the twist rate. The additional strain components due to the sweep are denoted $\tilde{\vartheta}_j$ and the sweep rate is

$z^*_{o,x}$. It must be noted that additional sweep terms appear only in the vertical walls due to the definition of sweep used in the modeling (see Fig. 3.5). The total strain in the local, untwisted coordinate system (x, y, z) is denoted ε_j and $\hat{T}_{ij}$ is the transformation matrix between the strains in the local, twisted coordinate system and the strains in the local, untwisted coordinate system. This transformation matrix is expressed as follows.

$$\hat{T}_{ij} = \begin{bmatrix} 1 & 0 & 0 & 0 & 0 & 0 \\ 0 & c^2\theta & s^2\theta & -c\theta s\theta & 0 & 0 \\ 0 & s^2\theta & c^2\theta & c\theta s\theta & 0 & 0 \\ 0 & 2c\theta s\theta & -2c\theta s\theta & c^2\theta - s^2\theta & 0 & 0 \\ 0 & 0 & 0 & 0 & c\theta & s\theta \\ 0 & 0 & 0 & 0 & -s\theta & c\theta \end{bmatrix}. \tag{3.18}$$

Note that the transformation matrix for the strains ($\hat{T}_{ij}$) is different from the transformation matrix for the displacements ($\mathbf{T}_{ur}$). The local inplane strains in the absence of pre-twist or sweep are derived as follows.

$$\begin{aligned} \tilde{\varepsilon}^o_1 &= e^o_1 + \zeta\kappa^1_1 + \zeta^3\kappa^3_1 \\ \tilde{\varepsilon}^o_2 &= e^o_2 + \zeta\kappa^1_2 + \zeta^3\kappa^3_2 \\ \tilde{\varepsilon}^o_6 &= e^o_6 + \zeta\kappa^1_6 + \zeta^3\kappa^3_6 \end{aligned} \tag{3.19a-c}$$

The out of plane strains are expressed similarly as

$$\begin{aligned} \tilde{\varepsilon}^o_3 &= 0, \\ \tilde{\varepsilon}^o_4 &= e^o_4 + \zeta^2\kappa^2_4, \\ \tilde{\varepsilon}^o_5 &= e^o_5 + \zeta^2\kappa^2_5. \end{aligned} \tag{3.19d-f}$$

The additional strains due to beam pre-twist are as follows

$$\begin{aligned} \tilde{\mu}_1 &= \mu^o_1 + \zeta\mu^1_1 + \zeta^2\mu^2_1 + \zeta^3\mu^3_1 + \zeta^4\mu^4_1, \\ \tilde{\mu}_2 &= \tilde{\mu}_3 = \tilde{\mu}_4 = 0, \\ \tilde{\mu}_5 &= \mu^o_5 + \zeta\mu^1_5 + \zeta^3\mu^3_5, \\ \tilde{\mu}_6 &= \mu^o_6 + \zeta\mu^1_6 + \zeta^2\mu^2_6 + \zeta^3\mu^3_6 + \zeta^4\mu^4_6. \end{aligned} \tag{3.20a-f}$$

The additional strain components due to the sweep are

$$\tilde{\vartheta}_1 = \vartheta_1^o + \zeta^2\vartheta_1^2,$$
$$\tilde{\vartheta}_2 = 0, \quad \tilde{\vartheta}_3 = 0, \quad \tilde{\vartheta}_4 = 0, \quad \tilde{\vartheta}_5 = 0, \tag{3.21a-f}$$
$$\tilde{\vartheta}_6 = \vartheta_6^o + \zeta^2\vartheta_6^2,$$

where the nonzero components of the individual strains are described in Appendix B.

3.4 Energy Formulation

The beam equations of motion are derived using Hamilton's principle [93] which assumes the following form.

$$\delta\int_{t_1}^{t_2}(U - T + W_e)dt \quad = \quad 0 \tag{3.22}$$

where $\delta(\,)$ represents the variation of $(\,)$ and U, T and W_e represent the total beam strain energy, kinetic energy and external work, respectively. Using variational principles, Eqn. 3.22 may be rewritten in terms of the individual plate quantities as follows.

$$\int_{t_1}^{t_2}\left(\sum_{i=1}^{N}\delta U_i - \delta T_i + \delta W_{e_i}\right)dt \quad = \quad 0 \tag{3.23}$$

where N is the total number of walls (N = 4 for a box beam). The individual strain energy density (U_o) in each plate is calculated as follows.

$$U_o = \int_0^{\varepsilon_i}\sigma_i d\varepsilon_i \tag{3.24}$$

Using the generalized Hooke's Law ($\sigma_\iota = Q_{ij}\varepsilon_j$), Eqn 3.24 is rewritten as

$$U_o = \frac{1}{2}Q_{ij}\varepsilon_i\varepsilon_j, \tag{3.25}$$

where repeated indices (i, j = 1, 2, $\cdots$, 6) indicate summation and σ_i is the strain tensor. The quantities Q_{ij} denote the full three-dimensional material properties in the local,

untwisted coordinate system which, for laminates made of orthotropic plies, is represented as follows.

$$Q_{ij} = \begin{bmatrix} Q_{11} & Q_{12} & Q_{13} & 0 & 0 & Q_{16} \\ Q_{12} & Q_{22} & Q_{23} & 0 & 0 & Q_{26} \\ Q_{13} & Q_{23} & Q_{33} & 0 & 0 & Q_{36} \\ 0 & 0 & 0 & Q_{44} & Q_{45} & 0 \\ 0 & 0 & 0 & Q_{45} & Q_{55} & 0 \\ Q_{16} & Q_{26} & Q_{36} & 0 & 0 & Q_{66} \end{bmatrix} \tag{3.26}$$

The material properties in terms of the local, untwisted coordinate system (x, y, z) are written in terms of the material properties in local, twisted and swept coordinate system (χ, η, ζ) as follows.

$$Q_{ij} = \hat{T}_{mi}\tilde{Q}_{mn}\hat{T}_{nj}, \tag{3.27}$$

where $\tilde{Q}_{mn}$ represents the material properties in the local, twisted coordinate system. The total strain energy in the i-th wall (U_i) is then written, using Eqns. 3.18 and 3.26 as follows.

$$\begin{aligned} U_i &= \int_V U_{o_i} dV \\ &= \frac{1}{2}\int_V \left(\tilde{\varepsilon}^o_m + \theta_{,x}\tilde{\mu}_m - z^*_{o,x}\tilde{\vartheta}_m\right)\hat{T}_{ik}\hat{T}_{mi}\tilde{Q}_{mn}\hat{T}_{nj}\hat{T}_{jl}\left(\tilde{\varepsilon}^o_n + \theta_{,x}\tilde{\mu}_n - z^*_{o,x}\tilde{\vartheta}_n\right)dV \end{aligned} \tag{3.28}$$

where V indicates integration over the volume of the wall. Due to the orthogonality of the transformation matrix, $\hat{\mathbf{T}}$, ($\hat{T}_{ik}\hat{T}_{mi} = \delta_{km}$, where δ_{km} is the Kronecker delta) Eqn. 3.28 is simplified as follows.

$$U_i = \frac{1}{2}\int_{\Omega}\int_{-h/2}^{h/2}\left(\tilde{\varepsilon}^o_m + \theta_{,x}\tilde{\mu}_m - z^*_{o,x}\tilde{\vartheta}_m\right)\tilde{Q}_{mn}\left(\tilde{\varepsilon}^o_n + \theta_{,x}\tilde{\mu}_n - z^*_{o,x}\tilde{\vartheta}_m\right) d\zeta\, d\Omega \tag{3.29}$$

where $d\Omega$ is the differential area ($d\Omega = d\chi d\eta$). The strain energy can be rewritten using Eqns. 3.19-3.21 and 3.29.

$$U_i = \frac{1}{2}\int_{\Omega} \boldsymbol{\beta}_m^T \begin{bmatrix} A_{mn} & B_{mn} & D_{mn} & E_{mn} & F_{mn} \\ B_{mn} & D_{mn} & E_{mn} & F_{mn} & G_{mn} \\ D_{mn} & E_{mn} & F_{mn} & G_{mn} & H_{mn} \\ E_{mn} & F_{mn} & G_{mn} & H_{mn} & O_{mn} \\ F_{mn} & G_{mn} & H_{mn} & O_{mn} & P_{mn} \end{bmatrix} \boldsymbol{\beta}_n d\Omega \qquad (3.30)$$

$$= \frac{1}{2}\int_{\Omega} \boldsymbol{\beta}_m^T Q_{mn} \boldsymbol{\beta}_n d\Omega$$

where m, n = 1, 2, ···, 6 and the laminate stiffness matrices (**A** - **P**) are defined in each of the walls as follows.

$$(\mathbf{A},\mathbf{B},\mathbf{D},\mathbf{E},\mathbf{F},\mathbf{G},\mathbf{H},\mathbf{O},\mathbf{P}) = \int_{-h/2}^{h/2} \tilde{\mathbf{Q}}\left(1,\zeta,\zeta^2,\zeta^3,\zeta^4,\zeta^5,\zeta^6,\zeta^7,\zeta^8\right) d\zeta \qquad (3.31)$$

For composite laminates, $\tilde{\mathbf{Q}}$ is ply dependent and as a result it is a function of the thickness coordinate ζ. Therefore, this matrix cannot be taken out of the integral in Eqn. 3.31. The vector $\boldsymbol{\beta}_m$ is defined as

$$\boldsymbol{\beta}_m = \Big[(e_m^o + \mu_m^o \theta_{,x} - z_{o,x}^* \vartheta_m^o) \quad (\kappa_m^1 + \mu_m^1 \theta_{,x}) \quad (\kappa_m^2 + \mu_m^2 \theta_{,x} - z_{o,x}^* \vartheta_m^2) \quad (\kappa_m^3 + \mu_m^3 \theta_{,x}) \quad \mu_m^4 \theta_{,x}\Big]^T \qquad (3.32)$$

The external work due to applied loads and body forces (W_e) in the i-th wall is written as

$$W_{e_i} = \int_V \text{X}_j \tilde{u}_j dV + \int_S \hat{t}_j \tilde{u}_j dS \qquad j = 1, 2, 3 \qquad (3.33)$$

where $\tilde{u}_j$ is the displacement vector defined as $[\tilde{u}_1 \ \tilde{u}_2 \ \tilde{u}_3]^T$, X_1, X_2, and X_3 are the body forces in the X, Y and Z directions, respectively. Applied surface tractions over the region of the surface S are denoted $\hat{t}_1$, $\hat{t}_2$ and $\hat{t}_3$, along the respective directions.

The total kinetic energy in the i-th wall is expressed as

$$T_i = \frac{1}{2}\int_V \rho v_j v_j dV \qquad j = 1, 2, 3 \qquad (3.34)$$

where $\mathbf{v}_i$ is the velocity vector defined as

$$\mathbf{v}_i = \frac{\partial \tilde{\mathbf{u}}_i}{\partial t} + \Omega \hat{k} \times \mathbf{r}_i, \tag{3.35}$$

$\tilde{\mathbf{u}}_i$ is the displacement vector, Ω is the rotational velocity about the Z axis and $\mathbf{r}_i$ is a position vector from the axis of rotation to an arbitrary point in the i-th wall (Fig. 3.6). The position vector is written as follows.

$$\mathbf{r} = X_o \hat{i} + Y_o \hat{j} \quad + \quad (\chi + \tilde{u}_1)\hat{e}_\chi + (\eta + \eta_o + \tilde{u}_2)\hat{e}_\eta + (\zeta + \zeta_o + \tilde{u}_3)\hat{e}_\zeta, \tag{3.36}$$

where X_o and Y_o are the offsets in the global, untwisted coordinate system from the axis of rotation to the center of twist and η_o and ζ_o are the local offsets to an arbitrary point on the wall expressed in terms of the local, twisted and swept axis system. Using Eqns. 3.35 and 3.36 and the coordinate transformations defined in Appendix A, the kinetic energy is expressed as follows.

$$\begin{aligned} T_i = \frac{1}{2}\int_V \rho \Big[& \Big\{ \dot{\tilde{u}}_1^2 + 2\dot{\tilde{u}}_1\left(\zeta + \zeta_o^* + \tilde{w}\right)\Omega_\eta - 2\dot{\tilde{u}}_1\left(\eta + \eta_o^* + \tilde{u}_2\right)\Omega_\zeta + \left(\zeta + \zeta_o^* + \tilde{u}_3\right)^2 \Omega_\eta^2 \\ & - 2\left(\zeta + \zeta_o^* + \tilde{u}_3\right)\left(\eta + \eta_o^* + \tilde{u}_2\right)\Omega_\eta\Omega_\zeta + \left(\eta + \eta_o^* + \tilde{u}_2\right)^2 \Omega_\xi^2 \Big\} \\ & + \Big\{ \dot{\tilde{u}}_2^2 + 2\dot{\tilde{u}}_2\left(\chi + \chi_o^* + \tilde{u}_1\right)\Omega_\zeta + \left(\chi + \chi_o^* + \tilde{u}_1\right)^2 \Omega_\xi^2 \Big\} \\ & + \Big\{ \dot{\tilde{u}}_3^2 - 2\dot{\tilde{u}}_3\left(\chi + \chi_o^* + \tilde{u}_1\right)\Omega_\eta + \left(\chi + \chi_o^* + \tilde{u}_1\right)^2 \Omega_\eta^2 \Big\} \Big] dV \end{aligned} \tag{3.37}$$

where the rotational and position vectors (Eqns. 3.35 and 3.36) are rewritten as

$$\mathbf{r} = \left(\chi + \chi_o^* + \tilde{u}_1\right)\hat{e}_\chi + \left(\eta + \eta_o^* + \tilde{u}_2\right)\hat{e}_\eta + \left(\zeta + \zeta_o^* + \tilde{u}_3\right)\hat{e}_\zeta, \tag{3.38}$$

$$\Omega \hat{k} = \Omega_\eta \hat{e}_\eta + \Omega_\zeta \hat{e}_\zeta, \tag{3.39}$$

and $(\dot{})$ represents a differentiation with respect to time.

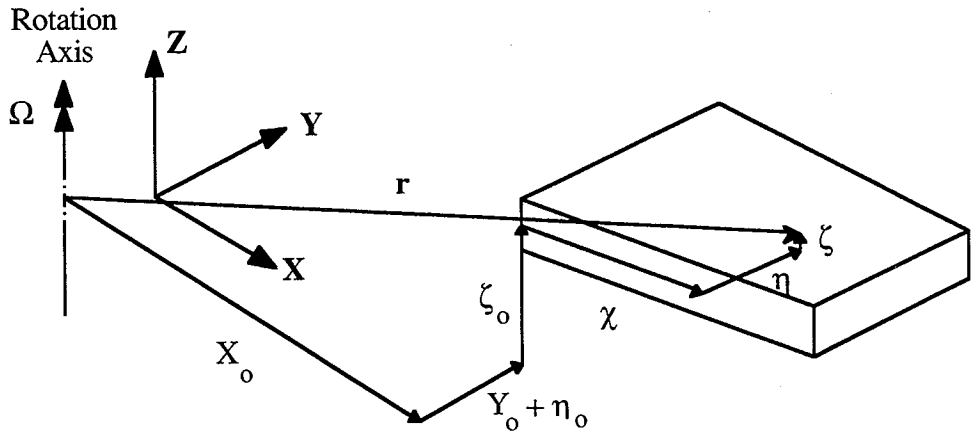

Fig. 3.6 Rotational offsets and position vector.

3.5 Incremental Stiffness Due to Rotation

To properly obtain the natural frequencies of rotating plates and beams, it is necessary to consider the stiffening effects which arise due to the stresses generated by rotation. This procedure involves two steps. First the stresses of the beam are calculated for centrifugal forces only. Then the incremental stiffness due to rotation is computed and is added to the original stiffness matrix. The procedure for calculating the incremental stiffness matrix is outlined below.

The additional strain energy due to centrifugal stiffening in each of the walls (U_{cf}) is given by [105]

$$U_{cfi} = \frac{1}{2}\int_V \left[\omega_\chi{}^2\sigma_\eta + \omega_\eta{}^2\sigma_\chi + \omega_\zeta{}^2\left(\sigma_\chi + \sigma_\eta\right) - 2\omega_\chi\omega_\eta\sigma_{\chi\eta} - 2\omega_\eta\omega_\zeta\sigma_{\eta\zeta} - 2\omega_\chi\omega_\zeta\sigma_{\chi\zeta}\right] dV \tag{3.40}$$

where ω_χ, ω_η and ω_ζ are the rotations about χ, η, ζ axes, respectively. It is important to note that in the above equation, the strains are not included in the formulation based on the assumption that their effects are small compared to the rotations. Equation 3.40 may be written in matrix notation as follows.

$$U_{cfi} = \frac{1}{2}\int_V \begin{bmatrix} \omega_\chi & \omega_\eta & \omega_\zeta \end{bmatrix} \begin{bmatrix} \sigma_\eta & -\sigma_{\chi\eta} & -\sigma_{\chi\zeta} \\ -\sigma_{\chi\eta} & \sigma_\chi & -\sigma_{\eta\zeta} \\ -\sigma_{\chi\zeta} & -\sigma_{\eta\zeta} & (\sigma_\chi + \sigma_\eta) \end{bmatrix} \begin{Bmatrix} \omega_\chi \\ \omega_\eta \\ \omega_\zeta \end{Bmatrix} dV \tag{3.41}$$

where the stresses σ_{ij} are due purely to the centrifugal force in each individual wall. The rotations are calculated as follows.

$$\omega_\chi = \frac{1}{2}\left(\frac{\partial \tilde{u}_3}{\partial \eta} - \frac{\partial \tilde{u}_2}{\partial \zeta}\right)$$

$$\omega_\eta = \frac{1}{2}\left(\frac{\partial \tilde{u}_1}{\partial \zeta} - \frac{\partial \tilde{u}_3}{\partial \chi}\right) \tag{3.42a-c}$$

$$\omega_\zeta = \frac{1}{2}\left(\frac{\partial \tilde{u}_2}{\partial \chi} - \frac{\partial \tilde{u}_1}{\partial \eta}\right)$$

Using Eqns. 3.12 and 3.42 the rotations are rewritten as

$$\omega_\chi = \frac{\partial w_o}{\partial \eta} - \frac{1}{2}\left(1 - \frac{4}{h^2}\right)\psi_y,$$

$$\omega_\eta = -\frac{\partial w_o}{\partial \chi} + \frac{1}{2}\left(1 - \frac{4}{h^2}\right)\psi_x, \tag{3.43a-c}$$

$$\omega_\zeta = \frac{1}{2}\left(\frac{\partial v_o}{\partial \chi} - \frac{\partial u_o}{\partial \eta}\right).$$

3.6 Variational Method

The variation of strain energy is written as follows.

$$\delta U_i = \int_\Omega \beta_m^T Q_{mn} \delta\beta_n d\Omega \qquad m, n = 1, 2, \cdots, 6 \tag{3.44}$$

where the variation of the strain vector β_m is expressed as the sum of the variation of the strain in the untwisted coordinate system, the variation of the strain due to pre-twist and the variation of the strain associated with sweep as follows.

$$\delta\beta_m = \Big[(\delta e_m^o + \delta\mu_m^o\theta_{,x} - \delta\vartheta_m^o z_{o,x}^*)\ \ (\delta\kappa_m^1 + \delta\mu_m^1\theta_{,x})$$
$$(\delta\kappa_m^2 + \delta\mu_m^2\theta_{,x} - \delta\vartheta_m^2 z_{o,x}^*)\ \ (\delta\kappa_m^3 + \delta\mu_m^3\theta_{,x})\ \ \delta\mu_m^4\theta_{,x}\Big]^T \tag{3.45}$$

The variation of the potential energy of the applied loads is expressed as

$$\delta W_{e_i} = \int_V \bar{X}_j \delta\tilde{u}_j dV + \int_S \hat{t}_j \delta\tilde{u}_j dS, \qquad j = 1, 2, 3. \tag{3.46}$$

Due the presence of the rotational velocity, the variation of the kinetic energy can be expressed in terms of four individual components as follows.

$$\delta T_i = \delta T_{m_i} + \delta T_{c_i} + \delta T_{k_i} + \delta T_{f_i} \tag{3.47}$$

where the subscript 'm' denotes the component of the kinetic energy that is used to form the mass matrix. Similarly, the subscripts 'c', 'k' and 'f' indicate the components that are used in the formulation of the gyroscopic matrix, the stiffness matrix and the forcing vector, respectively. The exact form of these variations are as follows.

$$\delta T_{m_i} = \int_V \rho\left[\ \ddot{\tilde{u}}_1\delta\tilde{u}_1 + \ddot{\tilde{u}}_2\delta\tilde{u}_2 + \ddot{\tilde{u}}_3\delta\tilde{u}_3\right] dV \tag{3.48}$$

$$\delta T_{c_i} = \int_V \rho\left[\ \left(2\dot{\tilde{u}}_2\Omega_\zeta - 2\dot{\tilde{u}}_3\Omega_\eta\right)\delta\tilde{u}_1 - 2\dot{\tilde{u}}_1\Omega_\zeta\delta\tilde{u}_2 + 2\dot{\tilde{u}}_1\Omega_\eta\delta\tilde{u}_3\right] dV \tag{3.49}$$

$$\delta T_{k_i} = \int_V \rho\Big[\left(\Omega_\eta^2 + \Omega_\zeta^2\right)\tilde{u}_1\delta\tilde{u}_1 + \left(\Omega_\zeta^2\tilde{u}_2 - \Omega_\eta\Omega_\zeta\tilde{u}_3\right)\delta\tilde{u}_2$$
$$+ \left(-\Omega_\eta\Omega_\zeta\tilde{u}_2 + \Omega_\eta^2\tilde{u}_3\right)\delta\tilde{u}_3\Big] dV \tag{3.50}$$

$$\delta T_{f_i} = \int_V \rho\left[\ \left(\Omega_\eta^2 + \Omega_\zeta^2\right)\left(\chi + \chi_o^*\right)\delta\tilde{u}_1 + \left(\Omega_\zeta^2\left(\eta + \eta_o^*\right) - \Omega_\eta\Omega_\zeta\zeta_o^*\right)\delta\tilde{u}_2\right.$$
$$\left. + \ \left(-\Omega_\eta\Omega_\zeta\left(\eta + \eta_o^*\right) + \Omega_\eta^2\zeta_o^*\right)\delta\tilde{u}_3\right] dV \tag{3.51}$$

The quantity δT_{m_i}, in each wall, is rewritten as

$$\delta T_{m_i} = \int_{\Omega} \left\{ \ddot{\lambda}^o_j \quad \ddot{\lambda}^1_j \quad \ddot{\lambda}^3_j \right\} \begin{bmatrix} \Delta^o_{jk} & \Delta^1_{jk} & \Delta^3_{jk} \\ \Delta^1_{jk} & \Delta^2_{jk} & \Delta^4_{jk} \\ \Delta^3_{jk} & \Delta^4_{jk} & \Delta^6_{jk} \end{bmatrix} \begin{Bmatrix} \delta\lambda^o_k \\ \delta\lambda^1_k \\ \delta\lambda^3_k \end{Bmatrix} d\Omega \qquad j, k = 1, 2, 3 \qquad (3.52)$$

where λ^0, λ^1 and λ^3 correspond to the zeroth, the first and the third-order components (in ζ) of the displacement field, respectively. These quantities are defined as follows.

$$\lambda^o = \left[u_o \quad v_o \quad w_o \right]^T$$

$$\lambda^1 = \left[\left(-w_{o,\chi} + \psi_x \right) \quad \left(-w_{o,\eta} + \psi_y \right) \quad 0 \right]^T \qquad (3.53a\text{-}c)$$

$$\lambda^3 = \left[-\frac{4}{3h^2}\psi_x \quad -\frac{4}{3h^2}\psi_y \quad 0 \right]^T$$

The density matrices, Δ^n_{jk}, are defined as

$$\left(\Delta^0_{jk}, \Delta^1_{jk}, \Delta^2_{jk}, \Delta^3_{jk}, \Delta^4_{jk}, \Delta^6_{jk} \right) = \int_{-h/2}^{h/2} \rho \left(1, \zeta, \zeta^2, \zeta^3, \zeta^4, \zeta^6 \right) d\zeta. \qquad (3.54)$$

Although simple closed form expressions cannot be obtained for the remaining components of the variation of the kinetic energy, they can be computed in a straight forward manner as discussed later.

The variation of the strain energy due to the centrifugal stiffening in each wall is written as

$$\delta U_{cf_i} = \int_V \omega^T_m \, \tilde{\Sigma}_{mn} \, \delta\omega_n \, dV, \qquad m, n = 1, 2, 3 \qquad (3.55)$$

where

$$\omega_m = \begin{Bmatrix} \dfrac{\partial w_o}{\partial \eta} - \dfrac{1}{2}\left(1 - \dfrac{4}{h^2}\zeta^2\right)\psi_z \\ -\dfrac{\partial w_o}{\partial \chi} + \dfrac{1}{2}\left(1 - \dfrac{4}{h^2}\zeta^2\right)\psi_x \\ \dfrac{1}{2}\left(\dfrac{\partial v_o}{\partial \chi} - \dfrac{\partial u_o}{\partial \eta}\right) \end{Bmatrix}, \tag{3.56}$$

and

$$\tilde{\Sigma}_{mn} = \begin{bmatrix} \sigma_\eta & -\sigma_{\chi\eta} & -\sigma_{\chi\zeta} \\ -\sigma_{\chi\eta} & \sigma_\chi & -\sigma_{\eta\zeta} \\ -\sigma_{\chi\zeta} & -\sigma_{\eta\zeta} & (\sigma_\chi + \sigma_\eta) \end{bmatrix}. \tag{3.57}$$

It must be noted that the stresses in Eqn. 3.57 are due to centrifugal forces only which are determined based on the forces associated with Eqn. 3.51. Therefore, Eqn 3.51 is used only to determine the steady state stresses due to rotation. After these stresses are calculated and the incremental stiffnesses are determined, the forcing terms associated with this equation are no longer included in the formulation.

3.7 Solution Procedure

The solution of the equations of motion is obtained using a two-dimensional finite element formulation in the local, twisted and swept coordinate system of each individual plate (χ, η, ζ). A four noded plate element is used to discretize the individual plates of the beam. This element is C^1 continuous in the zeroth order displacements (u_o, v_o, w_o) and is C^o continuous in the higher order terms (ψ_x, ψ_y). As a result, the element contains 11 degrees of freedom per node which are defined in terms of the nodal degree of freedom vector as follows.

$$\tilde{\mathbf{q}} = \left[u_o, \frac{\partial u_o}{\partial \chi}, \frac{\partial u_o}{\partial \eta}, v_o, \frac{\partial v_o}{\partial \chi}, \frac{\partial v_o}{\partial \eta}, w_o, \frac{\partial w_o}{\partial \chi}, \frac{\partial w_o}{\partial \eta}, \psi_x, \psi_y \right]^T \tag{3.58}$$

3.7.1 Continuity conditions: To maintain the continuity of displacements throughout the entire beam, constraints are imposed at the corners of each individual plate as follows.

$$\begin{aligned} {}^{1}u_o(\chi,\eta=b_1) &= {}^{2}u_o(\chi,\eta=0) \\ {}^{1}v_o(\chi,\eta=b_1) &= -{}^{2}w_o(\chi,\eta=0) \\ {}^{1}w_o(\chi,\eta=b_1) &= {}^{2}v_o(\chi,\eta=0) \end{aligned} \tag{3.59a-c}$$

where the preceding superscripts '1' and '2' denote walls 1 and 2, respectively and b_1 is the width of wall 1 (Figs. 3.3 and 3.4). It must be noted that these equalities must be satisfied for all values of χ. Therefore, the partial derivatives of the above equalities, with respect to χ, must also be satisfied. To ensure that the angle between the walls remains 90° after deformation, the following constraints are imposed on the rotations about the χ-axis.

$$\begin{aligned} {}^{1}w_{o,\eta}(\chi,\eta=b_1) &= {}^{2}w_{o,\eta}(\chi,\eta=0) \\ {}^{1}\psi_y(\chi,\eta=b_1) &= {}^{2}\psi_y(\chi,\eta=0) \end{aligned} \tag{3.60}$$

Similar sets of constraints are derived at each of the four corners of the box beam.

3.7.2 Finite element formulation: The finite element approach is used to solve the complete beam equations of motion (Eqn. 3.23). Denoting **q** as the nodal degree of freedom vector, it is possible to express the strain (Eqn. 3.5) in the following form

$$\tilde{\varepsilon}_i = \left(\Gamma_{ij} + \theta_{,x}\Phi_{ij} - z^*_{o,x}\Xi_{ij}\right)q_j. \tag{3.61}$$

The partial derivatives of the strain vector with respect to q_j are then written as

$$\frac{\partial\tilde{\varepsilon}_i}{\partial q_j} = \Gamma_{ij} + \theta_{,x}\Phi_{ij} - z^*_{o,x}\Xi_{ij}. \tag{3.62}$$

Note that quantities Γ, Φ and Ξ can be expanded in terms of ζ as follows

$$\begin{aligned} \Gamma_{ij} &= \left[\Gamma^o_{ij}\ \Gamma^1_{ij}\ \Gamma^2_{ij}\ \Gamma^3_{ij}\ \Gamma^4_{ij}\right]\bullet\left\{1\ \zeta\ \zeta^2\ \zeta^3\ \zeta^4\right\} \\ &= \mathcal{B}_{ij}\bullet\left\{1\ \zeta\ \zeta^2\ \zeta^3\ \zeta^4\right\}, \end{aligned} \tag{3.63}$$

$$\begin{aligned} \Phi_{ij} &= \left[\Phi^o_{ij}\ \Phi^1_{ij}\ \Phi^2_{ij}\ \Phi^3_{ij}\ \Phi^4_{ij}\right]\bullet\left\{1\ \zeta\ \zeta^2\ \zeta^3\ \zeta^4\right\} \\ &= \mathcal{R}_{ij}\bullet\left\{1\ \zeta\ \zeta^2\ \zeta^3\ \zeta^4\right\}, \end{aligned} \tag{3.64}$$

and

$$\Xi_{ij} = \left[\Xi^{o}_{ij} \quad \Xi^{2}_{ij}\right] \bullet \left\{1 \quad \zeta^2\right\} = \mathcal{L}_{ij} \bullet \left\{1 \quad \zeta^2\right\}. \tag{3.65}$$

The rotation terms (ω_i) may also be expressed as a function of the nodal degrees of freedom as follows

$$\omega_i = \Theta_{ij} q_j \tag{3.66}$$

so that

$$\frac{\partial \omega_i}{\partial q_j} = \Theta_{ij}. \tag{3.67}$$

Similarly, the displacement vector **u** may be written as

$$\begin{Bmatrix} \tilde{u}_1 \\ \tilde{u}_2 \\ \tilde{u}_3 \end{Bmatrix} = \begin{Bmatrix} s_{uj} \\ s_{vj} \\ s_{wj} \end{Bmatrix} q_j \tag{3.68}$$

or

$$\tilde{u}_i = S_{ij} q_j \tag{3.69}$$

such that partial derivatives of the displacements with respect to q_j are as follows

$$\frac{\partial \tilde{u}_i}{\partial q_j} = S_{ij}. \tag{3.70}$$

Note that the displacement matrix can similarly be written in terms of the thickness coordinate as

$$S_{ij} = \left[S^{o}_{ij} \quad S^{1}_{ij} \quad S^{3}_{ij}\right] \bullet \left\{1 \quad \zeta \quad \zeta^3\right\} = \mathcal{M}_{ij} \bullet \left\{1 \quad \zeta \quad \zeta^3\right\}. \tag{3.71}$$

Using the finite element approach, the coupled (dynamic/aerodynamic) beam equations of motion are written in matrix form as follows

$$\mathbf{M}\,\ddot{\mathbf{q}}(t) + \mathbf{C}\,\dot{\mathbf{q}}(t) + \mathbf{K}\,\mathbf{q}(t) = \mathbf{F}(t) \tag{3.72}$$

where **M**, **C** and **K** are the mass, the damping and the stiffness matrices, respectively and **F** is the external force vector representing loads corresponding to the beam nodal degrees of freedom (**q**). Note that in Eqn. 3.72, the **C** matrix represents the gyroscopic (Coriolis) effects and not damping of the system. As a result, the equations of motion as formulated represent an undamped system. Therefore a proportional damping (two percent) is assumed in the model to represent the structural damping. The proportional damping is determined based on the natural frequencies obtained through consideration of the mass and the stiffness terms only in Eqn. 3.72. These terms are augmented to the **C** matrix. It must be noted that additional terms analogous to damping and stiffness terms will be introduced through aerodynamic loading. These terms are augmented to the appropriates matrices in Eqn. 3.72 as explained in detail in Chapter 5. The matrices and forcing vector due to the structural contribution only are expressed as follows.

$$\mathbf{M} = \sum_{i=1}^{N}\left[\int_{V}\rho\mathbf{S}^{T}\mathbf{S}\,dV\right], \tag{3.73}$$

$$\mathbf{C} = \sum_{i=1}^{N}\left[\int_{V}\rho\left[2\Omega_{\eta}\left(\mathbf{s}_{w}\mathbf{s}_{u}^{T}-\mathbf{s}_{u}\mathbf{s}_{w}^{T}\right)-2\Omega_{\zeta}\left(\mathbf{s}_{v}\mathbf{s}_{u}^{T}-\mathbf{s}_{u}\mathbf{s}_{v}^{T}\right)\right]dV\right], \tag{3.74}$$

$$\begin{aligned}\mathbf{K}^{*} = &\sum_{i=1}^{N}\left[\int_{\Omega}\left(\mathcal{B}^{T}+\theta_{,x}\mathcal{R}^{T}-z_{o,x}^{*}\mathcal{L}^{T}\right)\mathcal{Q}\left(\mathcal{B}+\theta_{,x}\mathcal{R}-z_{o,x}^{*}\mathcal{L}\right)d\Omega\right]\\ &-\sum_{i=1}^{N}\left[\int_{V}\rho\left[\Omega_{\eta}^{2}\left(\mathbf{s}_{u}\mathbf{s}_{u}^{T}+\mathbf{s}_{w}\mathbf{s}_{w}^{T}\right)-\Omega_{\eta}\Omega_{\zeta}\left(\mathbf{s}_{w}\mathbf{s}_{v}^{T}+\mathbf{s}_{v}\mathbf{s}_{w}^{T}\right)+\Omega_{\zeta}^{2}\left(\mathbf{s}_{u}\mathbf{s}_{u}^{T}+\mathbf{s}_{v}\mathbf{s}_{v}^{T}\right)\right]dV\right],\end{aligned} \tag{3.75}$$

and the forcing vector is

$$\mathbf{F} = \sum_{i=1}^{N}\left[\int_{V}\mathbf{T}_{ur}\mathbf{S}\mathbf{X}\,dV+\int_{S}\mathbf{T}_{ur}\mathbf{S}\hat{\mathbf{t}}\,dS\right], \tag{3.76}$$

$$\mathbf{f}_{cf} = \sum_{i=1}^{N}\left[\int_{V}\rho\left\langle\Omega_{\eta}^{2}\left(s_u\left\{\chi+\chi_o^*\right\}+s_w\zeta_o^*\right)-\Omega_{\eta}\Omega_{\zeta}\left(s_w\left\{\eta+\eta_o^*\right\}+s_v\zeta_o^*\right)\right.\right.$$
$$\left.\left.+\Omega_{\zeta}^{2}\left(s_u\left\{\chi+\chi_o^*\right\}+s_v\left\{\eta+\eta_o^*\right\}\right)\right\rangle\right]dV\,. \tag{3.77}$$

Note that the matrix **C** in Eqn 3.75 does not include the proportional damping which can be determined only after an eigenanalysis of Eqn. 3.72 is performed. The matrix denoted **K*** (Eqn. 3.75) corresponds to the stiffness matrix obtained before the addition of the incremental stiffness due to rotation. Using Eqns 3.75 and 3.76 to determine the stresses due to beam rotation, the incremental stiffness matrix is calculated as follows.

$$\mathbf{K}_{cf} = \sum_{i=1}^{N}\left[\int_{V}\boldsymbol{\Theta}^{T}\,\tilde{\boldsymbol{\Sigma}}\,\boldsymbol{\Theta}\,dV\right], \tag{3.78}$$

where the stress matrix ($\tilde{\boldsymbol{\Sigma}}$) is determined from the solution to

$$\mathbf{K}^{*}\,\mathbf{q} = \mathbf{f}_{cf} \tag{3.79}$$

The total stiffness matrix (**K**) used in Eqn 3.72 is now written as a combination of $\mathbf{K}^{*}$ and $\mathbf{K}_{cf}$ as follows

$$\mathbf{K} = \mathbf{K}^{*} + \mathbf{K}_{cf}\,. \tag{3.80}$$

4. Composite Beam Results and Validation

The mesh sizes necessary for both individual plate and complete beam analyses are determined by performing a detailed convergence study. The details of this convergence study are presented in Appendix C. Next, beam correlations are presented in order to demonstrate the adequacy of the individual wall elements. Finally, the beam model (both thin-walled and thick-walled sections) is correlated with available experimental results and results obtained using a general purpose finite element code. Details of the correlation study are presented in the following sections. In the following sections, the elemental mesh size is defined as $M \times N$ where M is the number of chordwise elements and N is the number of spanwise elements. For the beam model, a consistent mesh is used in every wall and the mesh size presented corresponds to an individual wall. A finite element representation of a beam with a 10×4 mesh is illustrated in Fig. 4.1.

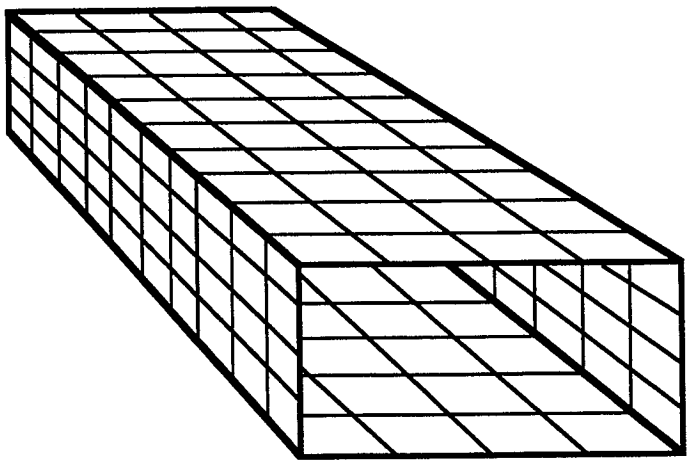

Fig. 4.1 Box beam finite element discretion; 10×4 mesh.

4.1 Higher-Order Plate Verification Studies

To demonstrate the importance of including the transverse shear terms in the formulation for the individual plates and to prove how well the present theory can capture these effects, results are first presented for individual plates. The accuracy of the plate theory is established from these validation studies, which are presented below.

4.1.1 Square, untwisted plate: Results are presented for a simply supported square, orthotropic plate under uniform loading (Fig. 4.2). The material properties of the plate are listed in Table 4.1. Figures 4.3 and 4.4 present the variations of the normalized center deflection, the normal axial stress (σ_1) and the transverse shear stress (σ_5) with plate thickness. The results of the present theory are compared with the those obtained using an exact elasticity approach [106]. Note that in Fig 4.4, results using the classical laminate theory (CLT) are not presented because in case of the axial stress, they are nearly identical to the results from the higher-order theory and in case of the transverse shear stress, they are zero. The figures indicate that the higher-order plate theory correlates very well with the exact elasticity solution [106]. Also, for moderately thick to very thick plates, the assumption of zero transverse shear stresses in CLT can introduce significant errors (Fig. 4.4).

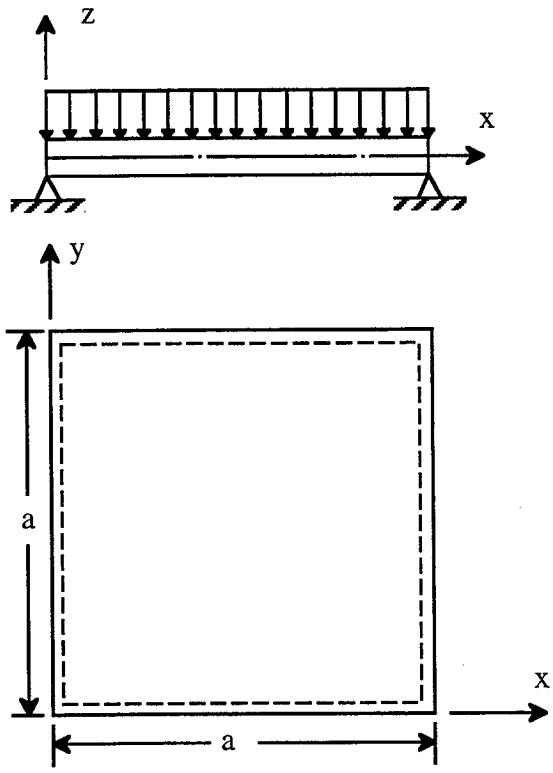

Fig. 4.2 Orthotropic square plate with fixed boundary conditions.

Table 4.1 Summary of orthotropic material properties[105]

$E_1 = 20.83 \times 10^6$ p.s.i., $E_2 = 1.094 \times 10^6$ p.s.i.,
$G_{12} = 6.10 \times 10^6$ p.s.i., $G_{13} = 3.71 \times 10^6$ p.s.i.,
$\mu_{12} = 0.44$

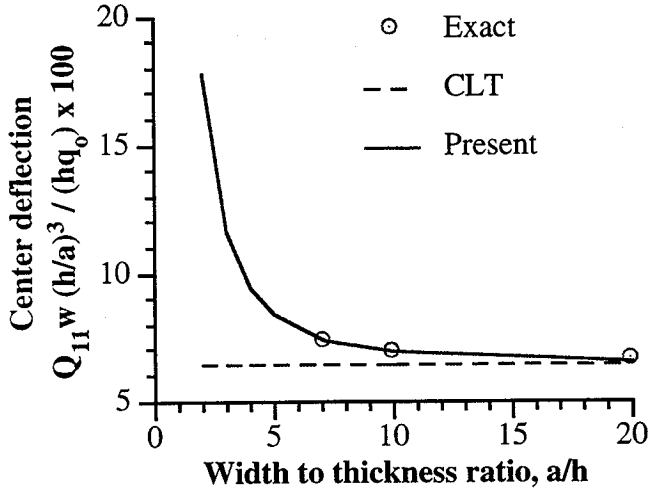

Fig. 4.3 Normalized center deflection of fixed orthotropic square plate under uniform distributed load.

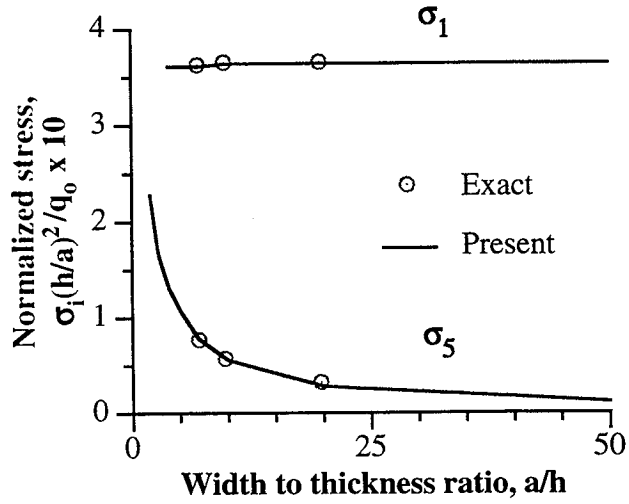

Fig. 4.4 Normalized stresses of fixed orthotropic square plate under uniform distributed load.

4.1.2 Plate with twist: From the convergence study it is determined that a 4×12 mesh (665 degrees of freedom) provides converged results and therefore this mesh size is used in all analyses involving the twisted plates. To validate the accuracy of the higher-order theory, the results are compared with published results. The first four natural frequencies for the plate are presented in Table 4.2. The natural frequencies are nondimensionalized as follows.

$$\lambda_i = \omega_i \sqrt{\frac{\rho h L^4}{D}}, \tag{4.1}$$

$$D = E\, h^3 / 12(1 - \nu^2). \tag{4.2}$$

The NASTRAN [105] results presented are due to MacBain [107] which uses a mesh size of 11×24 to yield a total of 1265 degrees of freedom. The Rayleigh-Ritz solution is due to Barton [108] in which an 18 term expansion for the deflection is used. In the table and following figures 'F' is used to denote a flexural or bending mode, 'T' is used to denote a torsional mode and 'PM_i' is used to indicate the i-th plate mode. From the table it is noted that although both the NASTRAN and the present approach correlate very well with the Ritz solution, the present approach is more accurate and requires fewer total degrees of freedom.

Table 4.2 Nondimensional frequencies of a flat, cantilevered plate
(ν = 0.3, L/w = 2.33)

Mode	Ritz	NASTRAN	% Difference*	Present	% Difference*
1F	3.47	3.43	- 1.2	3.43	- 1.1
1T	17.10	16.74	- 2.1	16.87	- 1.3
2F	21.58	21.36	- 1.0	21.45	- 0.6
2T	55.00	53.66	- 2.4	54.08	- 1.7

* Percent difference from Ritz solution.

The natural frequencies of the twisted, isotropic plates over a range of tip twist values, are presented in Figs. 4.5 - 4.7. In addition to the results obtained using the present approach, experimental data [107] and results obtained using NASTRAN are also presented. In these plates, the twist is assumed to vary linearly along the span. Results are presented for tip twist values of θ_T = 0°, 12°, 17°, 23.5°, 30° and 38° to correlate with available experimental data. In addition, results using the present approach are also calculated at pre-twist values of 45° and 60° to further examine the trends. From the figures, excellent correlation is noted in all cases, with a possible exception of the first plate mode (PM_1) for low tip twist values. However, it must be noted that the experimental value for this particular mode is also not available [107]. Using the present approach, its value is very close to the third torsional mode (3T, Fig. 4.7). The proximity of these natural frequencies might explain why it was possible to experimentally determine only one of these values (3T). This also suggests that the current theory does accurately predict the natural frequency of this mode and the results obtained using NASTRAN are under predicted. Overall, the present approach yields more accurate results than NASTRAN. This is due to the fact the elements used in NASTRAN are based on first-order shear deformation theories which only approximate the transverse stress.

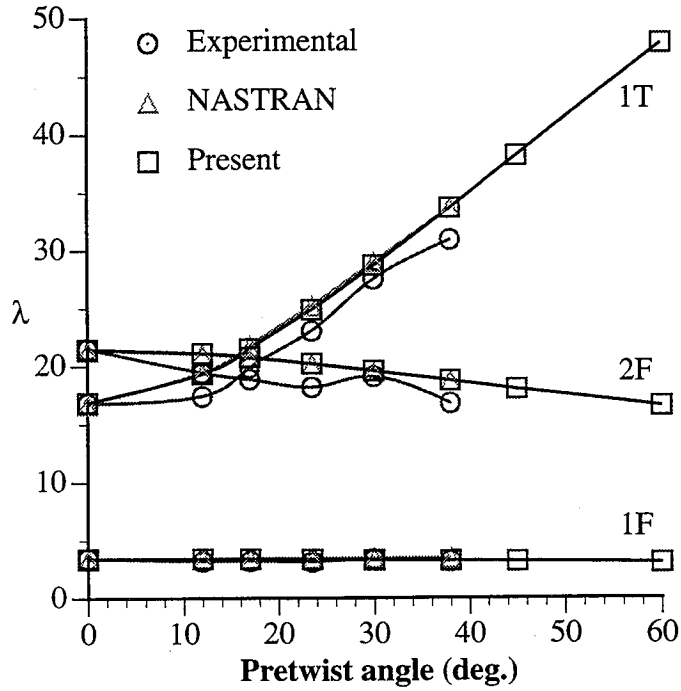

Fig. 4.5 Natural frequency as a function of tip twist (modes 1-3).

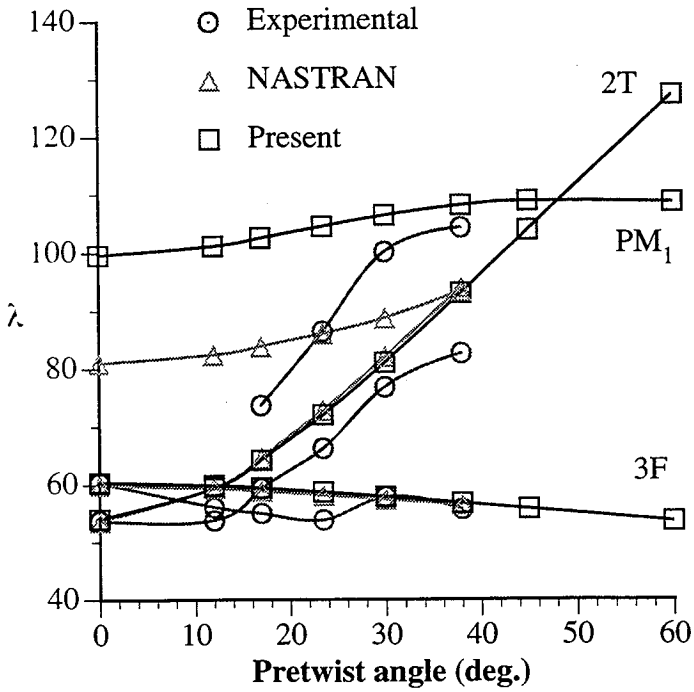

Fig. 4.6 Natural frequency as a function of tip twist (modes 4 - 6).

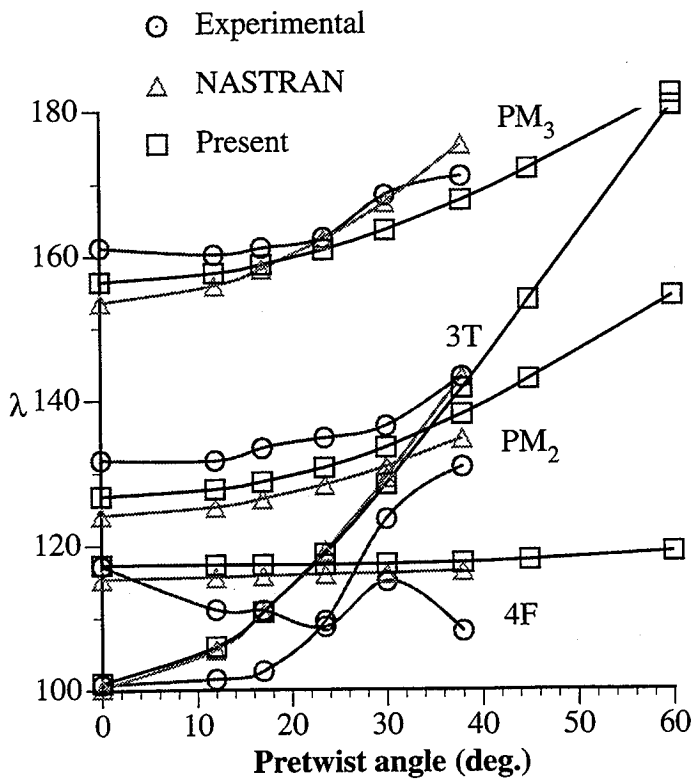

Fig. 4.7 Natural frequency as a function of tip twist (modes 7 - 10).

4.1.3 Vibration of thick, swept plates: To validate the higher-order theory for thick plates with sweep, the first eight nondimensionalized frequencies are calculated for several different plate configurations. The plate geometry is shown in Fig. 4.8 and plates with two different length-to-width ratios corresponding to a thick plate (a/b = 5) and a very thick plate (a/b = 2) are investigated. In both cases, three different width-to-thickness ratios (b/h = 0.5, 1 and 2) are used. The results obtained using the present approach are compared with two different numerical results which were presented by McGee and Leissa [109]. The first set of results in Ref. 109 were obtained using a three-dimensional Ritz solution in which a $6 \times 4 \times 4$ (288 degrees of freedom) mesh was used to discretize the displacement field. In addition, results were also obtained using NASTRAN solid elements (CHEXA) for a mesh size of $14 \times 14 \times 3$ (2520 degrees of freedom). It must be noted that both of these results represent truly converged results. In the present approach,

a mesh size of only 6 × 4 (269 degrees of freedom) is used which also represents converged results. Graphical results for the thick plate (a/b = 5) with a unit width-to-thickness ratio (b/h = 1) are presented in Figs. 4.9 - 4.16. The results from the other five cases are presented in Tables. 4.3 - 4.7.

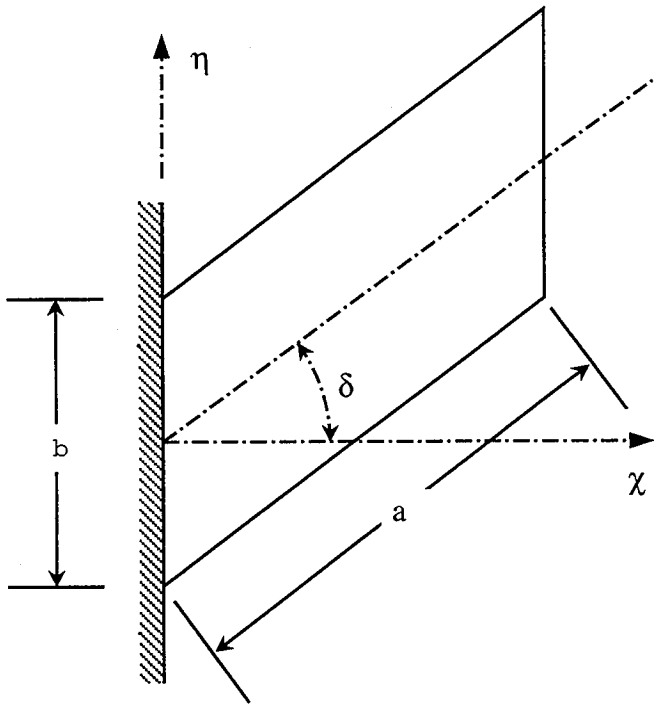

Fig. 4.8 Definitions of swept plate.

The first natural frequency of the thick plate with unit width-to-height ratio is shown in Fig. 4.9 from which several important observations are made. It is seen that increasing the sweep angle will increase the natural frequency. Also, all three techniques are in excellent agreement. The second natural frequency is presented in Fig. 4.10 and indicates that for zero sweep angle all three approaches are in very good agreement. With increases in the sweep angle, the natural frequency in case of the Ritz solution increases more rapidly than the other two techniques. This due to the fact the stress free boundary conditions on the edges of the plate are exactly satisfied in the Ritz solution. In both the NASTRAN results and the present approach these boundary conditions are not satisfied. In cases of moderate

sweep (up to 30°), the difference between the present approach and the Ritz solution is less than three percent. However, despite the fact that the NASTRAN solution involves an order of magnitude increase in the total degrees of freedom, the present approach is a better approximation to the Ritz solution.

Similar trends are observed in the higher-order modes (Figs. 4.11 - 4.16). In particular it observed that in general the natural frequency increases more dramatically with sweep in the Ritz solution than with the either the NASTRAN results or the present approach. In some cases, the natural frequency is slightly over predicted in the present approach for zero sweep. However, in all cases as the sweep angle increases the results using the present approach are as good or are better than NASTRAN despite the fact that the number of degrees of freedom used in NASTRAN is an order of magnitude larger than that used in the present approach. In addition to the results presented in Figs. 4.9 - 4.16, the results presented in Tables 4.3 - 4.7, for various plate thicknesses and length-to-width ratios, also show similar trends. From all of these results, the adequacy of the higher-order theory to model very thick, swept plates is demonstrated.

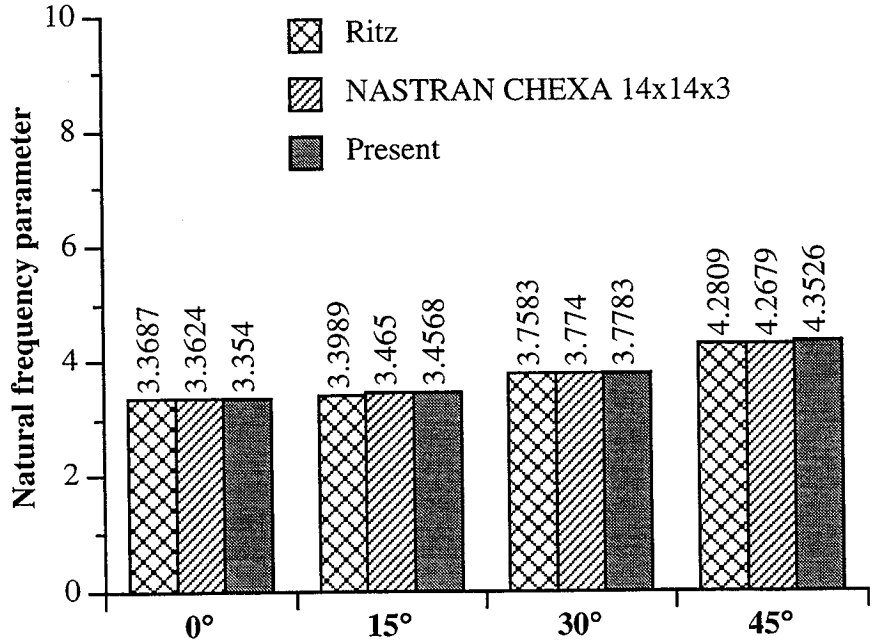

Fig. 4.9 Comparison of the natural frequencies of the first mode for thick, swept plates.

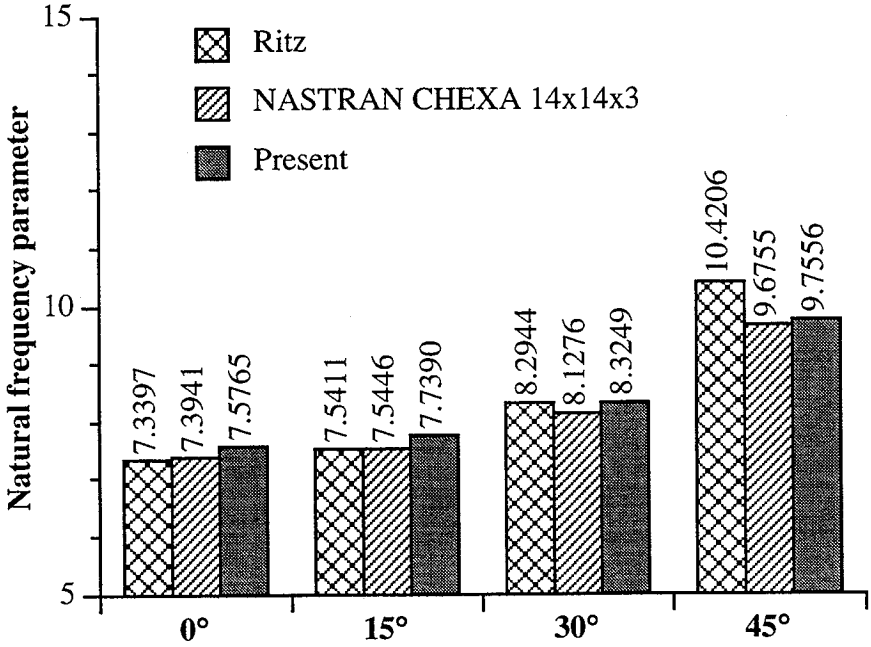

Fig. 4.10 Comparison of the natural frequencies of the second mode for thick, swept plates.

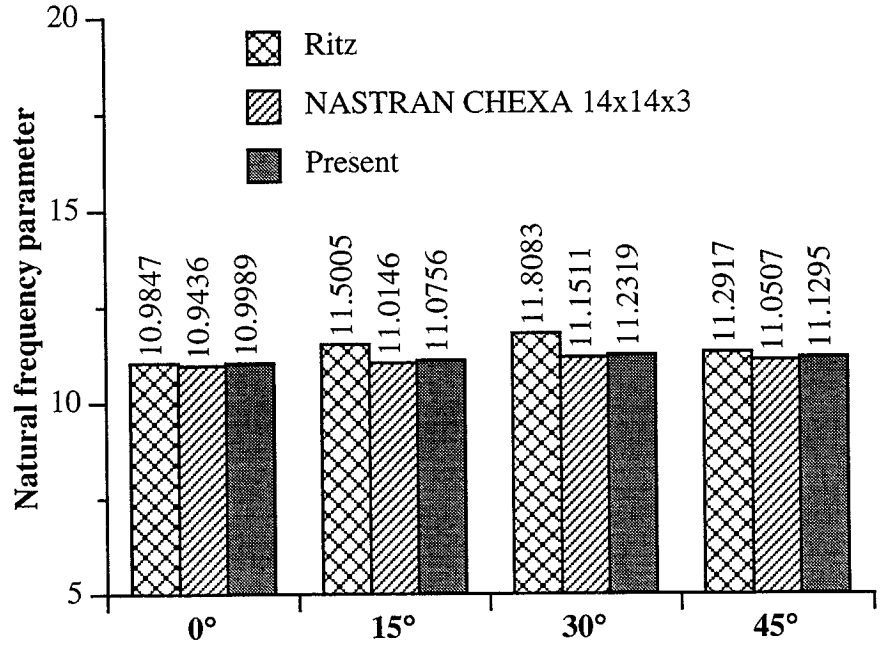

Fig. 4.11 Comparison of the natural frequencies of the third mode for thick, swept plates.

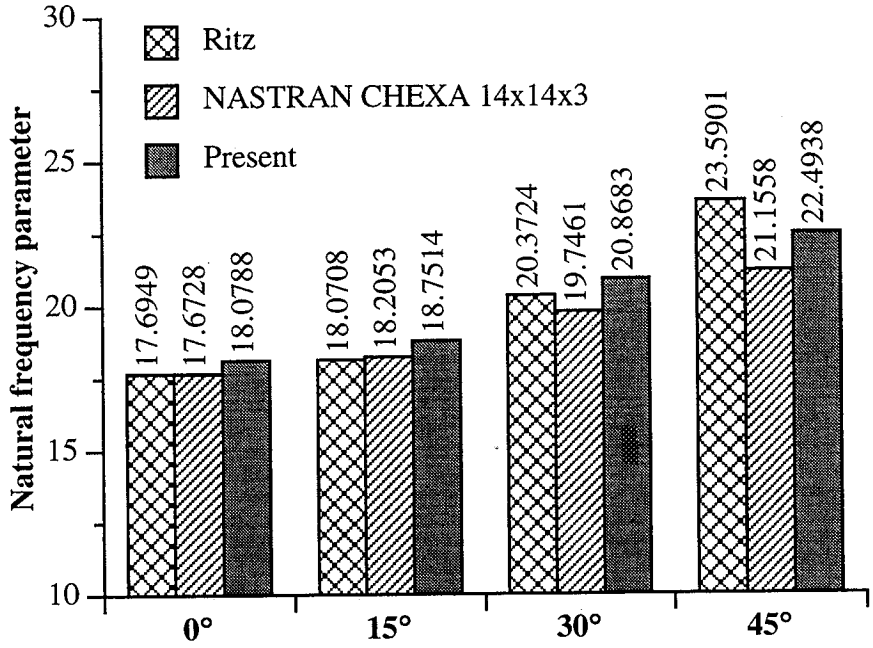

Fig. 4.12 Comparison of the natural frequencies of the fourth mode for thick, swept plates.

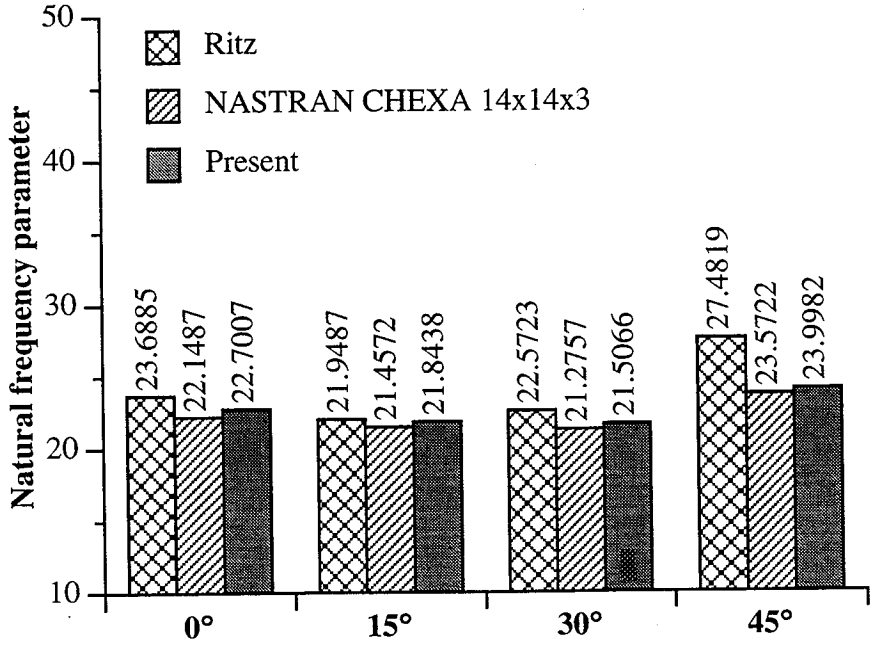

Fig. 4.13 Comparison of the natural frequencies of the fifth mode for thick, swept plates.

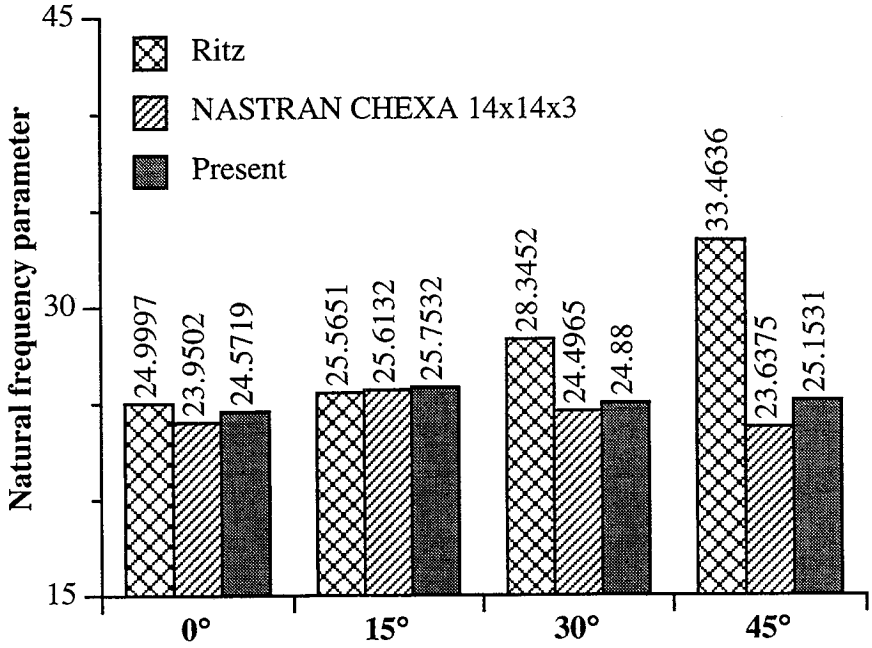

Fig. 4.14 Comparison of the natural frequencies of the sixth mode for thick, swept plates.

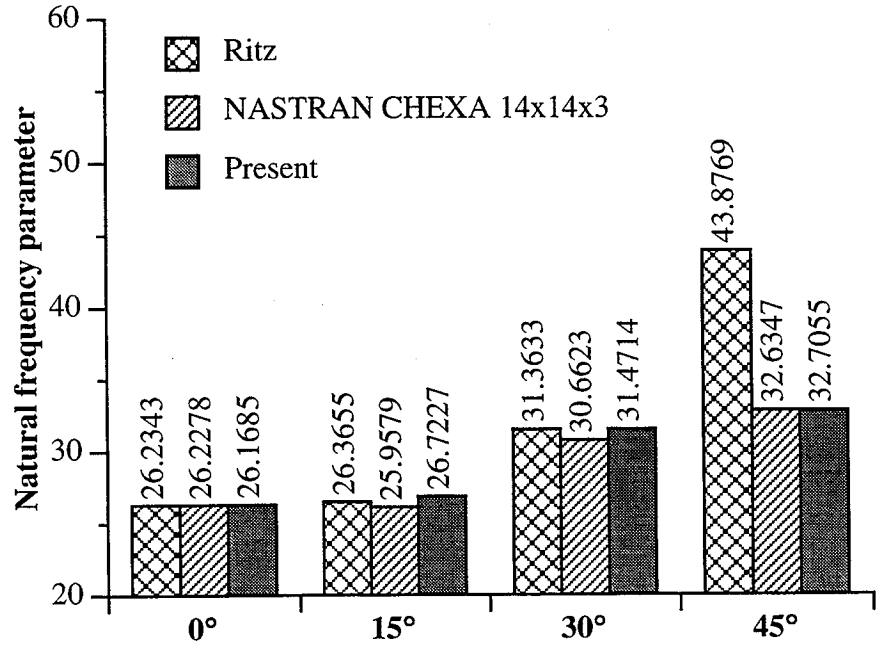

Fig. 4.15 Comparison of the natural frequencies of the seventh mode for thick, swept plates.

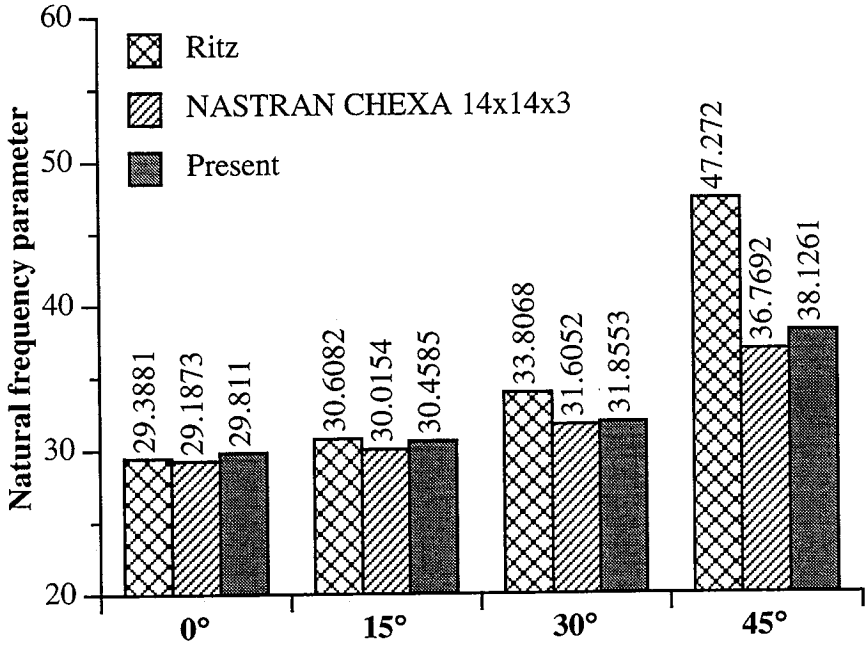

Fig. 4.16 Comparison of the natural frequencies of the eighth mode for thick, swept plates.

Table 4.3 Natural frequency parameters of thick, swept cantilevered plates; a/b = 0.5, b/h = 5

Analysis	Sweep Angle 0°	15°	30°	45°
Mode 1				
Ritz	3.1227	3.2166	3.5501	4.1425
Present	3.1054	3.2161	3.5459	4.0818
NASTRAN	3.1238	3.2217	3.4885	3.8582
Mode 2				
Ritz	4.2261	4.3542	5.0753	7.1414
Present	4.3052	4.4372	4.9293	6.2007
NASTRAN	4.2821	4.4073	4.9183	6.2958
Mode 3				
Ritz	6.8552	7.2038	8.2730	10.2007
Present	6.8642	6.9203	6.9706	6.5989
NASTRAN	6.7974	6.8581	6.9365	6.6924
Mode 4				
Ritz	8.0642	8.3654	9.3562	11.4351
Present	7.5768	7.7075	8.1924	9.4582
NASTRAN	7.3213	7.4760	8.0192	9.2653
Mode 5				
Ritz	12.6494	12.5656	13.3447	16.6312
Present	12.5927	12.1570	11.6274	11.7331
NASTRAN	12.5705	12.0459	11.4246	11.5358
Mode 6				
Ritz	12.9342	12.9723	14.7501	18.9970
Present	13.0389	13.1159	13.5085	15.1500
NASTRAN	12.9816	12.3409	12.7782	13.3430
Mode 7				
Ritz	13.5239	14.3488	17.1083	22.5717
Present	13.3894	13.6536	14.4809	15.7681
NASTRAN	13.3094	13.1870	13.5041	14.2523
Mode 8				
Ritz	13.9620	14.7390	17.7805	24.5030
Present	13.9822	14.1885	15.2488	16.4272
NASTRAN	14.4315	14.3078	15.1933	16.7757

Ritz solution $6 \times 4 \times 4$ mesh; present solution - 6×4 mesh; MSC/NASTRAN CHEXA values - $14 \times 14 \times 3$ mesh.

Table 4.4 Natural frequency parameters of thick, swept cantilevered plates; a/b = 2, b/h = 5

Analysis	Sweep Angle 0°	15°	30°	45°
Mode 1				
Ritz	3.3397	3.3432	3.0183	2.9961
Present	3.4077	3.4750	3.6810	4.0514
NASTRAN	3.4114	3.5002	3.7805	4.3144
Mode 2				
Ritz	12.4593	12.5382	12.7095	11.6690
Present	13.7012	13.9136	13.8973	12.8721
NASTRAN	13.2833	13.5085	13.8810	12.9673
Mode 3				
Ritz	14.3907	14.4765	15.4606	16.0299
Present	14.4754	14.3496	14.6975	16.4236
NASTRAN	14.4521	14.3258	14.4257	16.6212
Mode 4				
Ritz	19.5960	19.7466	20.6890	23.6116
Present	20.4807	21.2286	23.5735	28.1333
NASTRAN	20.3647	21.1291	23.4390	27.4966
Mode 5				
Ritz	38.7711	37.5107	35.3326	35.659
Present	43.3142	42.6169	42.2367	44.2161
NASTRAN	41.9086	41.6010	42.1593	46.0781
Mode 6				
Ritz	52.2825	49.9046	51.9786	64.1992
Present	52.2598	51.1111	49.4186	47.6519
NASTRAN	52.3346	50.6122	48.6333	47.2957
Mode 7				
Ritz	52.4692	50.3584	55.3036	68.8087
Present	54.4937	57.2897	59.9279	61.6180
NASTRAN	53.4834	55.9763	59.9545	62.1115
Mode 8				
Ritz	54.8140	54.0790	57.9550	71.5920
Present	55.8318	57.3844	64.8321	75.3250
NASTRAN	54.7376	56.9011	62.7143	72.3215

Ritz solution $6 \times 4 \times 4$ mesh; present solution - 6×4 mesh; MSC/NASTRAN CHEXA values - $14 \times 14 \times 3$ mesh.

Table 4.5 Natural frequency parameters of very thick, swept cantilevered plates; a/b = 1, b/h = 2

Analysis	Sweep Angle 0°	15°	30°	45°
Mode 1				
Ritz	2.9463	3.0096	3.3164	3.8412
Present	2.9402	3.0113	3.2317	3.6310
NASTRAN	2.9397	3.0017	3.1809	3.4554
Mode 2				
Ritz	4.4178	4.6232	4.6768	6.5555
Present	4.3996	4.4303	4.4928	4.4518
NASTRAN	4.3957	4.4244	4.4802	4.4421
Mode 3				
Ritz	5.1815	5.3635	6.1756	7.6914
Present	5.4081	5.5332	5.9641	6.9015
NASTRAN	5.1470	5.2527	5.6351	6.4876
Mode 4				
Ritz	10.5391	9.9399	11.3566	13.3667
Present	10.4674	10.3013	9.9520	9.5993
NASTRAN	10.5200	10.2640	9.8067	9.4300
Mode 5				
Ritz	10.9792	10.645	13.5265	18.6951
Present	11.4304	11.6097	12.044	12.3342
NASTRAN	10.7864	10.8493	10.9455	10.8145
Mode 6				
Ritz	11.7535	11.3436	13.5265	18.6951
Present	11.9244	12.1834	12.7421	13.0822
NASTRAN	11.6626	12.0043	12.6506	13.0694
Mode 7				
Ritz	14.4674	12.5292	14.3425	18.9918
Present	15.0781	14.4062	14.3705	15.3392
NASTRAN	14.3273	13.7176	13.6732	14.0382
Mode 8				
Ritz	16.1660	14.4180	15.9530	25.3940
Present	15.1308	16.3263	17.8745	18.7010
NASTRAN	14.4794	15.3277	16.5283	16.7953

Ritz solution $6 \times 4 \times 4$ mesh; present solution - 6×4 mesh; MSC/NASTRAN CHEXA values - $14 \times 14 \times 3$ mesh.

Table 4.6 Natural frequency parameters of very thick, swept cantilevered plates; a/b = 0.5, b/h = 2

Analysis	Sweep Angle 0°	15°	30°	45°
Mode 1				
Ritz	2.2304	2.2987	2.5790	3.1205
Present	2.2483	2.3041	2.4744	2.6396
NASTRAN	2.2375	2.2757	2.3791	2.5398
Mode 2				
Ritz	2.7039	2.8662	3.3293	4.1110
Present	2.7457	2.7681	2.7883	2.7899
NASTRAN	2.6884	2.7535	2.7861	2.6920
Mode 3				
Ritz	2.7577	2.8973	3.4345	4.8256
Present	2.7908	2.8774	3.1797	3.8379
NASTRAN	2.7289	2.7675	3.0452	3.4531
Mode 4				
Ritz	4.7438	4.8997	5.3477	6.6697
Present	4.6172	4.6900	4.6509	4.6932
NASTRAN	4.2550	4.2921	4.3260	4.3008
Mode 5				
Ritz	5.0722	5.0376	5.4416	6.8077
Present	5.0371	4.8628	4.9193	5.1200
NASTRAN	5.0096	4.8003	4.5566	4.5895
Mode 6				
Ritz	5.5855	5.8947	6.6160	8.1640
Present	5.5929	5.6647	5.5440	5.9195
NASTRAN	5.5375	5.1834	5.0861	5.3187
Mode 7				
Ritz	5.5932	5.9298	7.1205	9.7608
Present	5.6144	5.6754	6.0995	6.5709
NASTRAN	5.5698	5.8741	5.9334	5.4364
Mode 8				
Ritz	5.8219	6.1000	7.3500	10.0930
Present	5.7794	5.9215	6.4047	6.9770
NASTRAN	5.7046	5.7498	6.1511	6.5378

Ritz solution $6 \times 4 \times 4$ mesh; present solution - 6×4 mesh; MSC/NASTRAN CHEXA values - $14 \times 14 \times 3$ mesh.

Table 4.7 Natural frequency parameters of very thick, swept cantilevered plates; a/b = 2, b/h = 2

Analysis	Sweep Angle 0°	15°	30°	45°
Mode 1				
Ritz	3.2545	3.2823	3.2943	3.3134
Present	3.2684	3.3259	3.5032	3.8267
NASTRAN	3.2667	3.3220	3.4865	3.7563
Mode 2				
Ritz	5.7869	5.8978	5.9928	6.6404
Present	5.7902	5.7398	5.5589	5.1488
NASTRAN	5.7970	5.7466	5.5692	5.2041
Mode 3				
Ritz	9.9090	9.8656	10.4693	11.0825
Present	10.5107	10.6933	11.3024	12.5047
NASTRAN	9.9270	10.0899	10.6543	11.8026
Mode 4				
Ritz	16.3311	16.3082	17.4151	19.7762
Present	16.8113	17.1731	18.2583	19.0607
NASTRAN	16.4537	16.7024	17.3983	18.3928
Mode 5				
Ritz	20.9459	20.9449	21.8063	25.7577
Present	20.9039	20.4445	19.7675	20.0736
NASTRAN	20.9648	20.2626	19.4645	18.9263
Mode 6				
Ritz	21.9266	23.563	25.7634	32.3171
Present	22.3327	22.9537	23.9712	24.6472
NASTRAN	21.8993	22.7818	24.0112	24.8581
Mode 7				
Ritz	29.5524	28.8472	30.5295	24.1152
Present	31.4764	31.2740	31.3982	33.0256
NASTRAN	29.5814	29.6120	30.1386	31.9981
Mode 8				
Ritz	37.2420	30.8320	34.8060	45.4330
Present	39.2395	40.5095	43.6541	40.7105
NASTRAN	37.4149	38.1270	39.7678	41.1186

Ritz solution $6 \times 4 \times 4$ mesh; present solution - 6×4 mesh; MSC/NASTRAN CHEXA values - $14 \times 14 \times 3$ mesh.

4.2 Static Thin-Walled Beam Verification Study

To validate the developed procedure, correlations are made with available experimental results on a thin-walled box beam [110] and a previously developed analytical model [59]. The analytical model developed in Ref. 59 is a one-dimensional thin-walled beam model, based on the Classical Laminate Theory (CLT). In this approach, the out-of-plane warping effects are determined using on a contour analysis. The details of the beams studied are presented in Table 4.8. The cross ply and symmetric beams are all subjected to two different loading conditions, a 1 lb. bending load at the tip and a 1 lb.-in. tip moment. The anti-symmetric beams are subjected to a 1 lb. axial load at the tip and a 1 lb.-in. tip moment.

4.2.1 Cross ply: The bending slope of the cross ply beam under a 1 lb. tip bending load is presented in Fig. 4.17, which compares the experimental data [110], the results of the quasi-analytical model [59] and the results from the present study. Further, results from a beam finite element model reported in Ref. 59 are also presented. As mentioned in Ref. 59, this two-dimensional finite element technique is as accurate as a full three-dimensional finite element model for the particular beams studied in that report. From Fig. 4.17, it is seen that all three modeling techniques under predict the bending slope of the cross ply beam. This can possibly be attributed to errors in the experimental results arising from fiber alignment problems that are typically encountered during fabrication and curing of the beam. A slight shift from the desired (0° and 90°) ply orientations can introduce additional coupling terms which will reduce bending stiffnesses, thereby increasing the bending slope. Overall, there is still good correlation between all three modeling techniques in this case. The twist angle of the cross ply beam due to a 1 lb.-in. tip moment is shown in Fig. 4.18. From the figure, excellent correlation is observed for both the quasi-analytical model [59] and the present approach. To further investigate the possible coupling with slightly shifted angle plies, the bending slope and elastic twist for the same loading conditions are

calculated for a "cross ply" $[6°/84°]_3$ beam. From the figures it is seen that both the bending slope (Fig. 4.19) and the elastic twist (Fig. 4.20) now correlate extremely well with the experimental results.

Table 4.8 Details of composite beams[59,110]

	Flanges		Webs	
	Top	Bottom	Left	Right
Cross Ply	$[0°/90°]_3$	$[0°/90°]_3$	$[0°/90°]_3$	$[0°/90°]_3$
Symmetric 15°	$[15°]_6$	$[15°]_6$	$[15°/-15°]_3$	$[15°/-15°]_3$
Symmetric 30°	$[30°]_6$	$[30°]_6$	$[30°/-30°]_3$	$[30°/-30°]_3$
Symmetric 45°	$[45°]_6$	$[45°]_6$	$[45°/-15°]_3$	$[45°/-45°]_3$
Anti-symmetric 15°	$[15°]_6$	$[-15°]_6$	$[15°]_6$	$[-15°]_6$
Anti-symmetric 30°	$[0°/30°]_3$	$[0°/-30°]_3$	$[0°/30°]_3$	$[0°/-30°]_3$
Anti-symmetric 45°	$[0°/45°]_3$	$[0°/-45°]_3$	$[0°/45°]_3$	$[0°/-45°]_3$

Length = 30 in., width = 0.953 in., depth = 0.53 in., ply thickness = 0.005 in, number of plies = 6, wall thickness = 0.030 in. Mechanical properties: $E_L = 20.59 \times 10^6$ p.s.i., $E_T = 1.42 \times 10^6$ p.s.i., $G_{LT} = 0.89 \times 10^6$ p.s.i., $\nu_{LT} = 0.42$. (Cross ply dimensions: width = 2.06 in., depth = 1.025 in.)

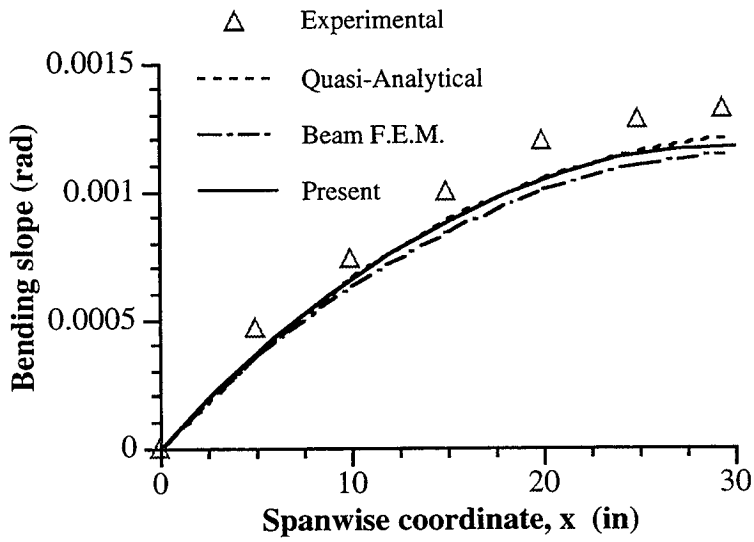

Fig. 4.17 Bending slope of cross ply beam under 1 lb. tip bending load.

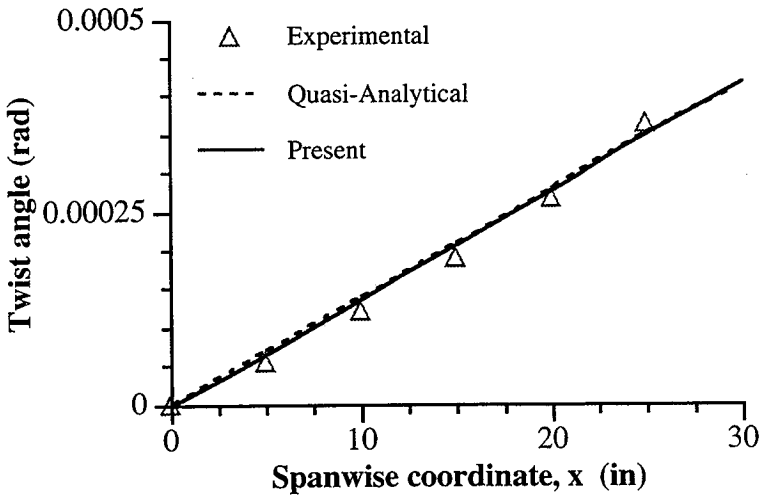

Fig. 4.18 Twist angle of cross ply beam under 1 lb.-in. tip moment.

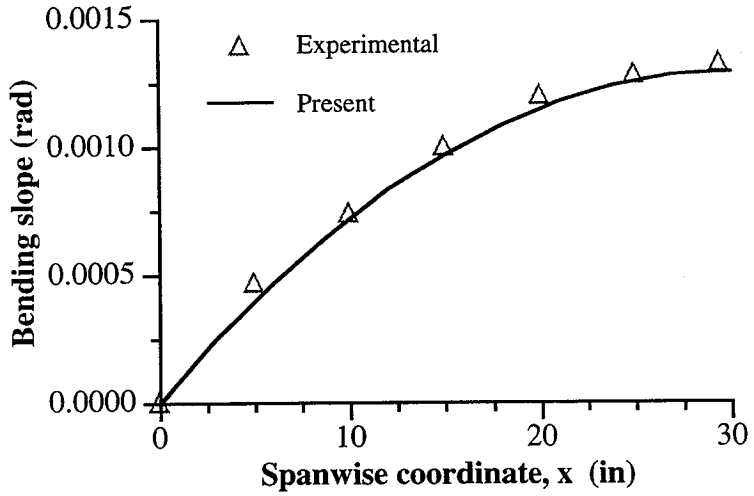

Fig. 4.19 Bending slope of "cross ply" $[6°/84°]_3$ beam under 1 lb. tip bending load.

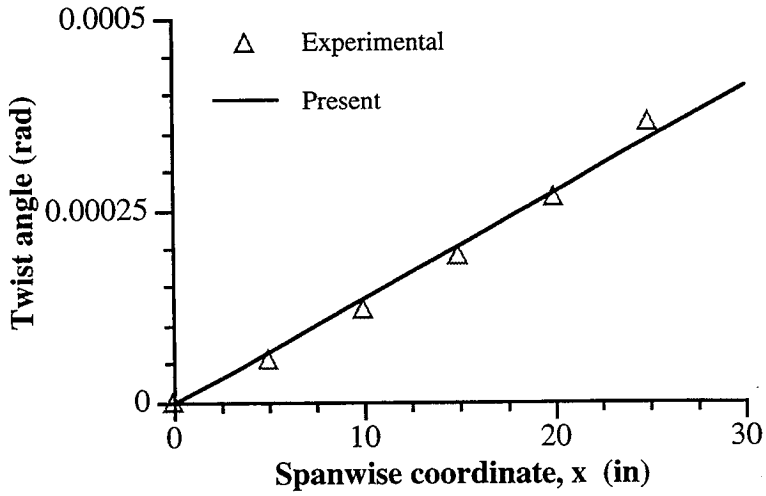

Fig. 4.20 Twist angle of "cross ply" $[6°/84°]_3$ beam under 1 lb.-in. tip moment.

4.2.2 Symmetric beams: The bending slope of the symmetric 15° beam under a 1 lb. tip bending load is presented in Fig. 4.21 where good correlation is observed between both modeling techniques. There are two sets of experimental data presented in this figure (as well as in the following figures) due to the fact that two separate beams were tested in Ref. 110. The induced twist due to tip bending load is presented in Fig. 4.22, which shows that the present approach slightly over predicts the twist angle at the tip compared to the quasi-analytical model of Ref. 59. Overall, both models show good correlation with the experimental data.

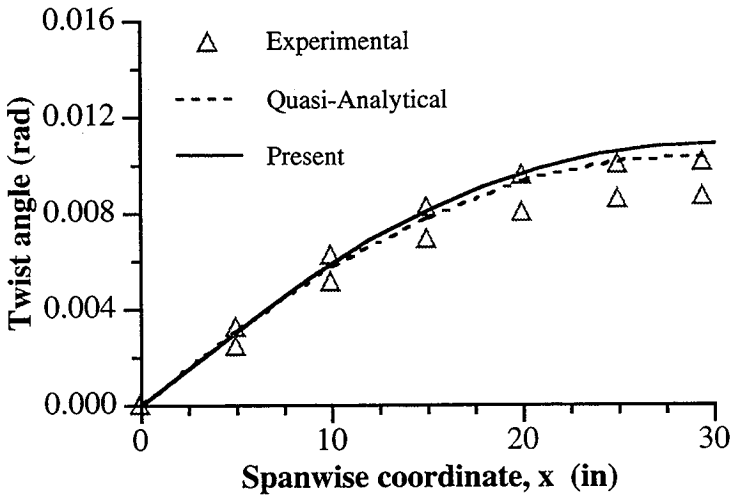

Fig. 4.21 Bending slope of symmetric 15° beam under 1 lb. tip bending load.

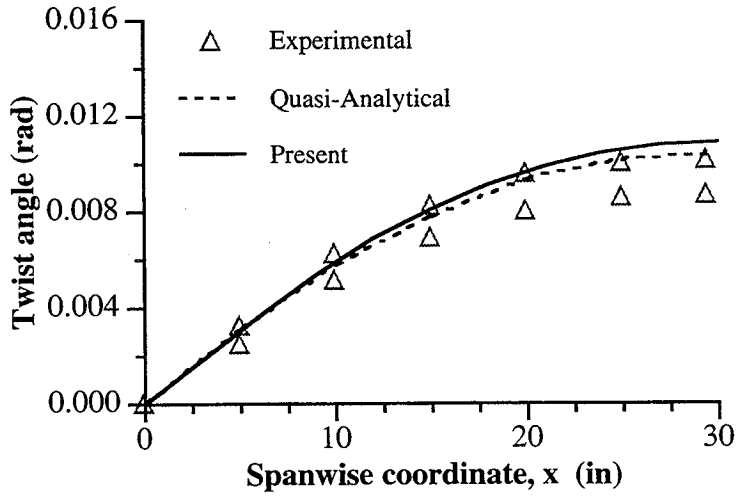

Fig. 4.22 Bending induced twist of symmetric 15° beam under 1 lb. tip bending load.

The bending slope of the symmetric 30° beam is presented in Fig. 4.23. This figure also shows the results from the beam finite element method presented in Ref. 59. From the figure it is observed that the quasi-analytical technique slightly under predicts and the present approach slightly over predicts the bending slope. The beam finite element method [59] over predicts the slope more significantly than the current approach. Once again, good correlation exists between all techniques. The induced twist due to bending load is presented in Fig. 4.24. The quasi-analytical technique again under predicts the response. The results from the present study correlate extremely well with the experimental data in this case.

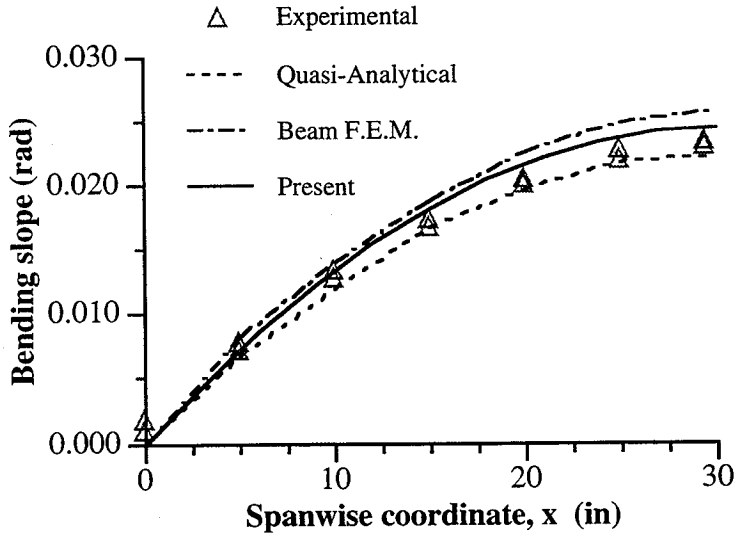

Fig. 4.23 Bending slope of 30° symmetric beam under 1 lb. tip bending load.

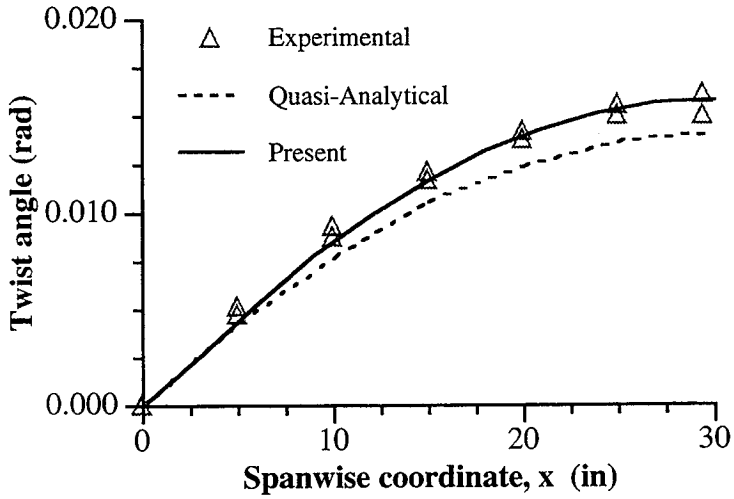

Fig. 4.24 Bending induced twist of 30° symmetric beam under 1 lb. tip bending load.

The results from the symmetric 45° beam subjected to a 1 lb. tip bending load are presented in Figs. 4.25 and 4.26. As shown in Fig. 4.25, the bending slope is slightly over predicted by the present model although the correlation with experimental data is still very good. The quasi-analytical technique [59] also correlates well. In case of the induced twist due to the bending load, the trends are significantly different (Fig. 4.26). The quasi-analytical method greatly under predicts the twist in this case while the present approach correlates extremely well with the experimental data. Further, the results are in excellent agreement with those predicted by the variational asymptotical approach (VABS) due to Cesnik et al. [69]. The approach reduces the cross-sectional properties into one-dimensional beam properties based on an expansion in terms of a small parameter which is defined to be the beam height divided by the beam length. The theory also includes both inplane and out-of-plane warping and is well suited for thin-walled box beams.

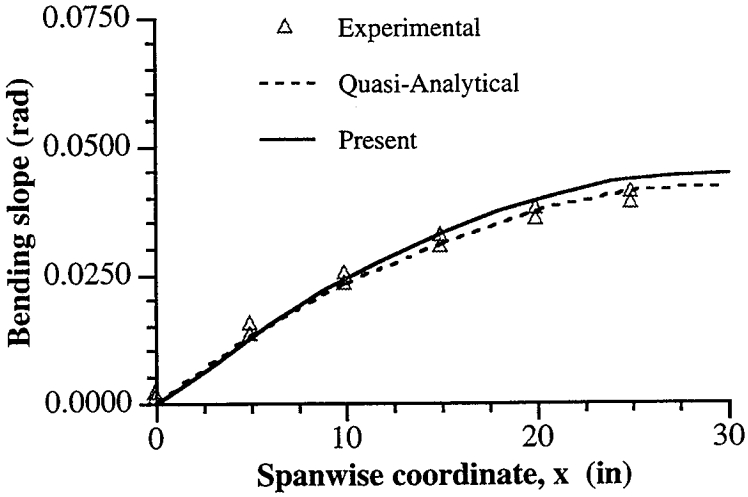

Fig. 4.25 Bending slope of $[45°]_6$ thin-walled beam under 1 lb. bending load at tip.

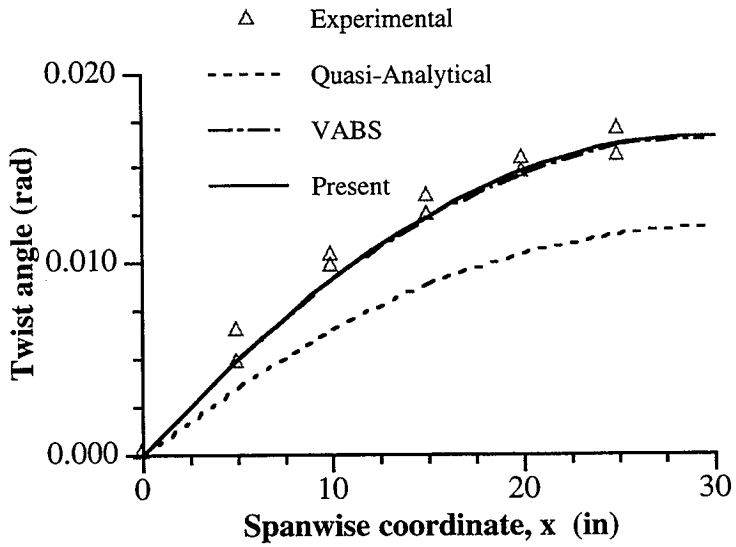

Fig. 4.26 Bending induced twist of $[45°]_6$ thin-walled beam under 1 lb. bending load at tip.

The results from the 1 lb.-in. tip moment loading case, for all three symmetric beams, are presented in Figs. 4.27 and 4.28. Since the variation of the response is linear, only the results at the mid span location (x/R = 0.5) are presented. From Fig. 4.27 it is seen that there is scattered correlation with the experimental bending slope, but it must be noted that the actual values of the slope are very small (on the order of 0.0005 rad). In case of the 15° symmetric beam, all three approaches over predict the slope when compared to the

experimental values. In case of the symmetric 30° beam, the present approach and the beam finite element method again over predict the slope, whereas the quasi-analytical method [59] correlates well with the experimental data. Finally, in case of the symmetric 45° beam, the quasi-analytical method greatly under predicts the slope whereas the beam finite element method and the present approach correlate very well. Overall, however, all three techniques show good correlation with the experimental data, particularly when the actual magnitude of the slope is taken into consideration. The comparisons of the twist angles are presented in Fig. 4.28. In case of the symmetric 15° beam, all three techniques slightly over predict the twist angle. However, in case of the symmetric 30° beam and the symmetric 45° beam, both the present approach and the beam finite element method correlate extremely well with the experimental data while the quasi-analytical technique significantly under predicts this behavior.

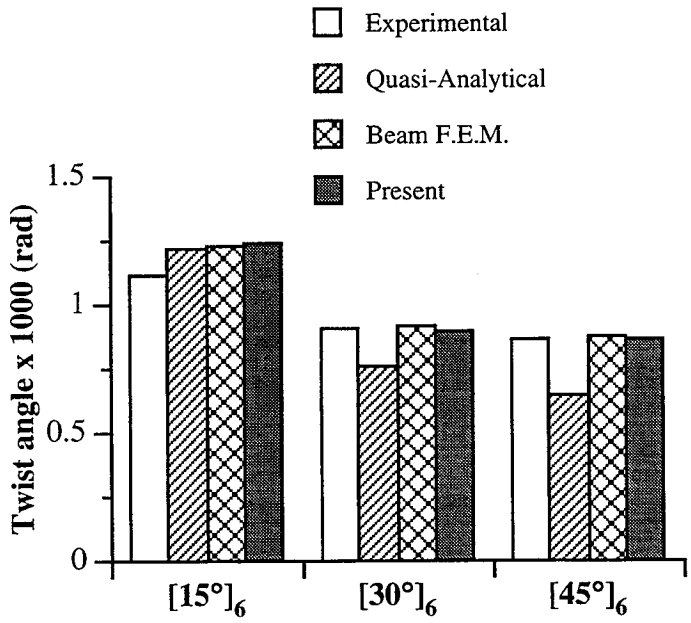

Fig. 4.27 Twist at x/R = 0.5 for 1 lb.-in. tip moment of symmetric beams.

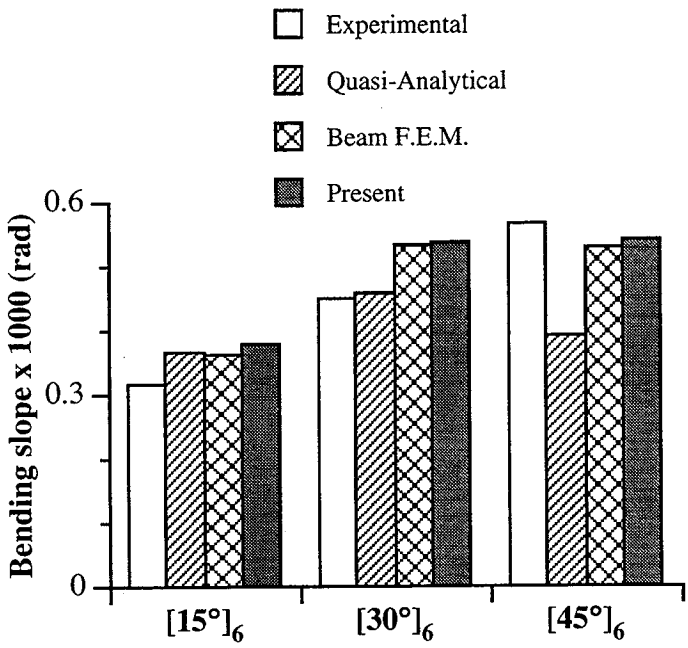

Fig. 4.28 Bending slope at x/R = 0.5 for 1 lb-in. tip moment of symmetric beams.

By examining Figs. 4.17 - 4.28, it is observed that the quasi-analytical model of Ref. 59 correlates well with experimental data for the cross ply beam and the 15° symmetric beam. In case of the 30° symmetric beam, the quasi-analytical model begins to under predict the behavior. This is particularly evident in Fig. 4.22 which presents the induced twist due to a 1 lb. tip bending load. The quasi-analytical method greatly under predicts the behavior of the symmetric 45° beam in all cases studied with the exception of the bending slope due to a 1 lb. tip bending load. It is also observed from these figures that although the present approach slightly over predicts the beam behavior for lower ply angles, the technique correlates very well with the experimental data in cases with larger ply orientations. Further, in cases where the present approach does over predict the behavior of the beam, compared to the experimental values, the beam finite element method [59] exhibits similar trends (Figs. 4.17, 4.27 and 4.28).

4.2.3 Anti-symmetric beams: The results from the three anti-symmetric beams (Table 4.8) are presented in Figs. 4.29 and 4.30. Since the response is linear, only the results at the mid span location are presented. As in Figs. 4.27 and 4.28, the actual magnitude of the twist angle, must be noted in these figures. The twist angle due to a 1 lb.-in. tip moment is presented in Fig. 4.29. In case of the 15° anti-symmetric beam, the quasi-analytical model, the beam finite element method and the present approach all correlate very well the experimental data. For the other two anti-symmetric beams, all three approaches predict very similar results, slightly under predicting the response compared to the experimental results. Similar trends are observed in Fig. 4.30 which presents the twist angle for a 1 lb. axial tip load. For the anti-symmetric 15° beam all three approaches slightly over predict the twist. However, all three approaches predict the behavior very well for the anti-symmetric 30° beam and the anti-symmetric 45° beam.

Overall, both the quasi-analytical model of Ref. 59 and the present approach correlate well with the experimental data in case of the anti-symmetric beams. Both techniques predict the same trends for all three beams. The present approach offers small improvements over the quasi-analytical results for the anti-symmetric 15° beam.

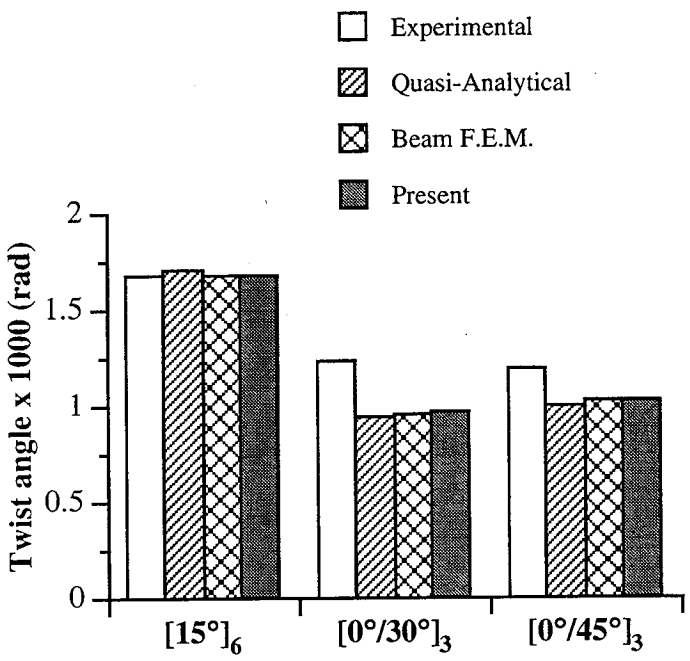

Fig. 4.29 Twist at x/R = 0.5 for 1 lb.-in. tip moment of anti-symmetric beams.

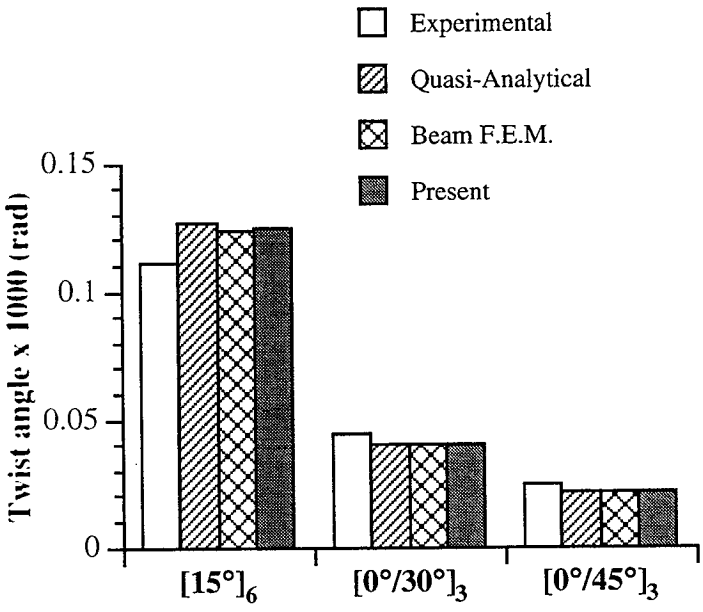

Fig. 4.30 Bending slope at x/R = 0.5 for 1 lb. tip axial load of symmetric beams.

4.3 Static Thick-Walled Beams Results

To demonstrate the importance of including transverse shear effects in the beam formulation, results are now presented for a series of thick-walled beams. Due to the lack of available experimental data, only numerical results are presented. Two different composite lay-ups are used which correspond to the symmetric 15° beam and the symmetric 45° beam (Table 4.8). The beams studied have a length-to-width ratio (L/c) of 2.5 and a width-to-height ratio (c/d) of 2. Since the goal is to investigate the effects of thick-walled beams, the wall thicknesses used in this study are 0.25 in. resulting in the values of the width-to-thickness ratio, c/h = 8, in the horizontal walls and the height-to-thickness ratio, d/h = 4, in the vertical walls. These two beam configurations are subjected to a 100 lb. bending load at the tip as well as a 100 lb.-in. tip moment.

Figure 4.31 presents the elastic twist for the thick-walled 15° symmetric beam subjected to a tip bending load. From the figure, it is observed that in addition to the fact that the local twist in the four individual walls is nonlinear, the average twist in each of the four walls is also nonlinear. This is different from the trends observed in case of the thin-walled beams where the local twists in the individual walls are nearly identical. In general, the local values of twist are very close to the average values which are presented in Fig. 4.27. Thus the average twist is a good representation of the beam twist for thin-walled beams. In the thick-walled case, however, the local twist differs significantly in the individual walls and as a results it is difficult to designate a value of "beam twist" for the entire cross section. Figure 4.31 also shows that the twist in the vertical walls are not equal to each other, while the twist in the horizontal walls are equal. This is due to the fact that the ply angles in the horizontal walls are all +15° (measured in the global, twisted coordinate system) and the two opposite walls are therefore mirror images of each other in their local coordinate systems. In the vertical walls, however, the stacking sequence in the opposite walls differs by a sign change (e.g. $\pm 15°$ in the right wall and $\mp 15°$ in the left wall). This

nonlinear trend is more observable in Figs. 4.32 and 4.33 which presents the induced twist of the symmetric 45° beam subjected to a tip bending load. In addition to the results obtained using the present approach, results obtained using NASTRAN are also presented. The NASTRAN results are obtained using QUAD4 plate elements which are elements based on first-order shear deformation theory. From Figs. 4.32 and 4.33, good correlation is observed between the present approach and NASTRAN in each of the walls. The nonlinear behavior of the vertical walls is more dominant in this case. The average twist for both approaches is presented in Fig. 4.34 where the correlation is again noted. In general, NASTRAN slightly over predicts the results compared to the present approach. This is due to the fact that only first-order shear deformation effects are included in the NASTRAN elements (QUAD4) used in this study.

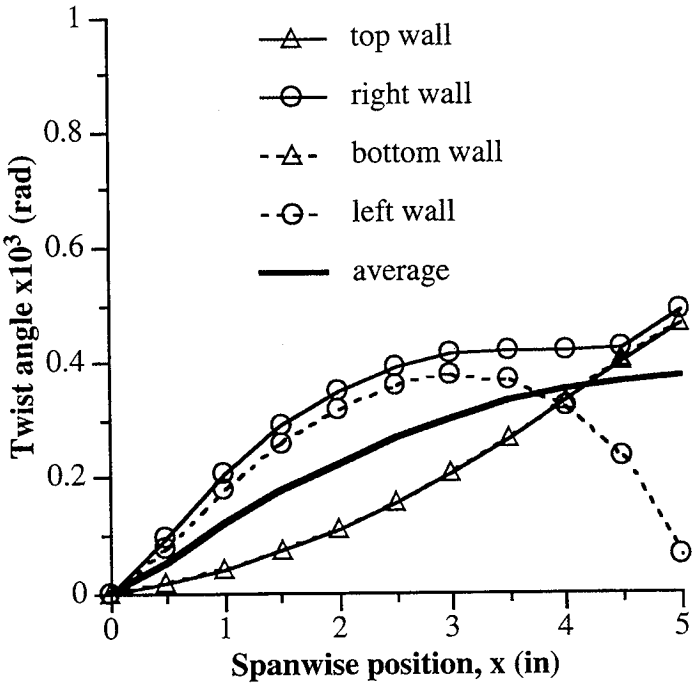

Fig. 4.31 Bending induced twist of thick-walled 15° beam under 100 lb. tip bending load.

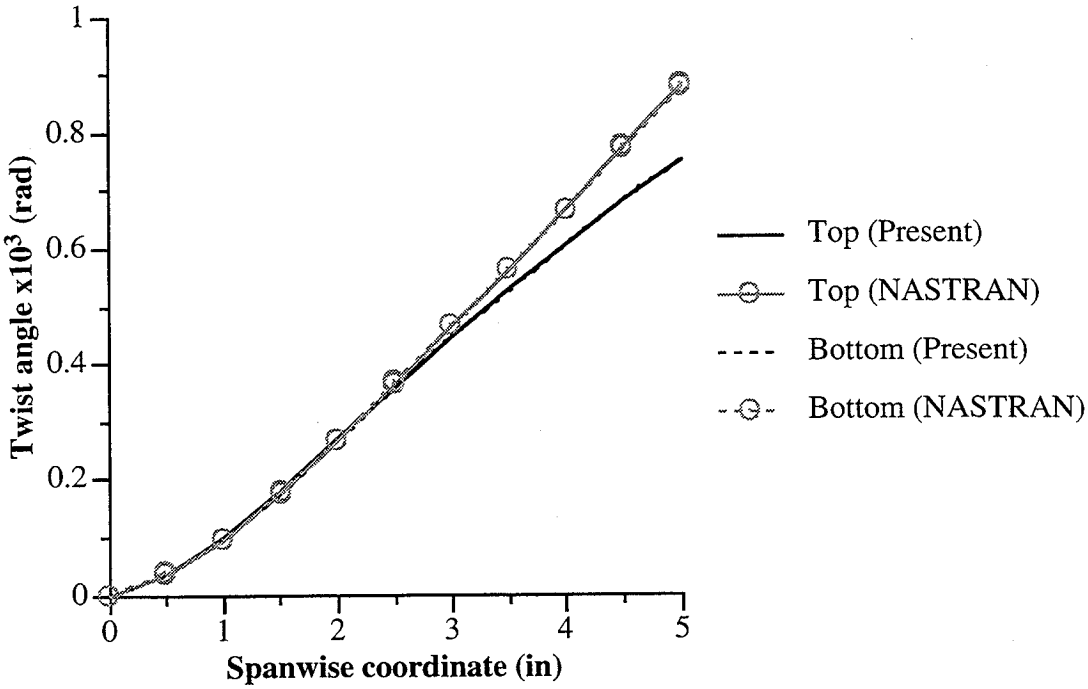

Fig. 4.32 Bending induced twist of thick-walled 45° beam under 100 lb. tip bending load; horizontal walls.

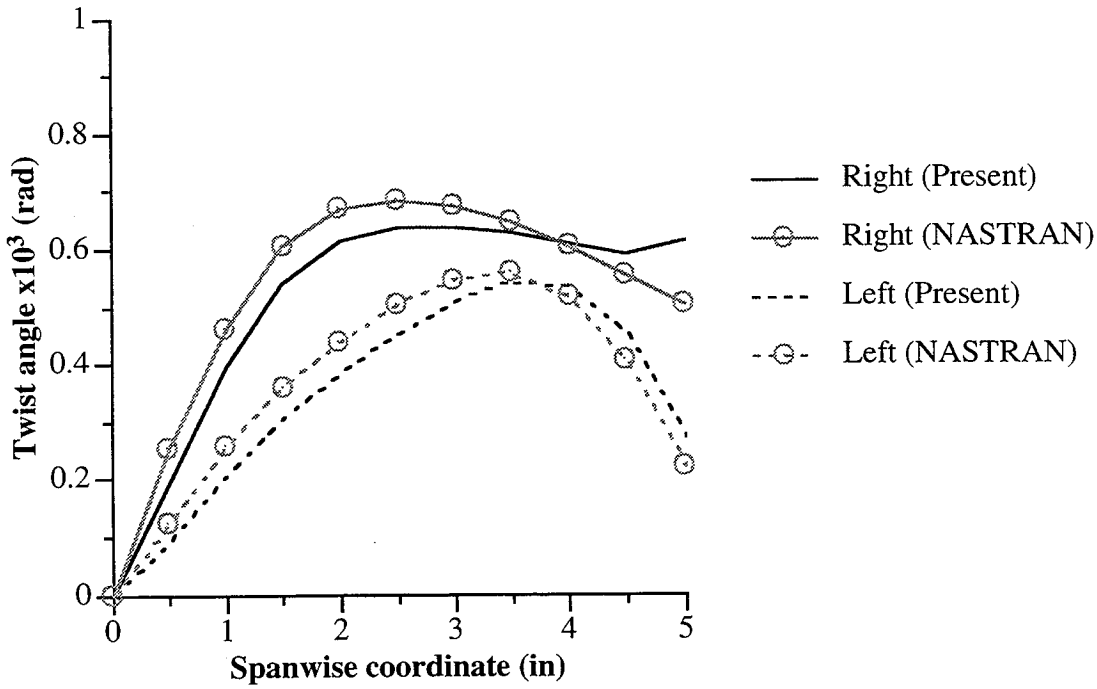

Fig. 4.33 Bending induced twist of thick-walled 45° beam under 100 lb. tip bending load; vertical walls.

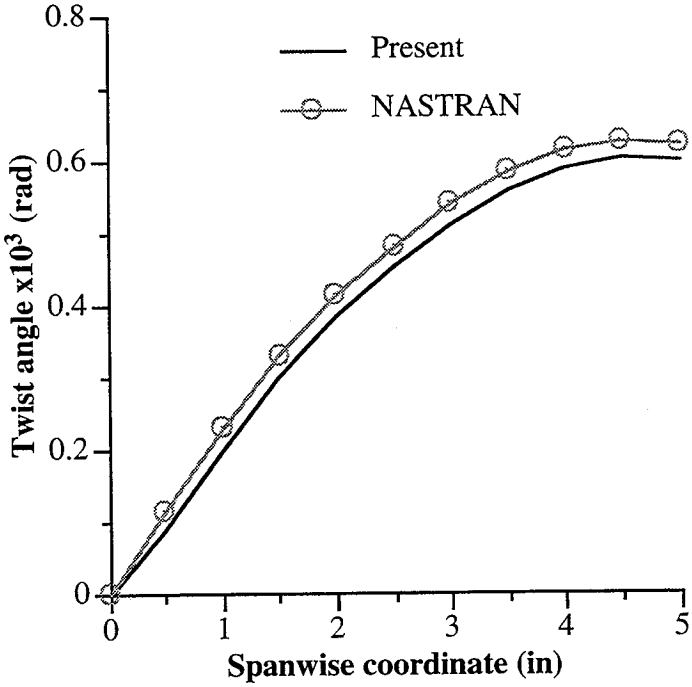

Fig. 4.34 Comparison of average bending induced twist of thick-walled 45° beam under 100 lb. tip bending load

A more complete explanation why the twist varies in each of the individual walls is presented in Figs. 4.35 - 4.37. Figure 4.35 shows the application of the tip bending load to the individual walls of the beam. In Fig. 4.36, a schematic diagram of the resulting displacements for unconnected walls (that is, individual plates) is shown where it is seen that displacements in the horizontal walls are described by a translation and a rotation. This is due to the fact that the plies in these walls are all of the same value (e.g. +45°) and therefore the laminate is unbalanced. Since both the vertical walls comprise balanced laminates (e.g. ±45°), there is no rotation in these walls and the displacement is purely translational. From Fig. 4.36 it is seen that the rotational displacement of the horizontal walls restricts the translational motion of the left vertical wall whereas the rotational motion in the horizontal walls is complimentary to the translational motion of the right wall. As a result, the horizontal walls become cambered which in turn induces large shearing stresses in the vertical walls. This type of bending behavior is shown in Fig. 4.37 which presents

the midplane deformation (greatly magnified) of the tip cross section for the 45° symmetric beam subjected to a tip bending load obtained using both the present approach and NASTRAN. Both techniques show shearing of the vertical walls and the cambering of the horizontal walls. Careful examination of Fig. 4.37 also reveals that the walls do not remain perpendicular to each other (at the corners) after deformation in case of the NASTRAN results. This is due to the fact that no such constraints are imposed in the NASTRAN formulation. In the present formulation, constraints are imposed on the rotations at the corners and the walls do remain perpendicular after deformation. This explains the increase in camber of the horizontal and the decrease in the transverse shear of the vertical walls when compared to the present results.

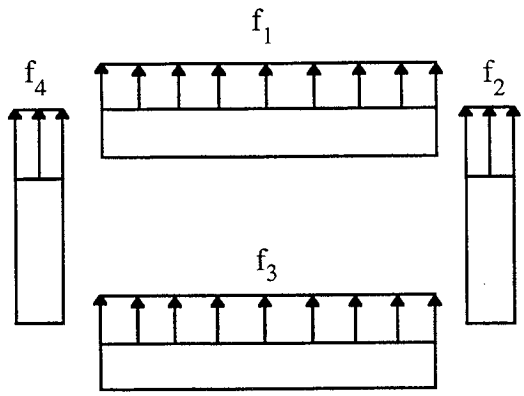

Fig. 4.35 Schematic of load distribution under tip bending load.

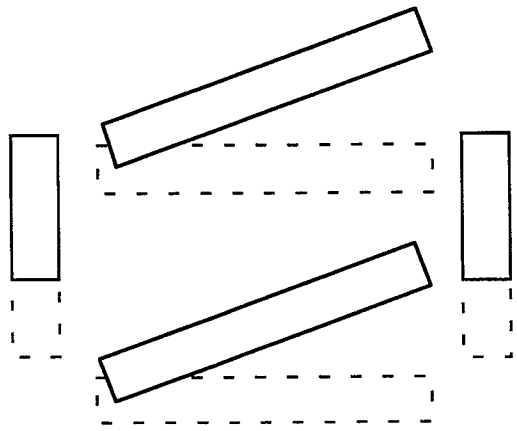

Fig. 4.36 Schematic of individual wall displacements under tip bending load.

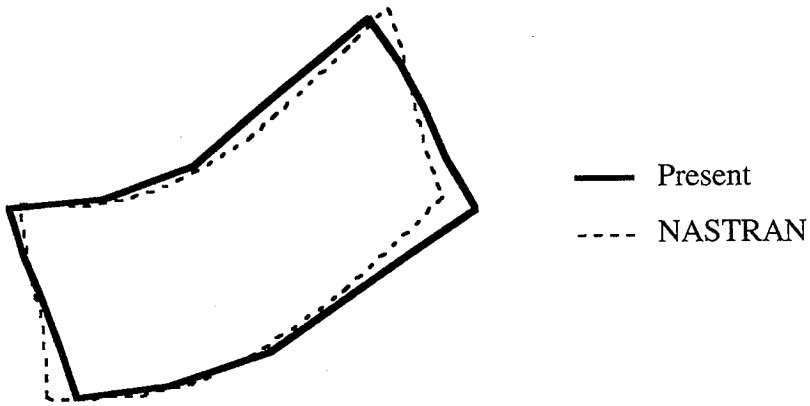

Fig. 4.37 Deformation of cross section at tip due to tip bending load; 45° beam.

The twist angle due to a 100 lb.-in. tip moment for the 15° symmetric, thick-walled beam is presented in Fig. 4.38. Similar trends as those obtained with the tip bending load are observed. In this case, however, the average twist of all four individual walls is very nearly linear. In comparison, in case of the thin-walled, symmetric 15° beam, the twist angle due to a 1 lb.-in. tip moment is linear in each of the four walls, except at the tip where the values are slightly larger for the horizontal walls compared to the vertical walls. The trends for the thick-walled beams are more observable in Figs. 4.39 and 4.40 which presents the twist angles of the thick-walled 45° symmetric beam due to a 100 lb.-in. tip moment for both the present approach. These figures also present the corresponding NASTRAN results. A comparison of the average twist using both techniques is presented in Fig. 4.41. Good correlation is observed from these figures. The small differences are once again attributed to the fact that QUAD4 elements used in NASTRAN only includes first-order shear deformation effects and the lack of constraints at the corner rotations in the NASTRAN formulation.

The results presented above indicate the importance of including transverse shear effects in the beam formulation. Further, the results also show that in general the twist of a composite beam is a local quantity which can be defined only locally, at a point. The definition of the twist at the centroid of a beam (or some other arbitrary point) is an approximation which in case of thick-walled sections can be erroneous.

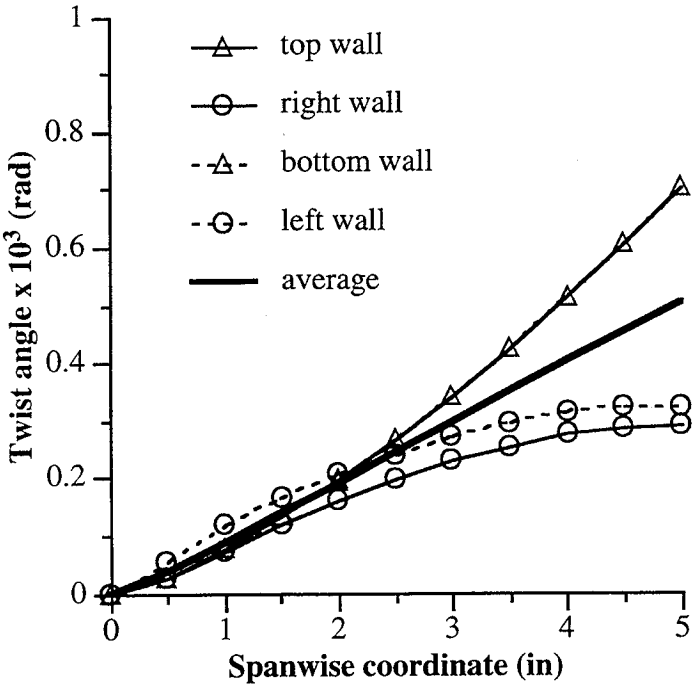

Fig. 4.38 Twist of thick-walled 15° beam under 100 lb.-in. tip moment.

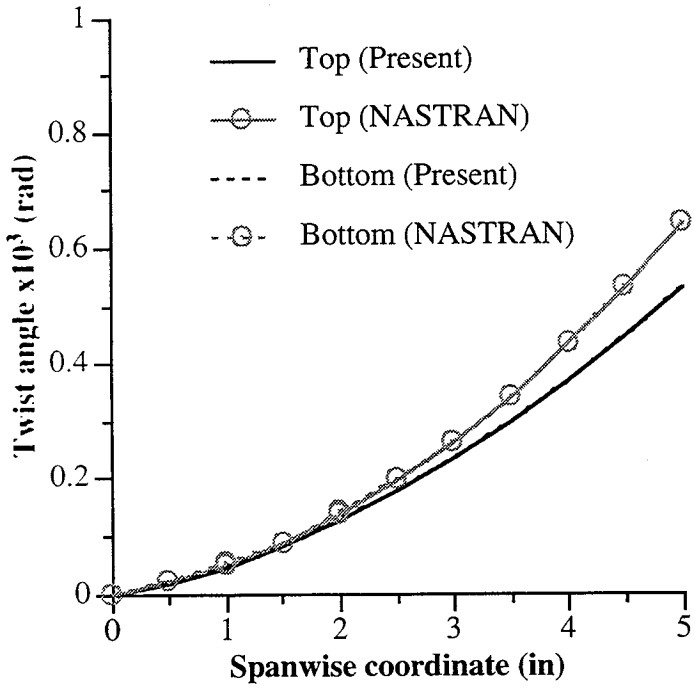

Fig. 4.39 Elastic twist of thick-walled 45° beam under 100 lb.-in. tip moment; horizontal walls.

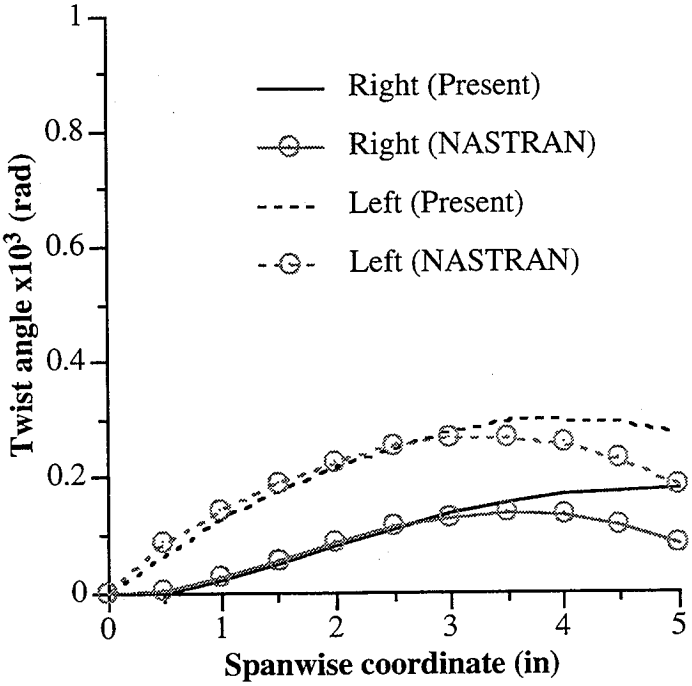

Fig. 4.40 Elastic twist of thick-walled 45° beam under 100 lb.-in. tip moment; vertical walls.

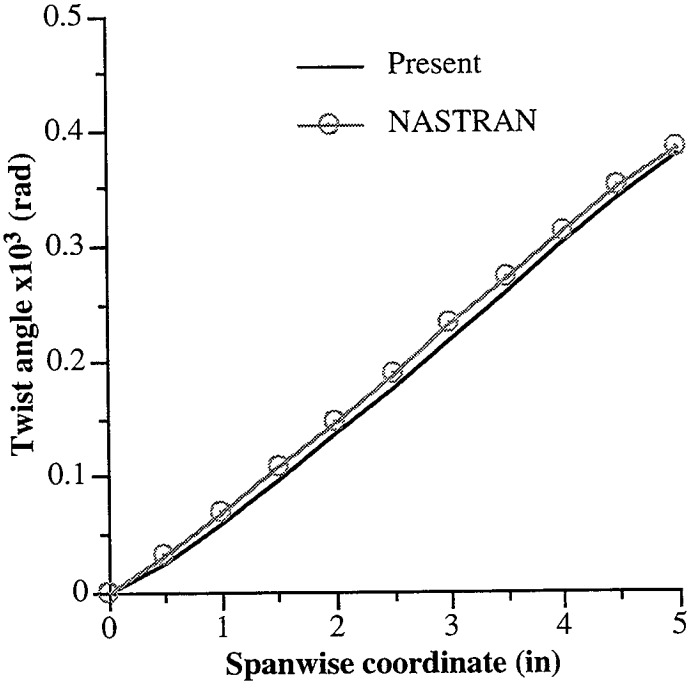

Fig. 4.41 Comparison of average elastic twist of thick-walled 45° beam under 100 lb.-in. tip moment.

4.4 Dynamic Results

In following sections, dynamic results for several different beam configurations are presented, including both thin-walled and thick-walled beams. Due to the lack of experimental data available, the results obtained using the present method are compared with those obtained using NASTRAN. In case of the composite beams, QUAD4 elements (first-order shear deformable) are used. In case of the thick-walled isotropic beam, both CHEXA (solid elements) and QUAD4 elements are used.

4.4.1 Thin-walled beams: The natural frequencies of the first several modes are calculated using the present approach and NASTRAN. These frequencies which are nondimensionalized as follows

$$\lambda_i = \omega_i \sqrt{\frac{\rho h L^4}{D}}, \tag{4.3}$$

$$D = E_1 h^3/12(1-\nu_{12}{}^2). \tag{4.4}$$

are presented in Table 4.9. The beam bending and chordwise bending modes are denoted 'B' and 'C', respectively, the torsional modes are denoted 'T' and extension modes are denoted 'E'. An element mesh size of 4×30 (each plate) is used in the present approach and since the NASTRAN elements are linear, a mesh size of 12×30 is used in each plate. From Table 4.9, very good correlation is observed between the predicted frequencies obtained using the present approach and NASTRAN. In general, the natural frequencies are slightly higher in case of the present model. This is once again due to the fact that a third-order displacement field is used in the present approach and the NASTRAN elements use only a first-order displacement field. Further, fairly significant differences observed in the torsional frequencies, with the present model being more stiff torsionally. The higher natural frequencies predicted by the present approach (compared NASTRAN results) is due to the constraints imposed on the corner rotations which are not present in the NASTRAN

formulation. It must also be noted that the present approach predicts a purely inplane warping mode which occurs before the fifth chordwise bending mode and the second torsional mode. This mode is not captured with NASTRAN.

Table 4.9 Natural frequencies of symmetric, thin-walled 45° beam

Modes	Frequency Parameter	
	Present (4×10 mesh)	NASTRAN (QUAD4, 12×30 mesh)
B1	27.57	27.05
C1	47.79	46.98
B2	172.32	169.12
C2	297.23	292.48
B3	480.13	472.39
C3	822.92	812.08
B4	930.75	921.98
T1	1458.03	1301.71
B5	1498.28	1514.79
C4	1581.34	1570.51
E1	1735.09	1718.58
Warp	2363.50	N.A.
C5	2553.36	2568.33
T2	3354.10	3388.66

To demonstrate the effect of inplane and out-of-plane warping on beam dynamic deformation, several mode shapes are presented for the 45° symmetric composite beam studied in Ref. 110. Due to the stacking sequence of this composite beam (Table 4.8), flap-lag coupling is absent. However, both bending-torsion coupling and extension-shear coupling are present. Further, since the beam consists of only ±45° plies, it is extremely rigid in torsion and the first torsional natural frequency (ω_{t_1}) is 52.8 times the fundamental natural frequency (ω_o = 18.83 Hz). As a result, there is no warping, either inplane or

out-of-plane, in the first five beam bending modes (ω_{b5} = 54.3 ω_1) and in the first four chordwise bending modes (ω_{c4}.= 57.4 ω_o). To illustrate the lack of coupling and/or warping in the first several modes, the fourth chordwise bending mode is shown in Fig. 4.42. (In these figures the dots denote the original undeformed shape of the beam.) However, there exists a purely inplane warping mode which occurs before the second torsion mode (ω_{t2} = 122 ω_o). This mode, whose natural frequency is 85.7 times the fundamental frequency, is illustrated in Fig. 4.43. It must be noted that this warping mode is not predicted by NASTRAN. The lack of significant out-of-plane warping for this composite beam is due to its thin-walled construction. Due to the very thin walls, the beam bending motion is accounted for by pure bending in the horizontal walls and the chordwise bending motion is accounted for by pure bending in the vertical walls. The bending motions are much larger than any inplane shear in the walls and as a result there is very little warping.

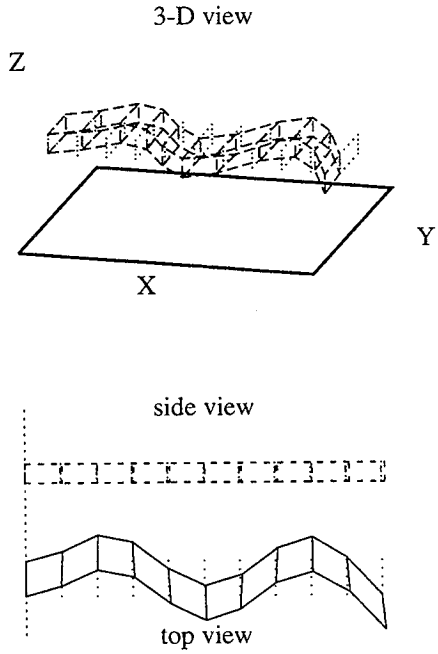

Fig. 4.42 Fourth chordwise bending mode of $[45°]_6$ thin-walled beam.

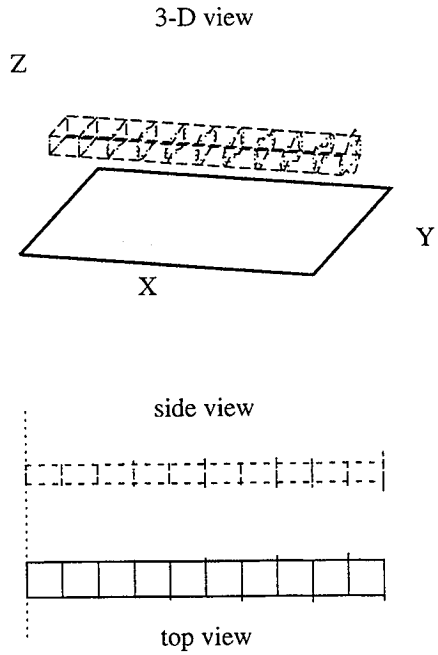

Fig. 4.43 Inplane warping mode of $[45°]_6$ thin-walled beam.

4.4.2 Pre-twisted thin-walled beams: In addition to the beams studied in Refs. 59 and 110, the frequencies and mode shapes are also presented for the symmetric, 45° beam with a 30° twist from root to tip. Table 4.10 presents the nondimensionalized frequency parameters obtained using both the present approach and NASTRAN. From the table it is seen that there is good correlation between the two approaches, although the present approach predicts slightly higher values in general. Similar trends as those of the untwisted beam are noted in this case. The differences are once again attributed to the different elements being used in the formulation. The current approach models the transverse strains more accurately than NASTRAN and exactly satisfies the stress free boundary conditions on the inner and outer surfaces of the beam. As is the case for the untwisted beam, a purely inplane warping mode is predicted using the present approach. This mode which

occurs before the second torsion mode (and fourth chordwise mode) is not predicted by NASTRAN.

Interesting mode shapes for the pre-twisted beam are presented in Figs. 4.44 - 4.46. Unlike the untwisted beam which displays very little coupling between bending modes, the pre-twisted beam starts to exhibit coupling between beam bending and chordwise bending as early as the first two modes ($\omega_{b1} = \omega_o$ and $\omega_{c1} = 1.56\ \omega_o$, $\omega_o = 20.5$ Hz). This coupling is more significant in the second bending modes which are presented in Fig. 4.44 ($\omega_{b2} = 5.79\ \omega_o$) and Fig. 4.45 ($\omega_{c2} = 9.54\ \omega_o$) despite the fact that their natural frequencies are not close to each other. Similar to the untwisted beam, a purely inplane warping mode exists for the pre-twisted beam with a natural frequency of 77.4 times larger than the fundamental frequency as shown in Fig. 4.46. This mode which occurs before the second torsional frequency ($\omega_{t2} = 109\ \omega_o$) is again not captured by NASTRAN.

Table 4.10 Natural frequencies of symmetric, thin-walled 45° beam with 30° pre-twist

Modes	Frequency Parameter	
	Present (4×10 mesh)	NASTRAN (QUAD4, 12×30 mesh)
B1	30.60	27.10
C1	47.66	46.64
B2	177.17	170.72
C2	292.07	287.89
B3	485.96	479.92
C3	811.72	788.35
B4	941.58	948.29
T1	1410.57	1295.00
B5	1483.31	1457.52
C4	1595.27	1627.26
E1	1735.09	1719.61
Warp	2367.11	N.A.
C5	2731.88	2598.25
T2	3354.22	3341.20

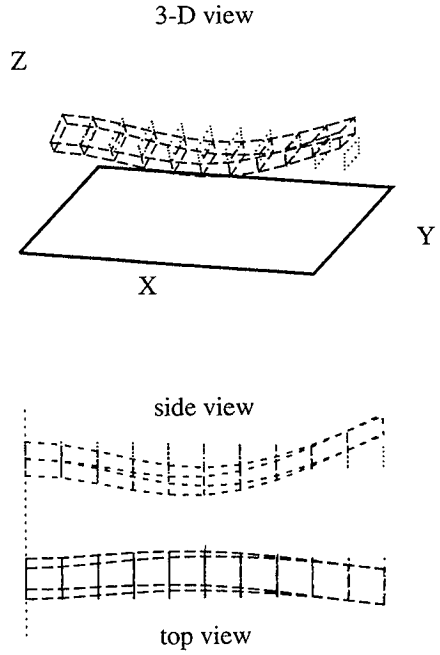

Fig. 4.44 Second beam bending mode of $[45°]_6$ thin-walled, pre-twisted beam.

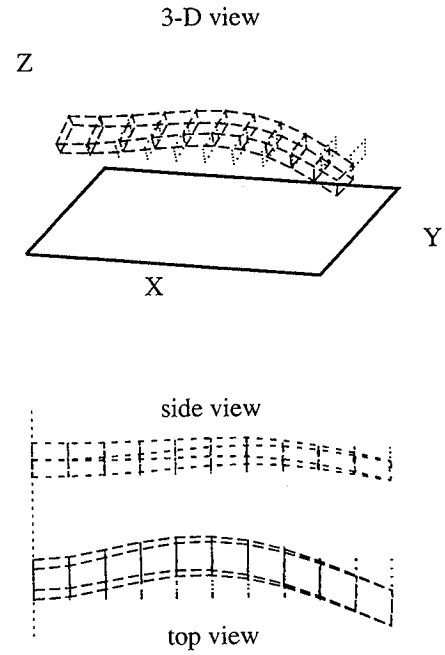

Fig. 4.45 Second chordwise bending mode of $[45°]_6$ thin-walled, pre-twisted beam.

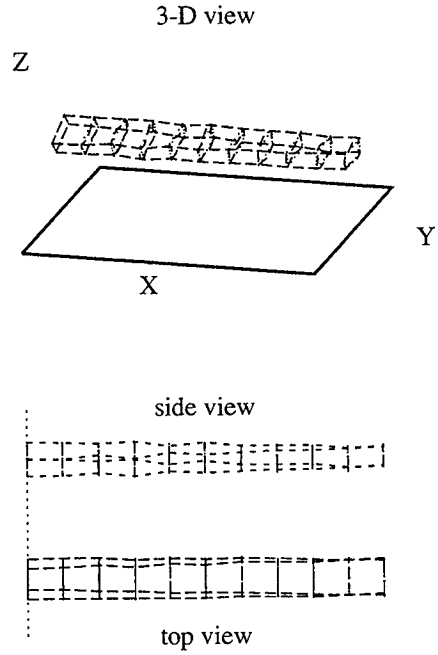

Fig. 4.46 Inplane warping mode of $[45°]_6$ thin-walled, pre-twisted beam.

4.4.3 Thick-walled beams: In addition to the beams studied in Refs. 59 and 110, natural frequencies and mode shapes are also presented for a thicker and shorter version of the beam with two different sets of material properties. Complete details of the thick-walled beams studied are listed in Table 4.11. The first set of material properties corresponds to an isotropic beam. The second beam is made of orthotropic laminae with identical lay-up and material properties as the symmetric 45° beam listed in Table 4.8.

Table 4.11 Details of moderately thick beam

Length = 10 in., width = 2 in., depth = 1 in., ply thickness = 0.0667 in., number of plies = 6, total wall thickness = 0.4 in.
Isotropic material properties
$E = 10 \times 10^6$ p.s.i., $\nu = 0.3$, $\rho = 0.1$ lb_m/in^3

The natural frequency parameters for both the present approach and for NASTRAN results are presented in Table 4.12. Since this beam has thicker walls, solid elements (CHEXA) are used to model the beam in NASTRAN. A $12 \times 30 \times 3$ mesh is used for a total of 17280 degrees of freedom. For comparison purposes, QUAD4 elements (12×30 mesh, 4320 degrees of freedom) are also used to calculate the frequencies. A 4×10 element mesh is used (1896 degrees of freedom) in the present approach. Good correlation is again observed between the present approach and NASTRAN CHEXA results although far fewer degrees of freedom are used in the present approach. The NASTRAN QUAD4 elements also correlate well with both the present approach and the solid (CHEXA) elements. In general, the solid elements predict slightly higher values of the bending frequencies and slightly lower values of the torsional and extensional frequencies when compared to the other two techniques. The present approach predicts slightly higher values compared to the QUAD4 elements. The differences in the torsional frequencies are again caused by the lack of rotation constraints at the corners of the beam in both NASTRAN results. For this beam, as was the case of thin-walled beams, the present approach does predict warping modes which are not predicted by either of the NASTRAN formulations. However, these modes occur only after the fifth torsional mode (T5) and as a result they are not presented in Table 4.12.

In the isotropic beam case, it is seen from Fig. 4.47 that out-of-plane warping is present as early as in the second chordwise bending mode ($\omega_{c2} = 10.5\ \omega_o$, $\omega_o = 313$ Hz). This is due to the presence of inplane shear in the side walls. The third torsional mode ($\omega_{t3} = 34.8\omega_o$) is presented in Fig. 4.48. A careful examination of this figure shows a small amount of both inplane and out-of-plane warping. This warping, which represents somewhat of a three-dimensional camber, is greatest near the node points. The camber effect is due to the shearing of the cross section.

Table 4.12 Natural frequencies of thick-walled isotropic beam

Modes	Frequency Parameter		
	Present (4×10 mesh)	NASTRAN (CHEXA, 12×30×3 mesh)	NASTRAN (QUAD4, 12×30 mesh)
B1	8.27	8.57	8.24
C1	16.30	16.53	16.24
B2	46.41	49.28	46.28
T1	74.29	60.75	61.18
C2	86.73	88.21	86.23
B3	114.74	124.02	114.34
E1	130.22	126.56	130.04
T2	197.03	179.82	178.06
B4	205.08	208.83	196.04
C3	216.61	215.51	203.33
T3	288.08	292.11	279.82
B5	289.18	316.45	286.29
C4	299.52	345.00	334.98
E2	356.81	378.49	367.09
C5	432.30	488.40	472.97

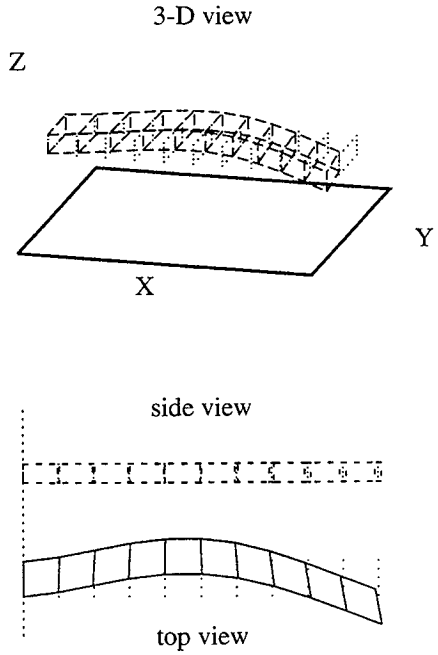

Fig. 4.47 Second chordwise bending mode of isotropic thick-walled beam.

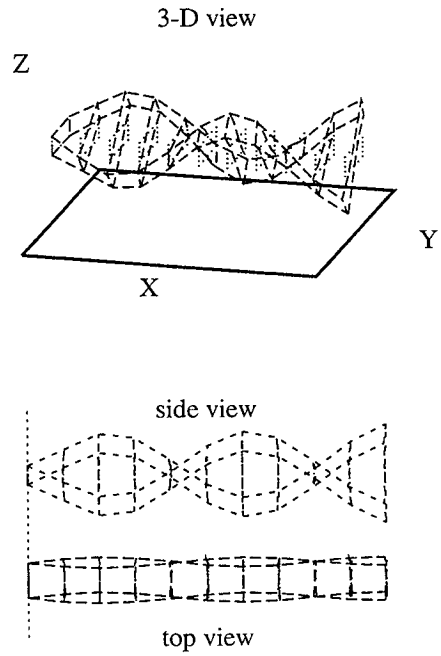

Fig. 4.48 Third torsion mode of isotropic thick-walled beam.

To investigate the effect of wall thickness on the warping of composite beams, natural frequencies and mode shapes are calculated for a thicker and shorter composite beam with cross-sectional dimensions that are approximately twice that of the symmetric 45° beam originally studied in Ref. 110. The length of this beam is one-third the previous beam. The laminate stacking sequence and material properties are identical to the previous beam (see Tables 4.8 and 4.11).

The natural frequency comparisons between the present approach and NASTRAN are presented in Table. 4.13 and show good correlation between the two techniques. It must be noted that although this beam does represent a thick-walled beam, QUAD4 (plate) elements are used. This is due to the fact that if solid elements (CHEXA) were used, each unique lamina would require a separate element. For this simple beam, that would require a discretization into 6 elements through the thickness of each wall. For more complex beams, this number would increase making the approach computationally expensive. Also numerical conditioning is an issue since very thin solid element do not behave very well [105]. Similar trends as those obtained in the previous three beams are again observed in this beam. In particular, the present approach predicts slightly higher natural frequencies for the lower modes and slightly lower natural frequencies for the higher modes compared to those predicted using NASTRAN. This is again due to the differences in the displacement field and the constraints on the corner rotations.

As in the previous beam, for the first several modes there is no coupling between the beam bending, the chordwise bending and the torsional modes. However, for this thicker beam, a slight out-of-plane warping effect is observed in the first chordwise bending mode (ω_{c1}), whose natural frequency is only 2.10 times larger than the fundamental frequency (ω_o = 224 Hz). The second chordwise bending mode (ω_{c2} = 13.5 ω_o) is shown in Fig. 4.49. A significant amount of out-of-plane warping is observed in this mode predominantly due to the shearing in the upper and the lower walls. Figure 4.49 also

shows that this mode is uncoupled, although its natural frequency is close to the first torsional mode ($\omega_{t1} = 11.5\ \omega_o$).

Table 4.13 Natural frequencies of thick-walled symmetric 45° beam

Modes	Frequency Parameter	
	Present (4×10 mesh)	NASTRAN (QUAD4, 12×30 mesh)
B1	2.77	2.70
C1	5.82	5.72
B2	16.67	16.28
T1	31.76	30.25
C2	37.32	31.25
B3	43.85	43.08
E1	44.16	43.47
B4	78.42	77.27
C3	79.76	77.48
T2	96.48	82.70
B5	102.50	114.11
T3	115.14	117.63
E2	117.29	127.22
C4	125.29	132.64
T4	128.73	145.54

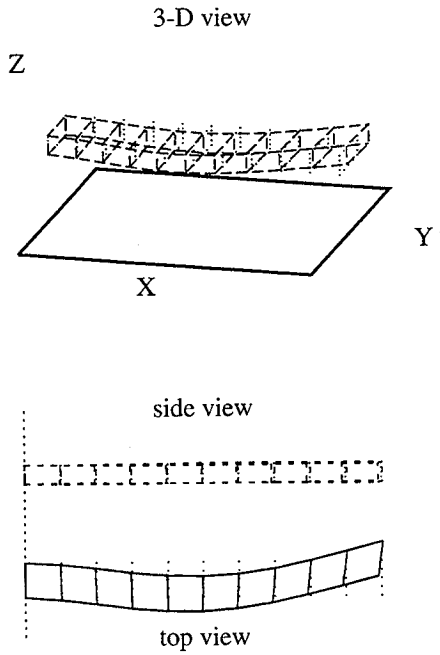

Fig. 4.49 Second chordwise bending mode of $[45°]_6$ thick-walled beam.

There is, however, a significant amount of coupling between the fourth beam bending mode (ω_{b4} = 28.3 ω_o) and the third chordwise bending mode (ω_{c3} = 28.8 ω_o). To illustrate this coupling, the third chordwise bending mode is shown in Fig. 4.50. This coupling, which is clearly due to the fact that their natural frequencies are very close, causes a significant amount of both inplane and out-of-plane warping as depicted in Fig. 4.50. Unlike the second chordwise bending mode which remains uncoupled from the nearby first torsion mode, the third chordwise bending mode is slightly coupled with the second torsion mode (ω_{t2} = 34.8 ω_o) as well as with the fourth beam bending mode.

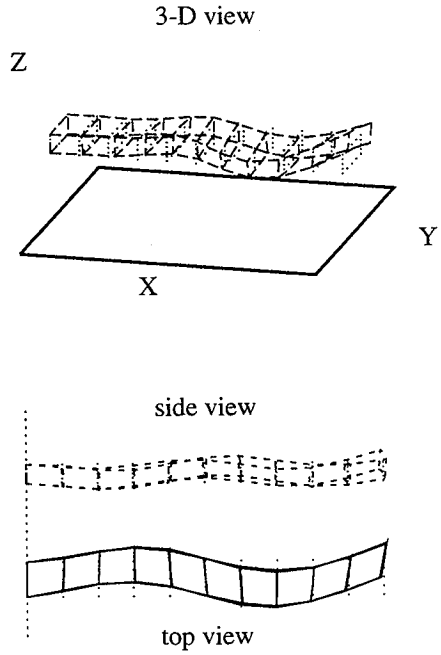

Fig. 4.50 Third chordwise bending mode of $[45°]_6$ thick-walled beam.

Finally, to illustrate the importance of including both inplane and out-of-plane warping in the beam formulation, the second extensional mode ($\omega_{e2} = 42.3\ \omega_o$) is presented in Fig. 4.51. A significant amount of warping in observed in this mode which is slightly coupled with the third torsion mode ($\omega_{t3} = 41.6\ \omega_o$) and is largely coupled with the fourth chordwise bending mode ($\omega_{c4} = 45.2\ \omega_o$). Unlike the previous modes which have primarily linear warping, both the inplane and the out-of-plane warping in this mode are nonlinear. Of particular interest is the "necking" effect observed near the cantilevered edge shown the side view and the nonlinear out-of-plane cross-sectional camber which is demonstrated in the top view. This three-dimensional warping is a result of the shearing effects and are significant due to the thick-walled construction of the beam.

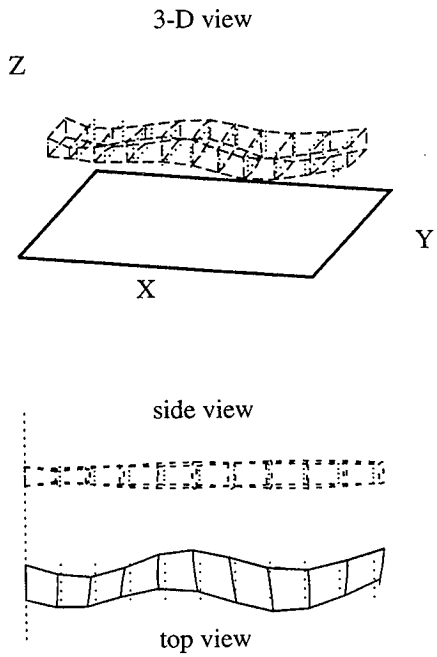

Fig. 4.51 Second extensional mode of $[45°]_6$ thick-walled beam.

5. Aerodynamic Modeling

The aerodynamic formulation is based on the two-dimensional compressible aerodynamic representation developed by Smith [111] and later modified by Talbot [112] for the formulation of axial flow performance analysis. The modifications by Talbot include an empirical correction to the two-dimensional stall behavior to represent the high lift capability demonstrated by rotors and propellers. In the initial study performed by Smith [111] an empirical fit was performed on NACA 63 and 64 series airfoil families in order to supply a functional relationship between maximum lift coefficient and sectional thickness and camber for incompressible flow. Detailed expressions for the coefficients of lift, drag and pitching moment (c_l, c_d and c_m), which represent the high lift capability of rotary wings in post stall angle of attack region, are found in Ref. 106. These functional relationships were later modified by Talbot [112] to model the Advanced Tiltrotor Blades (ATB) [113,114]. These relationships were then modified by McCarthy et al. [13] to include blade sweep. A similar algorithm was proposed to model the post stall delay due to rotation by Corrigan and Schillings [115]. In this study, the formulation is extended to include blade dynamic effects. The coefficients of lift, drag and the pitching moment, obtained using this analysis, are presented in Figs. 5.1 - 5.3 for a typical section of the Advanced Technology Blade over a range of Mach numbers.

5.1 Aerodynamic Loads

The blade element theory used in the algorithm is due to Glauert [116]. In this formulation, the sectional lift and drag are resolved into elemental thrust and torque for each section of the blade. The force and momentum equations for thrust and torque assume the following form.

$$dT_1 = 4\pi r\rho\left(V_\infty + \upsilon_i\right)\upsilon_i dr, \tag{5.1}$$

$$dT_2 = \frac{1}{2}\rho W^2 c\left(c_l \cos\Lambda - c_d \sin\Lambda\right)dr, \tag{5.2}$$

$$dQ_1 = 4\pi r^2 \rho (V_\infty + \upsilon_i) u_T dr, \tag{5.3}$$

$$dQ_2 = \frac{1}{2}\rho W^2 c(c_l \sin\Lambda + c_d \cos\Lambda) r dr, \tag{5.4}$$

where dT, dQ and dr represent the section thrust, torque and element length, respectively, V_∞ is the forward velocity, υ_i and u_T represent the inflow and swirl velocities, respectively and W is the magnitude of the resultant velocity. The chord length and radial locations are denoted c and r, respectively and ρ is the air density. The quantities c_l and c_d represent the sectional coefficients of lift and drag, respectively.

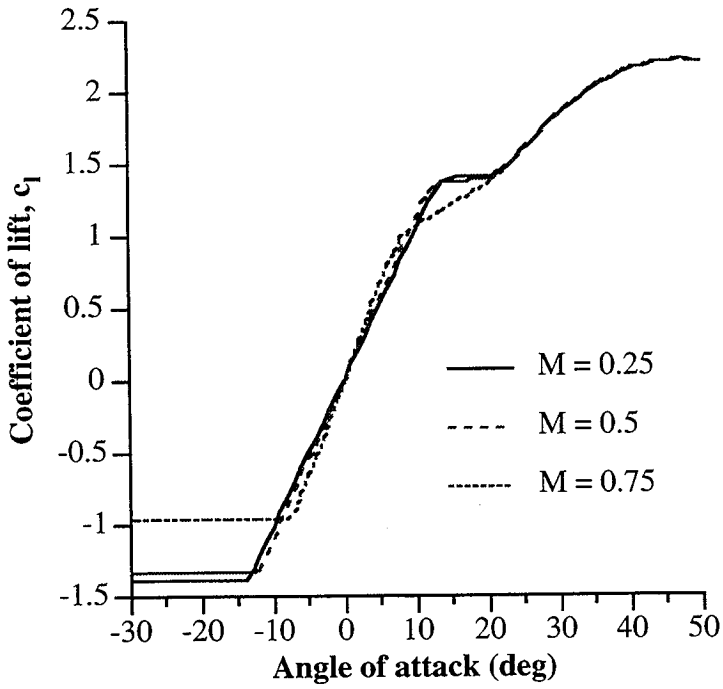

Fig. 5.1 Sectional lift coefficient distribution; Advanced Technology Blade.

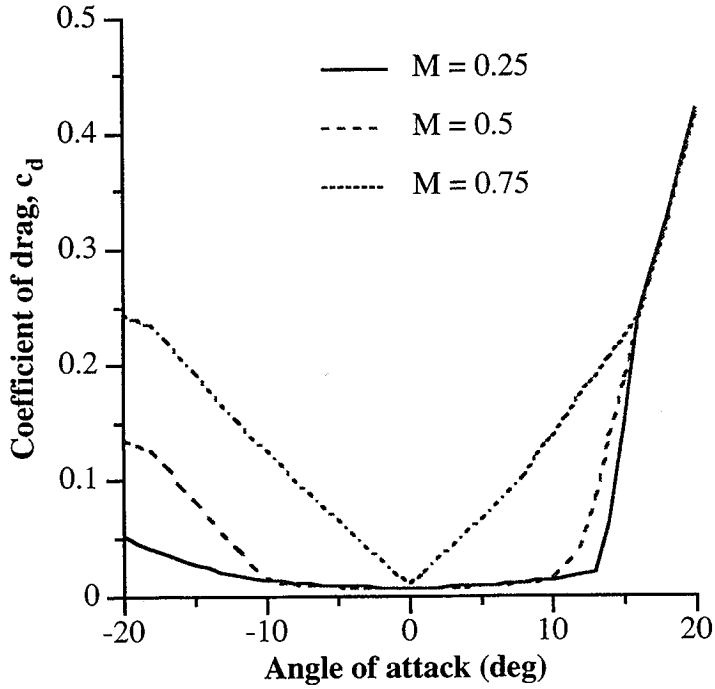

Fig. 5.2 Sectional drag coefficient distribution; Advanced Technology Blade.

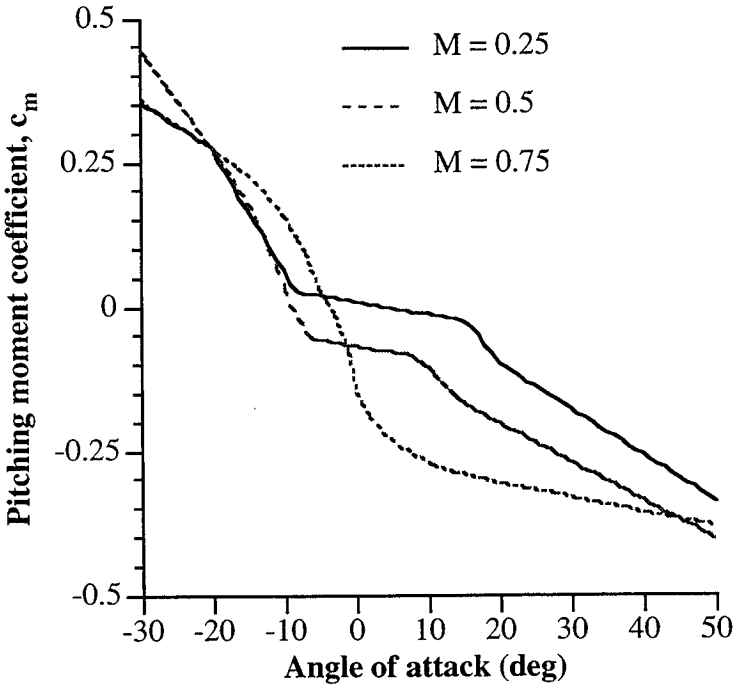

Fig. 5.3 Sectional pitching moment coefficient distribution; Advanced Technology Blade.

The subscripts (1) and (2) in Eqns. 5.1 - 5.4 correspond to the momentum and force equations, respectively, for thrust and torque. This system of equations is then used to solve for the inflow and swirl velocities by equating the thrust and torque as follows

$$dT_1 = dT_2 , \tag{5.5}$$

$$dQ_1 = dQ_2 . \tag{5.6}$$

The total inflow angle of the blade section (Λ, in Eqns. 5.2 and 5.4) is defined as

$$\Lambda = \Lambda_a + \Lambda_s , \tag{5.7}$$

where Λ_a is the angle of the aerodynamic inflow and Λ_s is the additional inflow angle which arises due to the inclusion of blade dynamic effects (Fig. 5.4). The effective inflow angle due to aerodynamics (Λ_a) is defined as

$$\Lambda_a = \tan^{-1}\left(\frac{V_\infty + \upsilon_i}{\Omega r - u_T}\right), \tag{5.8}$$

where V_∞ is the forward velocity of the aircraft and Ω is the rotational speed of the rotor.

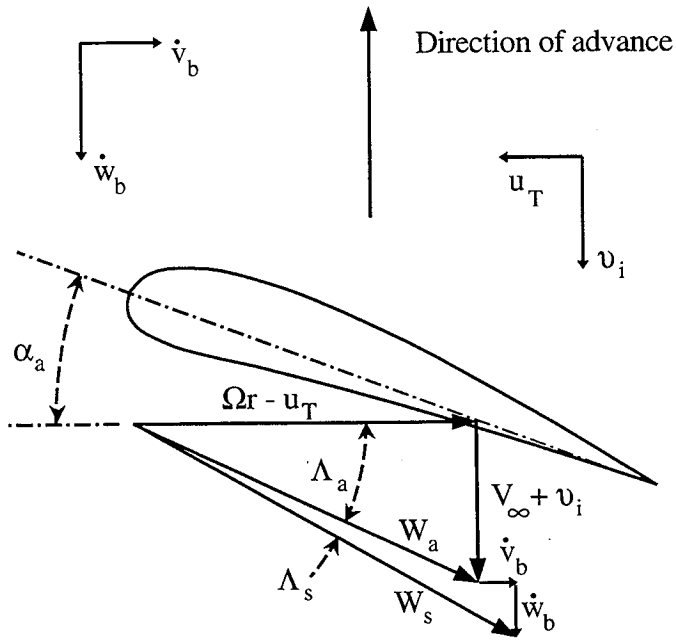

Fig. 5.4 Blade element inflow definitions.

To define the effective structural inflow angle, Λ_s, it is first necessary to translate the blade dynamics from the global, untwisted coordinate system to a coordinate system which is parallel to the effective aerodynamic inflow angle (Fig. 5.5). This is mathematically stated as follows.

$$\begin{aligned} \dot{\tilde{v}}_b &= \dot{v}_b \cos\Lambda_a + \dot{w}_b \sin\Lambda_a \\ \dot{\tilde{w}}_b &= -\dot{v}_b \sin\Lambda_a + \dot{w}_b \cos\Lambda_a \end{aligned} \tag{5.9}$$

where $\dot{\tilde{v}}_b$ is the dynamic velocity parallel to the aerodynamic inflow angle and $\dot{\tilde{w}}_b$ is the velocity perpendicular to the inflow angle. The quantities, $\dot{v}_b$ and $\dot{w}_b$, represent the dynamic effects perpendicular and parallel to the free stream velocity, respectively. These transverse velocities are defined as

$$\begin{aligned} \dot{v}_b &= \dot{\tilde{v}}\cos(\alpha_a) - \dot{\tilde{w}}\sin(\alpha_a) \\ \dot{w}_b &= \dot{\tilde{v}}\sin(\alpha_a) + \dot{\tilde{w}}\sin(\alpha_a) - \dot{\phi}Y'_{ac} \end{aligned} \tag{5.10}$$

where Y'_{ac} is the offset between the aerodynamic center of the blade and the axis of twist.

The physical angle of attack of the blade is denoted α_a and the cross-sectional velocities in the global, twisted coordinate system are $\dot{\tilde{v}}$ and $\dot{\tilde{w}}$ (Fig. 5.5). The effective aerodynamic inflow angle is defined as follows.

$$\begin{aligned} \sin\Lambda_a &= \frac{V_\infty + \upsilon_i}{W} \\ \cos\Lambda_a &= \frac{\Omega r - u_T}{W} \end{aligned} \tag{5.11}$$

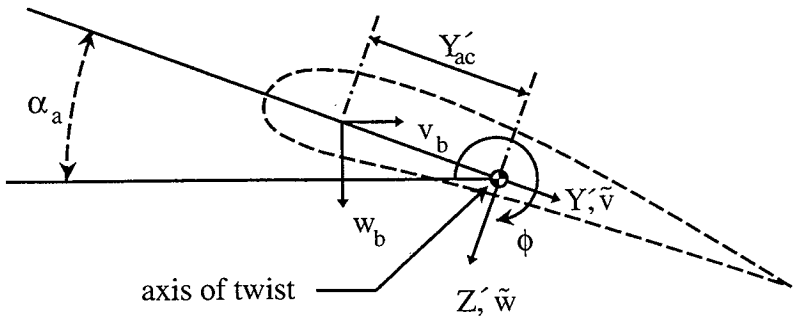

Fig. 5.5 Coordinate systems in blade cross section.

where W is the total resultant velocity. Under the assumption that the velocities due to airflow are much greater than those due to blade dynamics, the total resultant velocity is written as

$$W \cong W_a \cong W_s \tag{5.12}$$

The effective structural inflow angle is then written as follows.

$$\Lambda_s = \frac{\dot{\tilde{w}}_b}{W} \tag{5.13}$$

Using Eqns. 5.7 - 5.13, the total inflow angle is expressed as

$$\Lambda = \Lambda_a - \frac{\dot{v}_b(V_\infty + \upsilon_i)}{W^2} + \frac{\dot{w}_b(\Omega r - u_T)}{W^2}. \tag{5.14}$$

The effective angle of attack (α) for the blade cross section is defined as follows

$$\alpha = \alpha_a + \phi - \Lambda, \tag{5.15}$$

where α_a is the physical angle of attack of the blade and ϕ is the elastic twist due blade deformations. Using Eqn. 5.14, the effective angle of attack is rewritten as

$$\alpha = \underbrace{\alpha_a - \Lambda_a}_{\text{Aerodynamics}} + \underbrace{\phi + \frac{\dot{v}_b(V_\infty + \upsilon_i)}{W^2} - \frac{\dot{w}_b(\Omega r - u_T)}{W^2}}_{\text{Elastic deformations}}. \tag{5.16}$$

In the above equation, the first two terms correspond to the purely aerodynamic effects and the last three terms represent contributions due to blade elastic deformations. Note that the steady state angle (α_{ss}) is written as

$$\alpha_{ss} = \alpha_a - \Lambda_a + \phi. \tag{5.17}$$

5.2 Energy Formulation

To evaluate the external work due to the aerodynamic loading it is first necessary to write the equations for lift, drag and pitching moment, per unit area, as follows.

$$l = \frac{1}{2}\rho W^2 c_{l_\alpha}\left(\alpha_a - \Lambda_a + \phi + \frac{\dot{v}_b(V_\infty + v_i)}{W^2} - \frac{\dot{w}_b(\Omega r - u_T)}{W^2}\right) \tag{5.18a}$$

$$d = \frac{1}{2}\rho W^2 c_{d_\alpha}\left(\alpha_a - \Lambda_a + \phi + \frac{\dot{v}_b(V_\infty + v_i)}{W^2} - \frac{\dot{w}_b(\Omega r - u_T)}{W^2}\right) \tag{5.18b}$$

$$m = \frac{1}{2}\rho W^2 c\, c_{m_\alpha}\left(\alpha_a - \Lambda_a + \phi + \frac{\dot{v}_b(V_\infty + v_i)}{W^2} - \frac{\dot{w}_b(\Omega r - u_T)}{W^2}\right) \tag{5.18c}$$

The coefficients (c_{l_α}, $c_{d\alpha}$ and $c_{m\alpha}$) are related to the derivatives of the lift, drag and moment coefficients (c_l, c_d, c_m), respectively as follows.

$$c_{l_\alpha} = c_{l_o} + \frac{\partial c_l}{\partial \alpha} \tag{5.19a}$$

$$c_{d_\alpha} = c_{d_o} + \frac{\partial c_d}{\partial \alpha} \tag{5.19b}$$

$$c_{m_\alpha} = c_{m_o} + \frac{\partial c_m}{\partial \alpha} \tag{5.19c}$$

The external work done by the aerodynamic loads is then written as

$$W_e = \int_S (-l\, w + d\, v + m\, \phi)\, dS \tag{5.20}$$

where S is the blade surface area and w, v and ϕ are the global, untwisted displacements. From Eqns. 5.18, it must be noted that the aerodynamic forces and moments can be separated into a steady aerodynamic term (α_a - Λ_a), a steady term dependent on the elastic deflection (ϕ) and a term associated with blade dynamics ($\dot{v}_b$ and $\dot{w}_b$). Define the following parameters

$$L_\phi = -\frac{1}{2}\rho W^2 (c_l \cos\alpha_a + c_d \sin\alpha_a), \tag{5.21a}$$

$$D_\phi = \frac{1}{2}\rho W^2 (-c_l \sin\alpha_a + c_d \cos\alpha_a), \tag{5.21a}$$

$$M_\phi = \frac{1}{2}\rho W^2\, c\, c_m - L_\phi Y'_{ac}, \tag{5.21a}$$

and

$$L_{\phi_\alpha} = -\frac{1}{2}\rho W^2\left(c_{l_\alpha}\cos\alpha_a + c_{d_\alpha}\sin\alpha_a\right), \tag{5.22a}$$

$$D_{\phi_\alpha} = \frac{1}{2}\rho W^2\left(-c_{l_\alpha}\sin\alpha_a + c_{d_\alpha}\cos\alpha_a\right), \tag{5.22a}$$

$$M_{\phi_\alpha} = \frac{1}{2}\rho W^2\, c\, c_{m_\alpha} - L_{\phi_\alpha} Y'_{ac}. \tag{5.22a}$$

Also, it must be noted that at the outer surfaces of the beam ($\zeta_i = +h/2$) the rotation about the χ-axis is defined as

$$\phi = \frac{1}{2}\left(\frac{\partial\tilde{w}}{\partial\eta} - \frac{\partial\tilde{v}}{\partial\zeta}\right)\Bigg|_{\zeta=h/2} = \frac{\partial w_o}{\partial\eta} = \frac{\partial\tilde{w}}{\partial\eta}. \tag{5.23}$$

Using Eqns. 5.10 and 5.18, the external work due to steady aerodynamic terms (W_{e_a}) and that due to static deflections (W_{e_s}) can now be expressed as follows.

$$W_{e_a} = \int_S (\alpha_a - \Lambda_a)\left[L_\phi\tilde{w} + D_\phi\tilde{v} + M_\phi\frac{\partial\tilde{w}}{\partial\eta}\right]dS, \tag{5.24}$$

$$W_{e_s} = \int_S\left[L_{\phi_\alpha}\frac{\partial\tilde{w}}{\partial\eta}\tilde{w} + D_{\phi_\alpha}\frac{\partial\tilde{w}}{\partial\eta}\tilde{v} + M_{\phi_\alpha}\frac{\partial\tilde{w}}{\partial\eta}\frac{\partial\tilde{w}}{\partial\eta}\right]dS. \tag{5.25}$$

The external work due to the dynamics loads (W_{e_d}) is written using Eqns. 5.10, 5.18, 5.20 and 5.23 as follows.

$$\begin{aligned} W_{e_d} = \frac{1}{2}\int_S \rho\Bigg[&\left\{c_{l_\alpha}\left(\tilde{v}\sin\alpha + \tilde{w}\cos\alpha\right) + c_{d_\alpha}\left(\tilde{v}\cos\alpha - \tilde{w}\sin\alpha\right) + c\, c_{m_\alpha}\frac{\partial\tilde{w}}{\partial\eta}\right\} \\ &\times\left\{\left(\dot{\tilde{v}}\cos\alpha - \dot{\tilde{w}}\sin\alpha\right)\left(V_\infty + \upsilon_i\right) - \left(\dot{\tilde{v}}\sin\alpha + \dot{\tilde{w}}\cos\alpha - \frac{\partial\dot{\tilde{w}}}{\partial\eta}\right)\left(\Omega r - u_T\right)\right\}\Bigg] dS \end{aligned} \tag{5.26}$$

Using the variational principles, the external work functionals are written as follows.

$$\delta W_{e_a} = \int_S (\alpha_a - \Lambda_a)\left[\left\{L_\phi - \frac{\partial}{\partial\eta}\left(M_\phi\right)\right\}\delta\tilde{w} + D_\phi\delta\tilde{v}\right]dS, \tag{5.27}$$

$$\delta W_{e_s} = \int_S \left[D_{\phi\alpha} \frac{\partial \tilde{w}}{\partial \eta} \delta \tilde{v} - \left\{ D_{\phi\alpha} \frac{\partial \tilde{v}}{\partial \eta} + 2\, M_{\phi\alpha} \frac{\partial^2 \tilde{w}}{\partial \eta^2} \right\} \delta \tilde{w} \right] dS, \tag{5.28}$$

$$\delta W_{ed} = \int_S \left[\dot{\tilde{v}} \quad \dot{\tilde{v}}_{,\eta} \quad \dot{\tilde{w}} \quad \dot{\tilde{w}}_{,\eta} \right] \begin{bmatrix} 0 & a_w \\ 0 & b_w \\ -a_w & 0 \\ b_w & c_w \end{bmatrix} \begin{Bmatrix} \delta \tilde{v} \\ \delta \tilde{w} \end{Bmatrix} dS \tag{5.29}$$

where

$$a_w = \frac{1}{2} \rho \left[c_{l_\alpha} (V_\infty + v_i) + c_{d_\alpha} (\Omega r - u_T) \right] \tag{5.30a}$$

$$\begin{aligned} b_w &= \frac{1}{2} \rho\, Y'_{ac} \left[c_{l_\alpha} \sin\alpha_b + c_{d_\alpha} \cos\alpha_b \right] (\Omega r - u_T) \\ &+ \frac{1}{2} \rho\, c\, c_{m_\alpha} \left[(V_\infty + v_i) \cos\alpha_b - (\Omega r - u_T) \sin\alpha_b \right] \end{aligned} \tag{5.30b}$$

$$\begin{aligned} c_w &= \rho\, Y'_{ac} \left[c_{l_\alpha} \cos\alpha_b - c_{d_\alpha} \sin\alpha_b \right] (\Omega r - u_T) \\ &- \rho\, c\, c_{m_\alpha} \left[(V_\infty + v_i) \sin\alpha_b + (\Omega r - u_T) \cos\alpha_b \right] \end{aligned} \tag{5.30c}$$

5.3 Solution Procedure

Equations 5.27 - 5.29 indicate that the external work from the aerodynamic loads will yield three separate equations. The first terms are associated with a steady state forcing vector independent of the displacements, F_{aero} (Eqn. 5.27). There are forcing terms that are dependent on the displacements (Eqn. 5.28) which will yield a matrix analogous to the stiffness matrix (K_{aero}). Finally, there are forcing terms that are dependent on the velocity of the displacements (Eqn. 5.29) yielding a damping matrix (C_{aero}).

Denoting the following matrices

$$\tilde{\mathbf{N}} = \frac{\partial [\tilde{v} \quad \tilde{w}]^T}{\partial \mathbf{q}}, \tag{5.31}$$

and

$$\tilde{\mathbf{N}}_\eta = \frac{\partial\left[\tilde{v} \;\; \tilde{v}_{,\eta} \;\; \tilde{w} \;\; \tilde{w}_{,\eta}\right]^T}{\partial \mathbf{q}}, \tag{5.32}$$

where $\mathbf{q}$ is the degree of freedom vector defined in Chapter 3, the quantities associated with the external work due to aerodynamic loads are formulated as follows.

$$\mathbf{F}_{aero} = \sum_{i=1}^{N}\left[\int_S \tilde{\mathbf{N}}^T \tilde{\mathbf{f}}\, dS\right], \tag{5.33}$$

$$\mathbf{K}_{aero} = \sum_{i=1}^{N}\left[\int_S \tilde{\mathbf{N}}^T \mathbf{Q}_1\, dS\right], \tag{5.34}$$

and

$$\mathbf{C}_{aero} = \sum_{i=1}^{N}\left[\int_S \tilde{\mathbf{N}}^T\begin{bmatrix} 0 & 0 & -a_w & b_w \\ a_w & b_w & 0 & c_w \end{bmatrix}\tilde{\mathbf{N}}_\eta\, dS\right], \tag{5.35}$$

where

$$\tilde{\mathbf{f}}^T = (\alpha_a - \Lambda_a)\left[D_\phi \;\; \left\{L_\phi - \frac{\partial}{\partial\eta}(M_\phi)\right\}\right], \tag{5.36}$$

$$\mathbf{Q}_1 = \frac{\partial\left[D_\phi \dfrac{\partial\tilde{w}}{\partial\eta} \;\; -\left\{D_\phi \dfrac{\partial\tilde{v}}{\partial\eta} + 2\,M_\phi \dfrac{\partial^2\tilde{w}}{\partial\eta^2}\right\}\right]}{\partial \mathbf{q}}. \tag{5.37}$$

The complete aerodynamic/dynamic/structural equations of motion for the coupled system are now written in the following matrix form

$$\mathbf{M}\,\ddot{\mathbf{q}} + \mathbf{C}\,\dot{\mathbf{q}} + \mathbf{K}\,\mathbf{q} = \mathbf{F} + \left(\mathbf{F}_{aero} + \mathbf{K}_{aero}\,\mathbf{q} + \mathbf{C}_{aero}\,\dot{\mathbf{q}}\right), \tag{5.38}$$

where the quantities within the parentheses correspond to the external work due to aerodynamic loading and the remaining terms are associated with the structural modeling of the beam (Eqn. 3.72)

5.4 Aeroelastic Stability

To investigate the aeroelastic stability of the rotor, the natural frequencies of the complete coupled equations of motion must be determined. By rearranging the terms in Eqn. 5.38, the equation may be rewritten as follows.

$$\mathbf{M}\,\ddot{\mathbf{q}} + \left(\mathbf{C} - \mathbf{C}_{\text{aero}}\right)\dot{\mathbf{q}} + \left(\mathbf{K} - \mathbf{K}_{\text{aero}}\right)\mathbf{q} = \mathbf{F} + \mathbf{F}_{\text{aero}} \tag{5.39}$$

The homogeneous portion of Eqn. 5.39 can be rewritten as

$$\tilde{\mathbf{M}}\,\ddot{\mathbf{q}} + \tilde{\mathbf{C}}\,\dot{\mathbf{q}} + \tilde{\mathbf{K}}\,\mathbf{q} = \mathbf{0}, \tag{5.40}$$

where

$$\tilde{\mathbf{M}} = \mathbf{M}, \tag{5.41}$$

$$\tilde{\mathbf{C}} = \left(\mathbf{C} - \mathbf{C}_{\text{aero}}\right), \tag{5.42}$$

$$\tilde{\mathbf{K}} = \left(\mathbf{K} - \mathbf{K}_{\text{aero}}\right). \tag{5.43}$$

It is possible to rewrite Eqn. 5.40, which is a second order equation, as a first order equation by making the following transformation

$$\{\delta\} = \begin{Bmatrix} \mathbf{q} \\ \dot{\mathbf{q}} \end{Bmatrix}. \tag{5.44}$$

Now Eqn. 5.40 is written as

$$\left\{\dot{\delta}\right\} = \mathbf{A}\,\{\delta\} \tag{5.45}$$

where

$$\mathbf{A} = \begin{bmatrix} 0 & \mathbf{I} \\ -\tilde{\mathbf{M}}^{-1}\tilde{\mathbf{K}} & -\tilde{\mathbf{M}}^{-1}\tilde{\mathbf{C}} \end{bmatrix} \tag{5.46}$$

The characteristic roots of Eqn. 5.40 are now determined by solving for the eigenvalues of **A**. It must be noted that the matrix **A** is neither positive definite, nor symmetric in

general and as a result, the eigenvalues are complex. If any of the roots of **A** have a positive real component, the system will be unstable at the given velocity.

5.5 Correlation

The adequacy of this aerodynamic representation is demonstrated in Figs. 5.6 and 5.7. This relatively simplistic formulation is shown to correlate very well with measured axial flow performance of the XV-15 rotor system in both hover and in airplane mode from tests conducted at the Outdoor Aerodynamic Research Facility (O.A.R.F.) and from flight test data obtained at NASA Ames Research Center [113,114]. This representation of the rotor, which is representative of the original design point of the XV-15 tiltrotor, is used as the baseline, or reference, rotor in this study. Further, as shown in Ref. 13 the results obtained using this approach are comparable with those obtained by Dadone et al. [5] in which a more comprehensive Euler based analysis technique was used. Therefore, despite the relative simplicity, the present approach proves to be quite adequate for modeling prop-rotor blade aerodynamics.

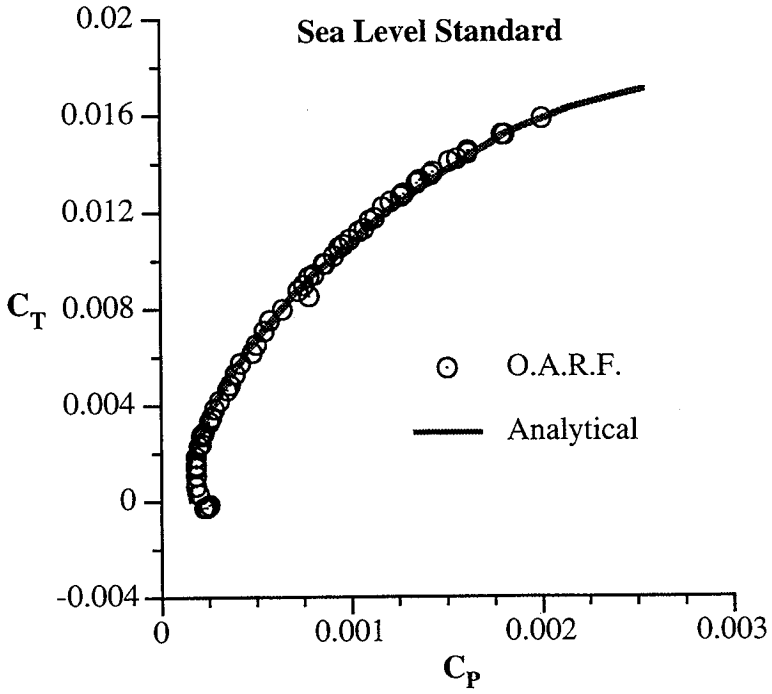

Fig. 5.6 Comparison of analytical and experimental thrust in hover.

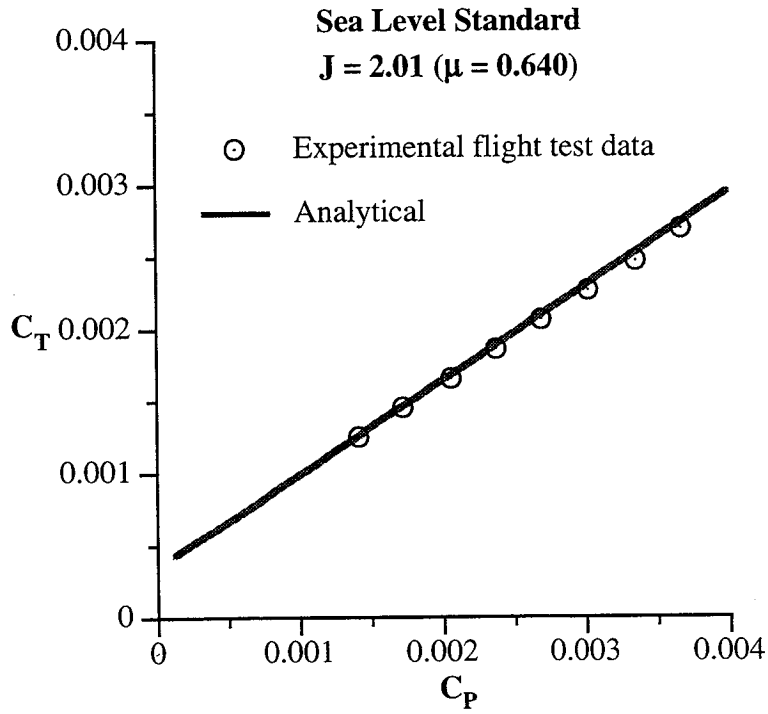

Fig. 5.7 Cruise propulsive efficiency correlation.

6. Optimization Problem

The structural, dynamic, aerodynamic and aeroelastic analysis procedures developed are now integrated to develop a multidisciplinary optimization procedure for investigating the design trade-offs of high speed prop-rotors. The reference aircraft, used as a baseline design in the optimization procedure, is a mathematical representation of the XV-15 tilting proprotor aircraft. The rotor is a three-bladed, gimballed rotor with a 25 foot diameter [113,114]. A multipoint optimization procedure is developed and design criteria associated with two flight conditions are addresses simultaneously. The first flight condition corresponds to hover at sea level and the second flight condition represents high speed cruise at an altitude of 25,000 feet and a forward speed of 400 knots. This altitude is typical for tiltrotors operating in high speed cruise.

6.1 Rotor Geometric Modeling

The rotor planform characteristics are defined as follows. The chord (c) and pre-twist angle (θ) are defined to have the following cubic spanwise distributions

$$c(\bar{x}) = c_0 + c_1\bar{x} + c_2\bar{x}^2 + c_3\bar{x}^3, \tag{6.1}$$

$$\theta(\bar{x}) = \theta_1(\bar{x} - 0.75) + \theta_2(\bar{x} - 0.75)^2 + \theta_3(\bar{x} - 0.75)^3, \tag{6.2}$$

where $\bar{x}$ is the nondimensional radial location ($\bar{x}$ = x/R, R = blade radius). These cubic distributions are selected to give the optimizer sufficient flexibility since the parameters which define these distributions are used as design variables. The offset in the twist distribution ($\bar{x}$ - 0.75) is used to ensure zero twist at 75 percent span [117]. The blade thickness-to-chord ratio (t/c) is defined to have a quadratic spanwise distribution to ensure a monotonic decrease in the thickness from root to tip. This distribution is defined as follows

$$t/c(\bar{x}) = t_0 + t_1\bar{x} + t_2\bar{x}^2. \tag{6.3}$$

Similarly, the blade is defined to have a quadratic lifting line offset as follows

$$y_{ac}(\bar{x}) = \frac{1}{2} a_o \bar{x}^2. \tag{6.4}$$

The above distribution is chosen to ensure zero offset at the root as well as zero sweep. The blade sweep ($\hat{\Lambda}$) is defined as follows.

$$\hat{\Lambda} = \tan^{-1}\left(\frac{dy_{ac}}{dx}\right) \tag{6.5}$$

or

$$\hat{\Lambda} = \tan^{-1}(a_o \bar{x}) \tag{6.6}$$

6.2 Structural Model

The box beam dimensions are assumed to be fixed percentages of the chord length and airfoil thickness as seen in Fig. 6.1. For the present study, the axis of twist (and rotation) is assumed to lie at the centroid of the beam. Further, the beam centroid is assumed to be at the 50 percent chord location.

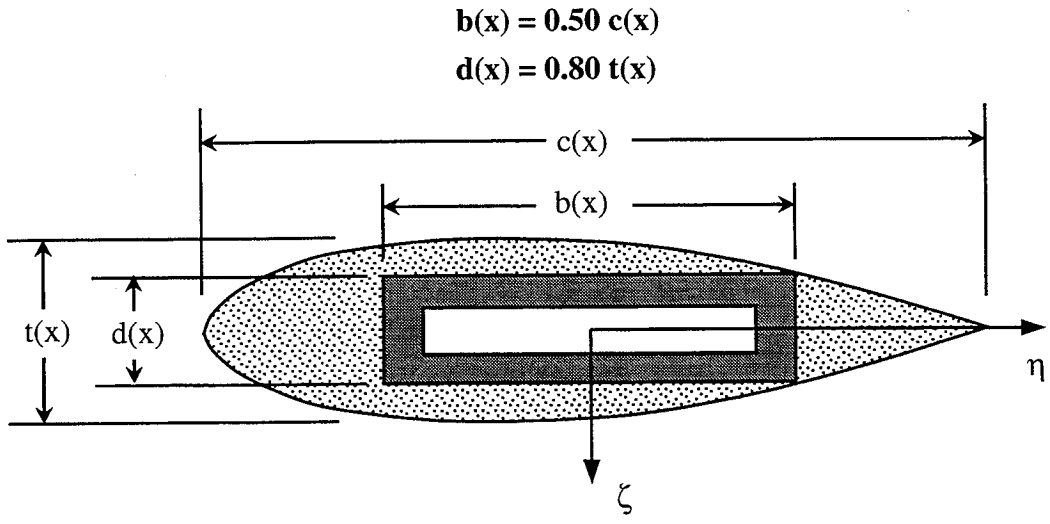

Fig. 6.1 Blade cross section and beam dimensions.

The two horizontal walls of the box beam are assumed to have identical composite lay-ups. A stacking sequence of $\left[\left\{(\beta_1)_3/(\beta_2)_3\right\}_3\right]_s$ is used during the optimization. Similarly, the two vertical walls are assumed to have the same lay-ups defined as $\left[\left\{(\beta_3)_3/(\beta_4)_3\right\}_3\right]_s$. A total number of 36 plies is used to ensure that the blade is stiff enough to sustain the large aerodynamic loads generated by the rotor. The angle ply stacking sequence is selected to investigate the effects of composite ply angles on the overall aerodynamic/structural/aeroelastic performance of the rotor.

6.3 Objective Functions and Constraints

The optimization problem addresses the simultaneous maximization of both the hover figure of merit (FM) and the propulsive efficiency in high speed cruise (η_c). These quantities are defined as follows.

$$FM = \frac{P_{ideal}}{P} \tag{6.7}$$

$$\eta_c = \frac{TV_\infty}{P} \tag{6.8}$$

The following constraints are imposed to ensure efficient structural and aerodynamic performance. To maintain blade aeroelastic stability, constraints are imposed on the real part of the stability roots determined from Eqn. 5.39

$$\lambda_k \geq -\varpi \qquad k = 1, 2, \cdots, NAERO \tag{6.9}$$

where ϖ is the minimum allowable damping, defined to be a small positive number and NAERO is the number of modes considered.

To prevent material failure, constraints are imposed on the individual ply stresses based on the Tsai-Wu failure criterion [118]. This criterion assumes that to avoid material failure the following equations representing a failure surface in the stress-space must be satisfied.

$$F_i\sigma_i + F_{ij}\sigma_i\sigma_j \leq 1 \qquad (i, j = 1, 2, \cdots, 6) \tag{6.10}$$

where σ_i represents the stresses in the coordinate system defined by the material axes (see Fig. 6.2). The quantities F_i and F_{ij} are related to tensile and compressive yield strengths of the material and are defined as follows.

$$F_i = \begin{Bmatrix} \frac{1}{X_T} - \frac{1}{X_C} \\ \frac{1}{Y_T} - \frac{1}{Y_C} \\ \frac{1}{Y_T} - \frac{1}{Y_C} \\ 0 \\ 0 \\ 0 \end{Bmatrix} \tag{6.11}$$

$$F_{ij} = \begin{bmatrix} \frac{1}{X_T X_C} & F_{12} & F_{12} & 0 & 0 & 0 \\ & \frac{1}{Y_T Y_C} & F_{23} & 0 & 0 & 0 \\ & & \frac{1}{Y_T Y_C} & 0 & 0 & 0 \\ & & & 2\left(\frac{1}{Y_T Y_C} - F_{23}\right) & 0 & 0 \\ & \text{sym.} & & & \frac{1}{S^2} & 0 \\ & & & & & \frac{1}{S^2} \end{bmatrix} \tag{6.12}$$

where the quantities X, Y are the yield strengths in both compression (subscript 'C') and tension (subscript 'T') and S is the corresponding shear strength. The quantities F_{12} and F_{23} are defined as

$$F_{12} = -\frac{1}{2}\sqrt{F_{11}F_{22}} \tag{6.13}$$

$$F_{23} = -\frac{1}{2}F_{22} \tag{6.14}$$

This reduces the total number of constraints as constraints on the individual stress (σ_i) at each ply level are avoided.

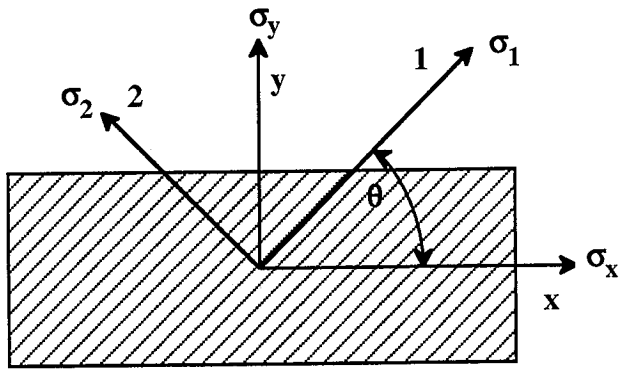

Fig. 6.2 Composite lamina material axes.

To maintain rotor thrust at acceptable values during optimization, equality constraints are imposed on the thrust in hover and in cruise. These constraints assume the following form.

$$T_h = T_{h_{ref}} \tag{6.14}$$

$$T_c = T_{c_{ref}} \tag{6.15}$$

6.4 Design Variables

The design variables that are used during the optimization include the coefficients which define the spanwise chord and twist distributions (c_0 - c_3 and θ_1 - θ_3, respectively), the thickness-to-chord ratio (t_o - t_2) and the blade sweep (a_o). The variables which define the composite lay-up in the individual walls (β_1 - β_4) are also used as design variables. It must be noted that to ensure realistic blade chord and wing thickness distributions (i.e., positive throughout the span), it is necessary to further impose additional geometric constraints on these distributions. The minimum allowable nondimensional chord value (c/R) is constrained to be 0.02 and the minimum allowable thickness (t) is constrained to be 0.75 in. Although, the minimum allowable chord values are far too small at the root, due to constraints on the stresses these chord distribution is never near critical values except at locations near the tip.

7. Optimization Procedure

The optimization problem addressed in this research is associated with multidisciplinary coupling and involves multiple design objectives and constraints. The Kreisselmeier-Steinhauser (K-S) function technique [119] is used to efficiently integrate all of the objective functions and constraints into a single envelop function. The problem is thus reduced to an unconstrained optimization problem. The Broyden-Fletcher-Goldfarb-Shanno (BFGS) algorithm [120] is used to solve the unconstrained nonlinear problem (NLP). A hybrid approximate analysis technique based on a two-point exponential expansion technique [121] is coupled with the optimization procedure to reduce the computational effort. The following sections contain details of the optimization procedure.

7.1 Kreisselmeier-Steinhauser (K-S) Function Approach

Since the optimization problem involves more than one design objective, the objective function formulation is more complicated. In most of the existing work, the individual objective functions are combined using weight factors in a linear fashion [43,44,122]. Such methods are judgmental as the answer depends upon the weight factors which are often hard to justify. Therefore, the problem is formulated using the Kreisselmeier-Steinhauser (K-S) function approach [119]. Using this function the multiple objective functions and constraints are transformed into a single envelope function which is then minimized using unconstrained optimization techniques. The K-S function has been found to perform extremely well by McCarthy et al. in a variety of rotary wing optimization problems [9,12-16].

The first step in the K-S function approach involves the transformation of the original objective functions into reduced objective functions. If the individual objective functions are to be minimized, these reduced objective functions assume the following form

$$F_k^*(\Phi) = \frac{F_k(\Phi)}{F_{k_o}} - 1.0 - g_{max} \leq 0 . \qquad k = 1, \cdots, NOBJ_{min} \qquad (7.1a)$$

When the individual objective functions are to be maximized, the reduced objective functions are as follows

$$F_k^*(\Phi) = 1.0 - \frac{F_k(\Phi)}{F_{k_o}} - g_{max} \leq 0, \qquad k = 1, \cdots, NOBJ_{max} \tag{7.1b}$$

where F_{k_o} represents the value of the original objective function F_k calculated at the beginning of each cycle and Φ is the design variable vector. The quantity g_{max} is the value of the largest constraint corresponding to the original constraint vector, $\mathbf{g}_j(\Phi)$ ($j = 1, 2, \cdots, NC$) and is held constant during each cycle. These reduced objective functions are analogous to constraints, therefore a new constraint vector $\mathbf{f}_m(\Phi)$ ($m = 1, 2, \cdots, M$ where $M = NC + NOBJ$) is introduced which includes the original constraints and the constraints introduced through the reduced objective functions (Eqns. 7.1). The design variable vector in this formulation remains unchanged. The new objective function to be minimized is defined using the K-S function as follows

$$F_{KS}(\Phi) = f_{max} + \frac{1}{\hat{\rho}} \log_e \sum_{m=1}^{M} e^{\hat{\rho}(f_m(\Phi) - f_{max})}, \tag{7.2}$$

where f_{max} is the largest constraint corresponding to the new constraint vector $\mathbf{f}_m(\Phi)$ and in general is not equal to g_{max}. The objective function $F_{KS}(\Phi)$, which represents an envelope function representing the original objective functions and constraints, can now be minimized using any unconstrained optimization technique.

The optimization algorithm, based upon this technique, can be explained as follows. Initially in an infeasible design space, where the original constraints are violated, the constraints due to the reduced objective functions (Eqns. 7.1) are satisfied, i.e. g_{max} is negative. Once the original constraints are satisfied, the constraints due to the reduced objective functions become violated. When this happens, the optimizer attempts to satisfy these constraints and in doing so, minimizes (or maximizes) the original objective functions (F_k). The multiplier $\hat{\rho}$ in Eqn. 7.2 is analogous to a draw-down factor where $\hat{\rho}$ controls

the distance from the surface of the K-S objective function to the surface of the maximum constraint function. When $\hat{\rho}$ is large, the K-S function closely follows the surface of the largest constraint function and when $\hat{\rho}$ is small, the K-S function includes contributions from all violated constraints. Additional details can be found in Refs. 93, 94, 97-101.

The K-S function formulation is illustrated for a problem where a single objective function is to be maximized subject to two constraints using one design variable (Figs. 7.1 and 7.2). An initial design point of X = 7 is used in the example. At this point, both constraints are satisfied and g_{max} is therefore negative. As a result, the reduced objective function is positive and the constraint introduced through Eqn. 7.1b is violated (Fig. 7.1). The three constraints of the problem introduced by the original constraints and the reduced objective function are shown in Fig. 7.2 along with the associated K-S function for three different values of $\hat{\rho}$. As seen from the figure, for a value of $\hat{\rho}$ =1, the K-S function represents a more composite envelope function which includes contributions from all three constraints. This is especially evident at locations where the values of two or more constraints are very similar. For the larger values of $\hat{\rho}$ = 3 and $\hat{\rho}$ = 5, the K-S function envelope more closely represents only the largest constraint even at locations where the constraints are similar in value. This simple example demonstrates how larger values of $\hat{\rho}$ "draw down" the K-S function closer to the value of the largest constraint.

The K-S function (Fig. 7.2) is minimized using standard nonlinear, unconstrained optimization techniques. Once a local minima is reached, a new cycle begins with the calculation of a new value of g_{max} and the reformulation of the reduced objective functions and the K-S function. The process is repeated until either the original objective functions or the design variable vector converges. Note that it is permissible to allow the value of $\hat{\rho}$ to change from cycle to cycle. This is typically done is a monotonically increasing manner so that as the optimization proceeds, the K-S function more closely represents only the largest constraint (or the reduced objective function).

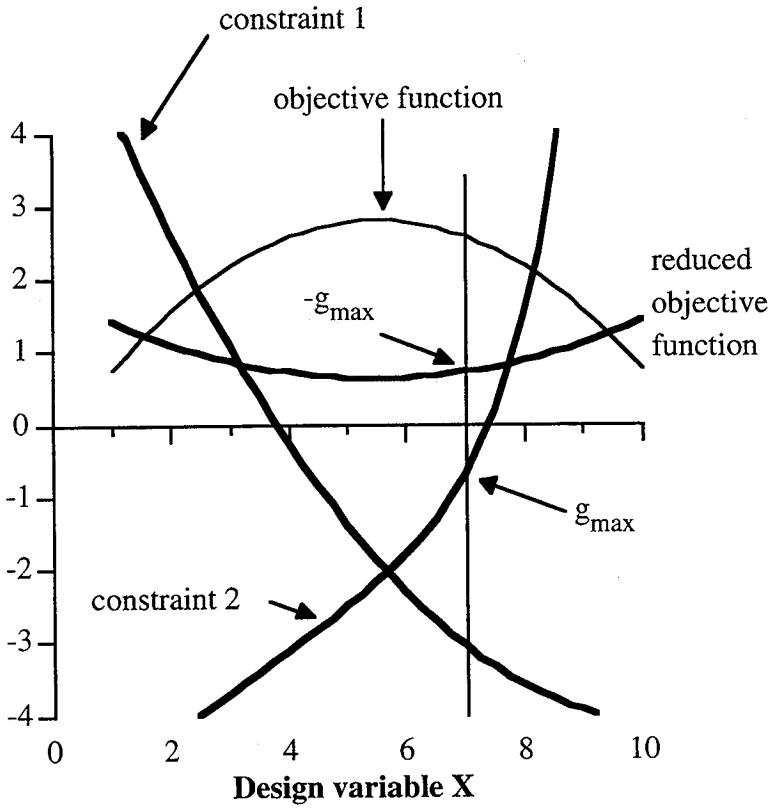

Fig. 7.1 K-S function formulation example.

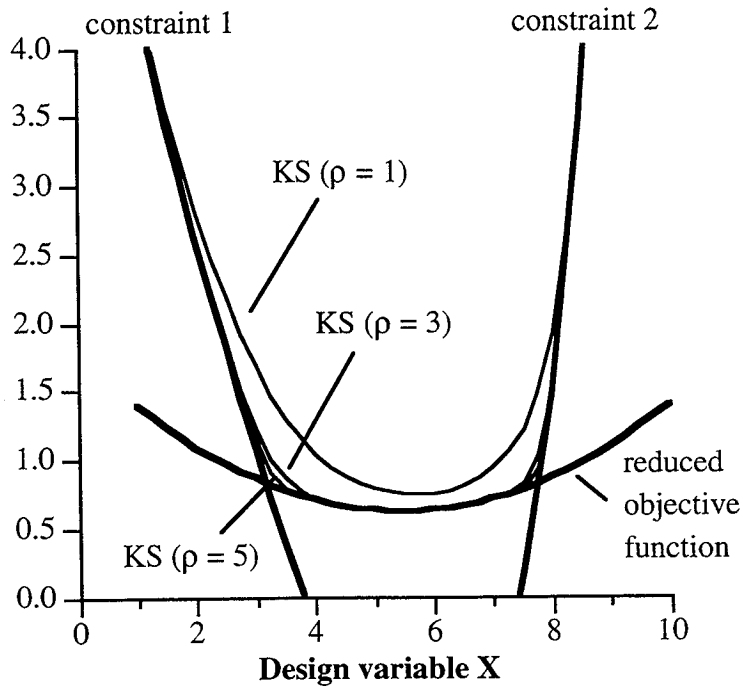

Fig. 7.2 K-S function envelope.

7.2 Approximate Analysis

The two-point exponential approximation technique [121], which was found to perform well in other nonlinear optimization problems [8-12, 14-16], is used for the approximation of the objective functions and the constraints. This technique derives its name from the fact that the exponent used in the expansion is based upon gradient information from the previous and current design cycles. The technique is described below.

$$\hat{F}_k(\Phi) = F_k(\Phi_o) + \sum_{n=1}^{NDV}\left[\left(\frac{\Phi_n}{\Phi_{o_n}}\right)^{p_n} - 1.0\right]\frac{\Phi_{o_n}}{p_n}\frac{\partial F_k(\Phi_o)}{\partial \Phi_n} \tag{7.3}$$

where $\hat{F}_k(\Phi)$ is the approximation of the original objective function $F_k(\Phi_o)$. The approximate values for the constraints, $\hat{g}_j(\Phi)$, are similarly calculated. The exponent, p_n, is defined below

$$p_n = \frac{\log_e\left\{\frac{\partial F(\Phi_1)}{\partial \Phi_n}\right\} - \log_e\left\{\frac{\partial F(\Phi_o)}{\partial \Phi_n}\right\}}{\log_e\left\{\Phi_{1_n}\right\} - \log_e\left\{\Phi_{o_n}\right\}} + 1.0 \tag{7.4}$$

where the quantity Φ_1 refers to the design variable vector from the previous iteration and the quantity Φ_o denotes the current design vector. A similar expression is derived for the constraint vector. The exponent p_n can be considered as a "goodness of fit" parameter, which explicitly determines the trade-offs between traditional and reciprocal Taylor series based expansions. Therefore, the procedure can also be regarded as a hybrid approximation technique. It can be seen from Eqn. 7.3 that in the limiting case of $p_n = 1$, the expansion is identical to the traditional first order Taylor series and when $p_n = -1$, the two-point exponential approximation reduces to the reciprocal expansion form. The exponent is then defined to lie within this interval. Therefore, if the exponent $p_n > 1$, it is set identically equal to one and if $p_n < -1$, it is set equal to -1. From Eqns. 7.3 and 7.4, it is obvious that many singularity points exist in the use of this method. Therefore, care

must be taken to avoid such points. In the present study, the linear Taylor series approximation is used at such singular points.

To ensure the validity of the approximation it is necessary to impose bounds, or "move limits" on the design variables during the optimization so that the design point remains in the neighborhood of the original point. These move limits represent a percent change from the original design variable. The move limits in this study are calculated based on a variable scheme developed by Thomas et al. [123]. This algorithm adjusts the values of the move limits based on changes in the maximum violated constraint and also by tracking the individual move limits to see whether they reach the same upper or lower limit over three consecutive evaluations. Another important aspect of the scheme developed in Ref. 123 is the ability to allow design variables to cross over between negative and positive values. Details of move limit approach are presented in Ref. 123.

8. Optimization Results

The reference rotor used is representation of the XV-15 proprotor which is an advanced three-bladed gimballed rotor [113,114]. The aerodynamic optimization is performed at a cruise altitude of 25,000 feet and a forward velocity of 400 knots with a rotational speed of 421 RPM. A vehicle weight of 13,000 lbs and aircraft lift to drag ratio (L/D) of 8.4 is assumed. Therefore, the thrust in cruise is constrained to be at 774 lbs for the two engine aircraft. In hover, the aircraft is assumed to be operating at sea level conditions with a rotational speed of 570 RPM and a 12 percent down load effect from the rotor/wing interaction. The thrust in hover is therefore constrained to be at 7280 lbs. The blade is discretized into 10 aerodynamic segments (11 node points) and the composite box beam is similarly discretized into 10 spanwise elements and 1 chordwise element for a total of 564 degrees of freedom. The composite material used in the structural analysis is carbon-PEEK AS4/APC2 [124] and the material properties are presented in Table 8.1. A total of 15 design variables are used during the optimization. The optimum design converges in 35 cycles and the results are presented in Table 8.2 and Figs. 8.1 - 8.6.

Table 8.1 Summary of beam material properties

$E_1 = 19.4 \times 10^6$ p.s.i., $E_2 = 1.29 \times 10^6$ p.s.i.,
$G_{12} = 0.740 \times 10^6$ p.s.i., $G_{13} = 0.500 \times 10^6$ p.s.i.,
$\mu_{12} = 0.28$, $\rho = 1.80 \times 10^{-3}$ slug/in^3

ply thickness = 0.001 in.

Ultimate Strengths

$X^T = 309 \times 10^3$ p.s.i., $X^C = 160 \times 10^3$ p.s.i.,
$Y^T = 11.6 \times 10^3$ p.s.i., $Y^C = 29.0 \times 10^3$ p.s.i.,
$S = 23.2 \times 10^3$ p.s.i.

From Table 8.2 and Fig. 8.1 it is seen that the hover figure of merit (FM) increases by 3.6 percent and the high speed cruise propulsive efficiency (η_{ax}) is significantly improved (55 percent). It must be noted, however, that the baseline rotor was originally designed for operation at 300 knots and therefore has a poor cruise efficiency ($\eta_{ax} = 0.49$) at the optimization design speed of 400 knots. As a result, the improvement in η_{ax} is much more significant compared to the increase in the hover figure of merit which has a fairly high value initially. A complete understanding of the aerodynamic improvements is obtained by examining the design variable trends.

Table 8.2 Comparison of optimum results

	Reference	Optimum
Objective Functions		
FM	0.7691	0.7974
η_{ax}	0.4856	0.7502
Design Variables		
c_o	0.1094	0.1050
c_1	-0.09256	-0.09760
c_2	0.1575	0.1630
c_3	-0.08176	-0.07630
θ_1 (rad.)	-0.3455	-0.3443
θ_2 (rad.)	0.7693	0.5817
θ_3 (rad.)	-0.1461	-0.1057
t_o	0.3155	0.2167
t_1	-0.3193	-0.2370
t_2	0.07517	0.09128
a_o	0.000	-0.05615
β_1 (deg.)	0.0	0.0
β_2 (deg.)	0.0	0.5
β_3 (deg.)	0.0	-1.7
β_4 (deg.)	0.0	-1.5

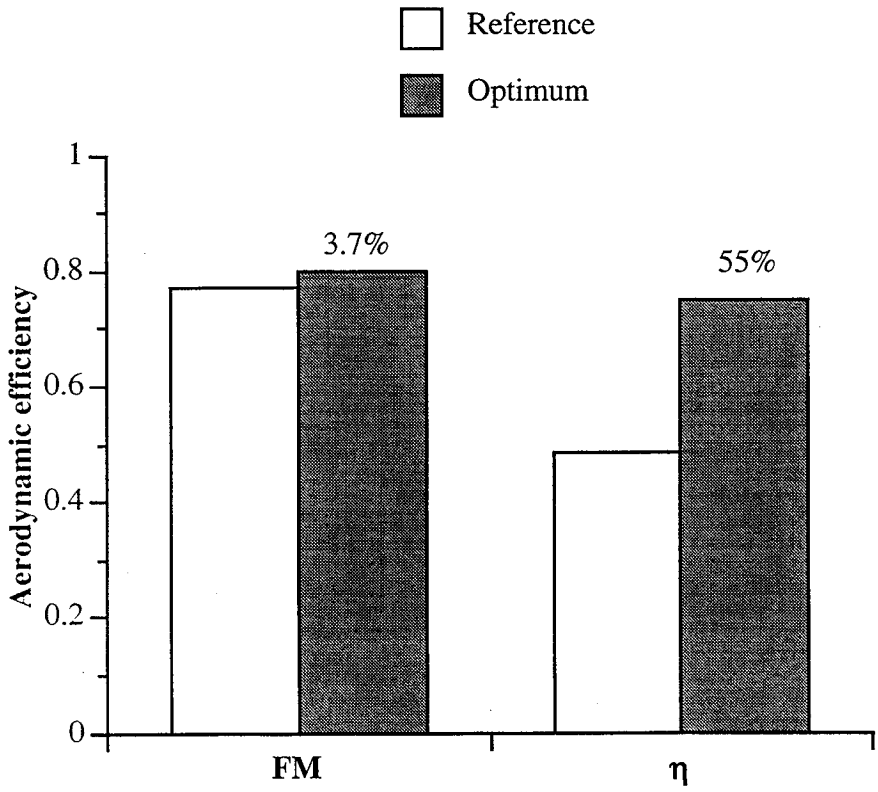

Fig. 8.1 Comparison of optimum results.

The optimum chord distribution is presented in Fig. 8.2 and shows that the chord distribution over the majority of the blade span is reduced from the baseline values. At the tip, however, the chord is actually increased. It is important to note that although the area weighted solidity (σ_A) is slightly decreased from the reference value (2.8 percent), both the thrust weighted solidity (σ_T) and the power weight solidity (σ_P) are not decreased as much (2.3 percent and 1.8 percent, respectively) as shown in Fig. 8.3. The solidity ratios are defined as follows.

$$\sigma_i = \frac{b\,\bar{c}_i}{\pi R}, \qquad i = A, T \text{ or } P, \tag{8.1}$$

where

$$\bar{c}_A = \frac{\int_0^1 c\,\bar{x}\,d\bar{x}}{\int_0^1 \bar{x}\,d\bar{x}}, \tag{8.2}$$

$$\bar{c}_T = \frac{\int_0^1 c\,\bar{x}^2\,d\bar{x}}{\int_0^1 \bar{x}^2\,d\bar{x}}, \tag{8.3}$$

$$\bar{c}_P = \frac{\int_0^1 c\,\bar{x}^3\,d\bar{x}}{\int_0^1 \bar{x}^3\,d\bar{x}}. \tag{8.4}$$

In the above equations, c is blade chord and $\bar{x}$ is the nondimensional radius. The reason for the reduced chord near the root is due to the fact that in the reference blade this section produces a significant amount of drag in cruise (Fig. 8.4) without generating any significant lift (Fig. 8.5). After optimization, it is seen that the drag is significantly reduced in this region whereas the lift is only slightly affected. In hover, the root section generates very little lift and drag (Figs. 8.6 and 8.7, respectively) therefore the root chord is reduced only due to constraints on the stresses. In the absence of the stress constraints, it is likely that the root chord would be reduced to smaller values. As a result, the optimizer reduces the chord throughout the blade span, except near the tip. It is interesting to note, that in the optimum configuration, there is an increase in the chord values from about midspan towards the tip, resulting in a slight inverse taper. This is due to the fact that this outboard section represents the working section of the blade. In both hover and in cruise, the majority of the lift is produced by the outer 25 percent of the blade. By increasing the

chord in this region of the blade, the optimizer is redistributing the load to a region which is beneficial to both flight conditions.

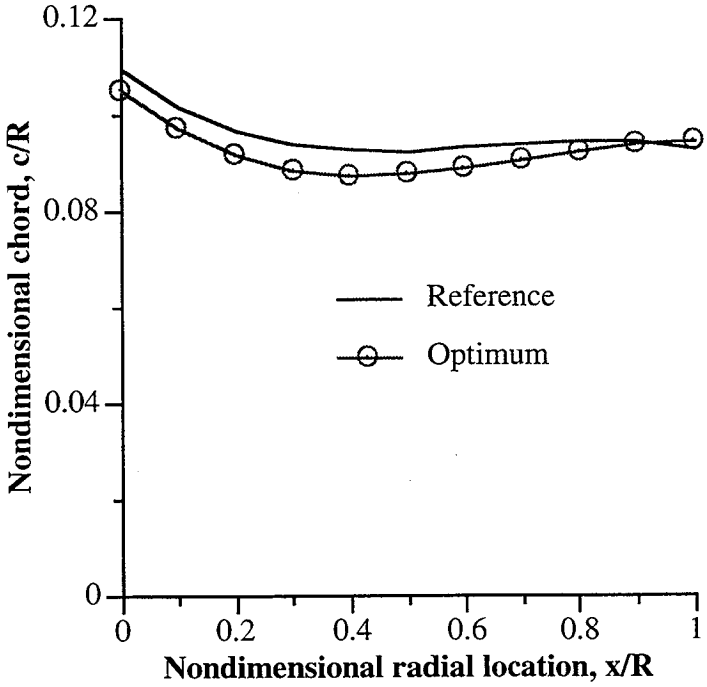

Fig. 8.2 Comparison of chord distributions.

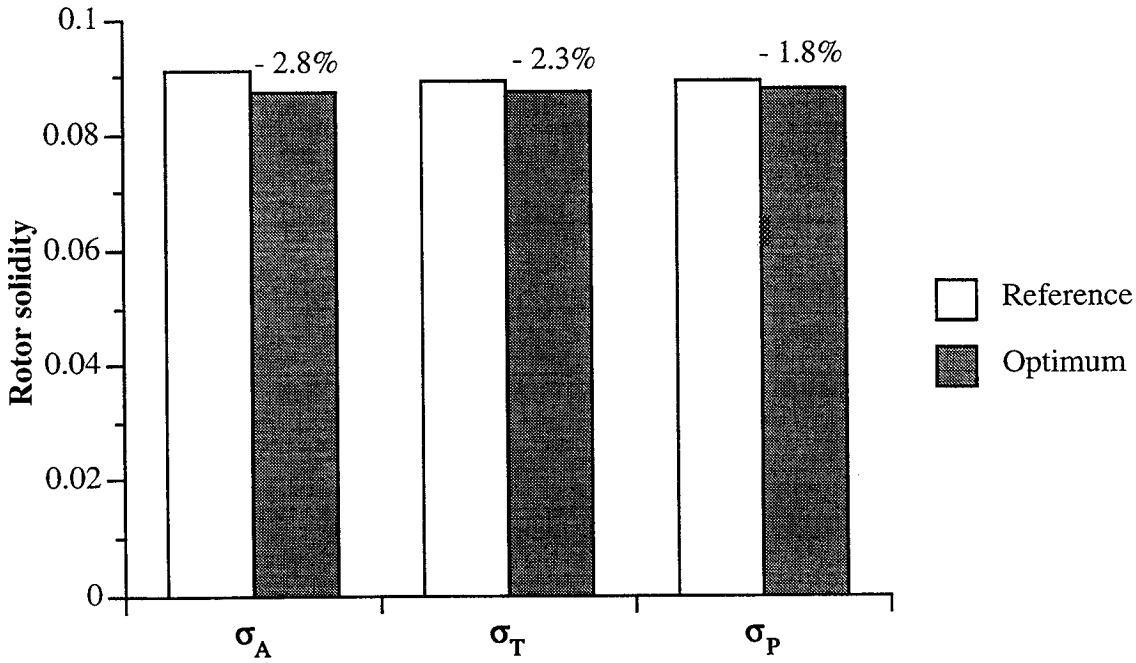

Fig. 8.3 Comparison of rotor solidity.

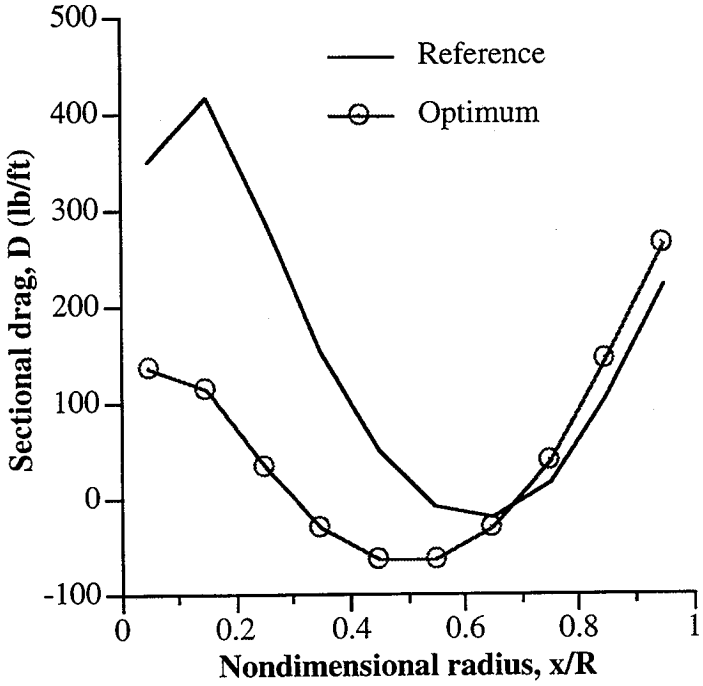

Fig. 8.4 Comparison of high speed cruise sectional drag.

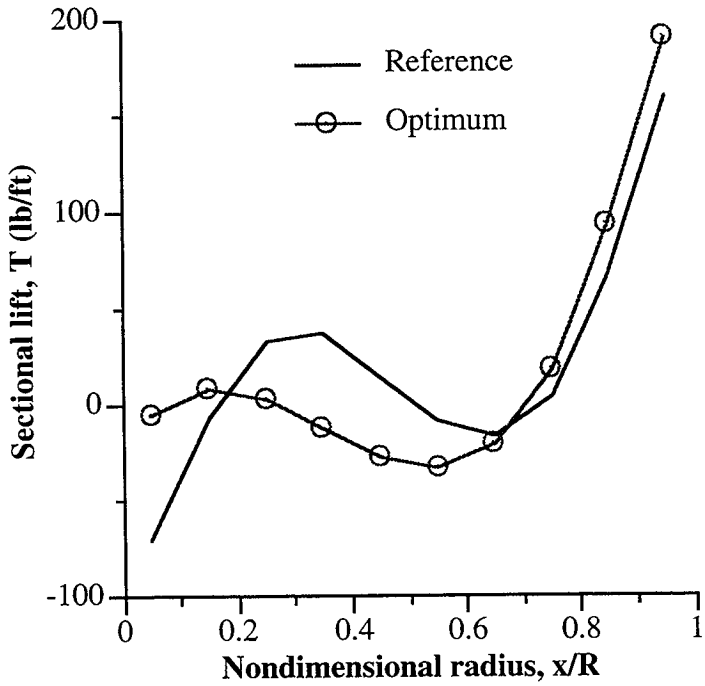

Fig. 8.5 Comparison of high speed cruise sectional lift.

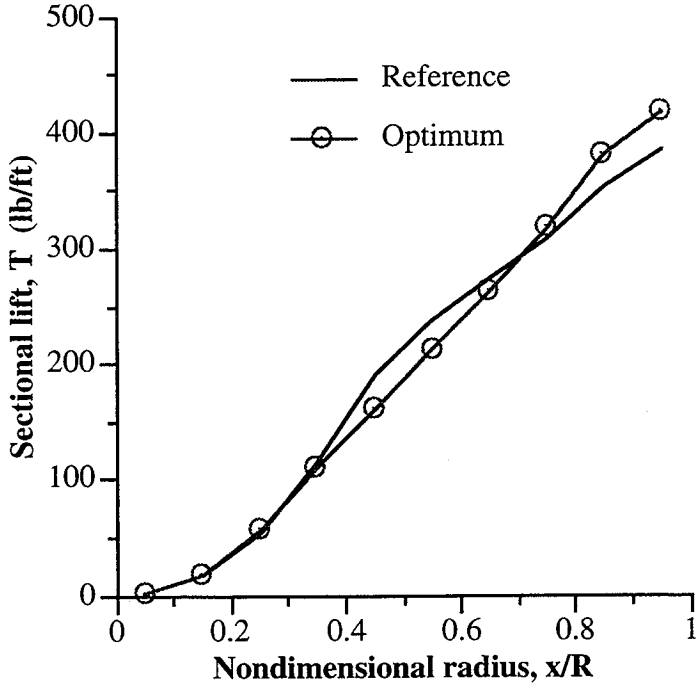

Fig. 8.6 Comparison of hover sectional lift.

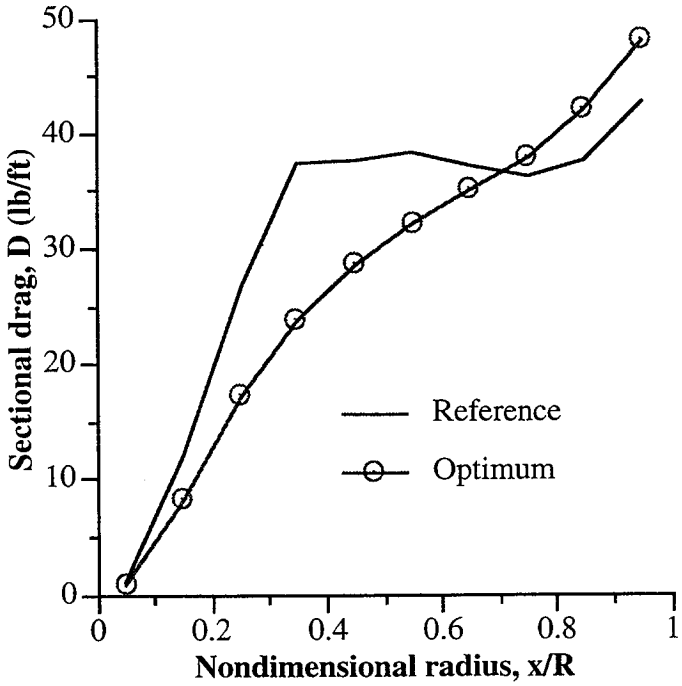

Fig. 8.7 Comparison of hover sectional drag.

The optimum and the reference blade thickness distributions are presented in Fig. 8.8. From the figure it is seen the blade thickness is reduced from the reference values throughout the entire span, except at the tip. One reason for this reduction is to reduce the profile drag of the blade by reducing the thickness. Reductions in the profile drag, in turn improves the aerodynamic performance. A second reason for this reduction is to increase the drag divergence Mach number (M_{dd}). This Mach number is defined as the point where a further increase in Mach number will result in a sharp increase in the drag [111]. In the reference blade the local Mach numbers near the tip in cruise are very near M_{dd}. Through reductions in the blade thickness distributions, the optimizer increases M_{dd} throughout the blade and as a result the drag is reduced improving the performance of the rotor. The constraints imposed on the blade thickness at the tip prevent the optimizer from reducing the tip thickness below the reference value. Near the tip, these constraints become active and as a result no further reductions in blade thickness are obtained in this region.

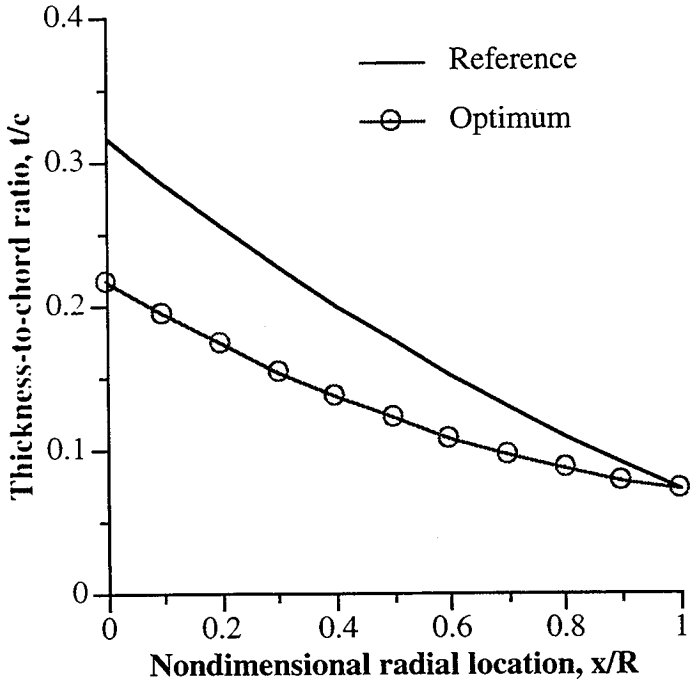

Fig. 8.8 Comparison of thickness-to-chord distributions.

Figure 8.9 presents the twist distributions of both the reference and the optimum rotors where it is seen that the twist is reduced from root to about midspan of the rotor. These reductions are due to the fact that the optimizer is attempting to unload this section of the blade since the drag in the cruise condition is very high for the reference blade (Fig. 8.4). The effective angle of attack is lower as a result of the reduction in blade twist and this results in reductions in both lift and drag in the region. This is again due to the fact that the optimizer is redistributing the lift outboard towards the tip to improve the performance. Near the tip, the twist distributions are very similar.

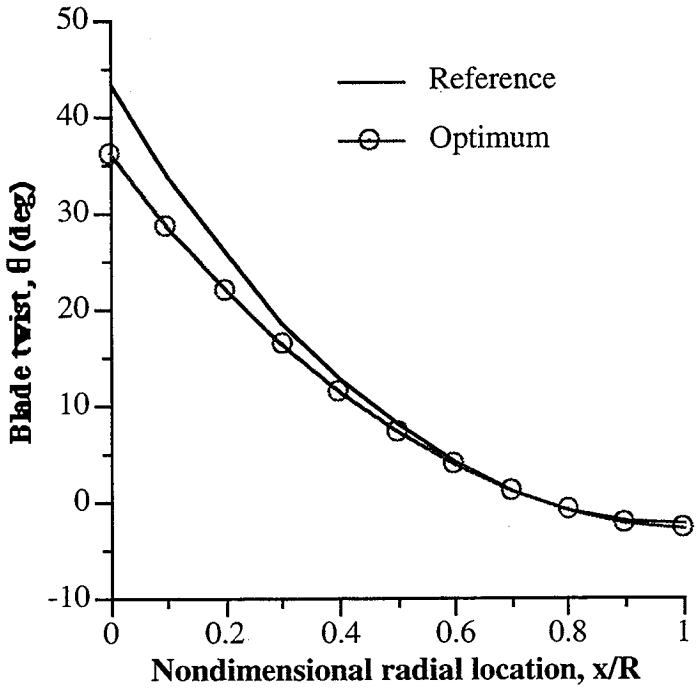

Fig. 8.9 Comparison of twist distributions.

The lifting line offset (Y_{ac}) and the resulting sweep distribution ($\hat{\Lambda}$) are presented in Figs. 8.10 and 8.11. These figures indicate that very little sweep is introduced after optimization and that the blade is swept forward. This can be explained as follows. The introduction of sweep reduces the effective Mach number which in turn improves the performance of the high speed cruise propulsive efficiency. However, only a slight

amount of sweep is introduced (about 3 degrees at the tip) and the reductions in the effective Mach numbers are not significant. This is due to the fact that in cruise there is a large nose down moment throughout the blade span. These moments are larger than the corresponding moments introduced through the lifting distribution and the offset of the aerodynamic center from the axis of twist. As a result, the blade twists down in cruise. However, in hover, the moments due to the lifting distribution and the aerodynamic offset are much larger than the corresponding moments due to the aerodynamic pitching moments. Therefore the blade twists backward (nose up) in hover. By sweeping the blade slightly forward, the offset between the lift and the axis of twist is increased and this reduces the amount of negative twist in cruise which in turn improves the performance. However, the forward sweep increases the amount of positive twist in hover and as a result only a slight amount of twist can be allowed without adversely affecting the hover performance. Further, a significant amount of sweep would increase the bending moments which would result in increased blade stresses.

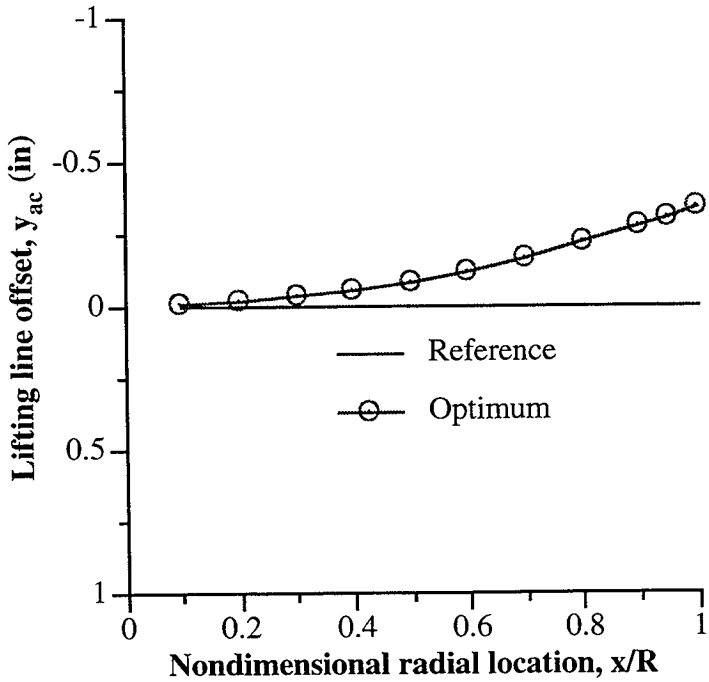

Fig. 8.10 Comparison of lifting line distributions.

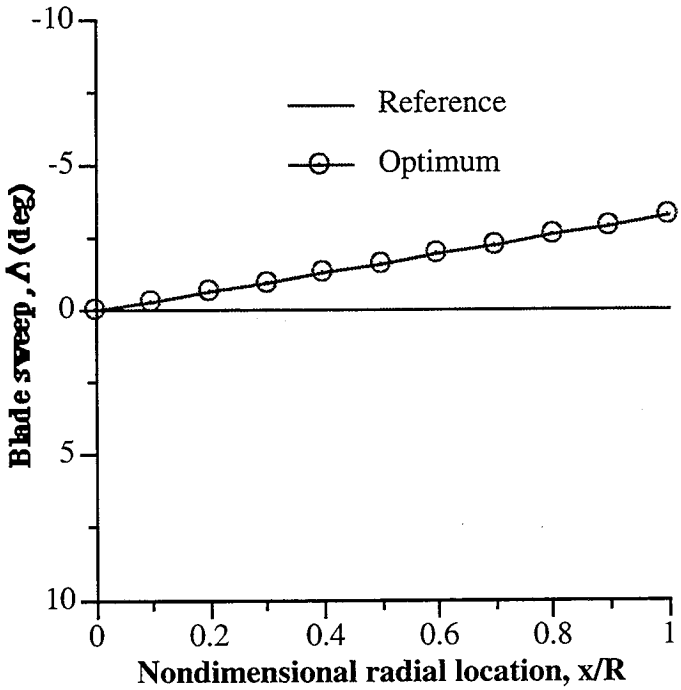

Fig. 8.11 Comparison of blade sweep distributions.

The stability roots of the five most critical modes are presented in Figs. 8.12 (hover) and 8.13 (cruise). The figures show that in both flight conditions the real part of the stability root is negative for both the reference and optimum rotors assuring that the system is stable. It is further seen in the figures that an imaginary line drawn through the locus of roots, originating at the origin, is nearly linear. This is due to the fact that the damping due to aerodynamics is small. Therefore, the structural damping (assumed to be two percent, proportional damping) dominates the aerodynamic damping. This is caused by several factors. First, due to the large loads under which the blade operates (each blade must generate nearly 2500 lbs of thrust), the blade must be extremely stiff in order to withstand the bending stresses. Also, unlike fixed wing aircraft, the aerodynamic loading is not significantly altered with changes in forward speed due to the fact that the rotor is trimmed to a constant thrust value.

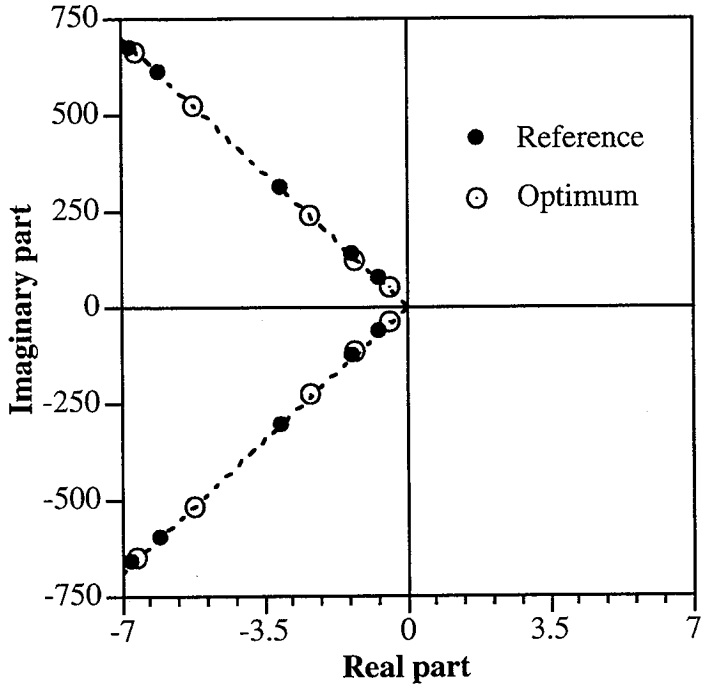

Fig. 8.12 Comparison of hover stability roots; 2 percent structural damping.

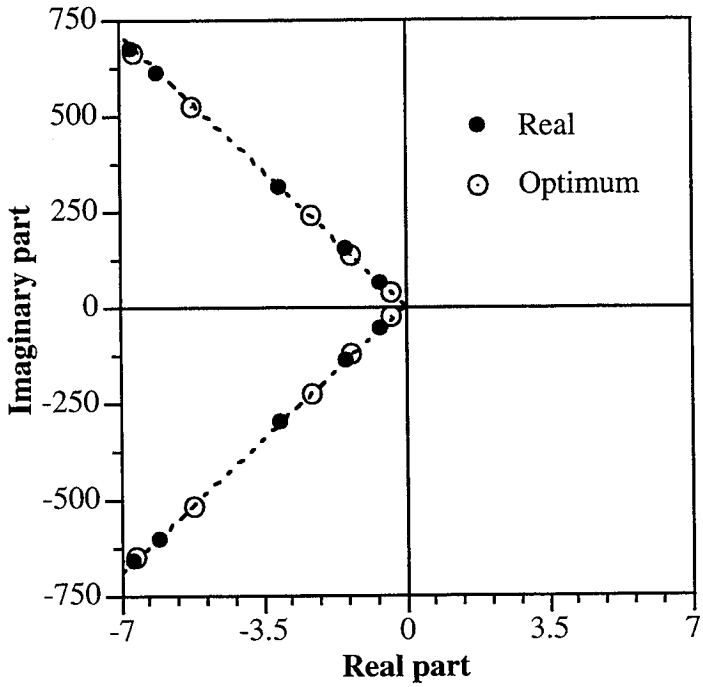

Fig. 8.13 Comparison of high speed cruise stability roots; without structural damping.

The optimum ply angles are presented in Table 8.2. Very little changes are observed between the reference and the optimum values. This is due to the fact that the stability constraints are never critical during optimization. Since the ply angles have very little effect on the aerodynamic performance and the stability roots are never near critical, there is little change in the ply angles after optimization. Figures 8.14 - 8.21 present the midplane stresses in the individual walls, at each corner, before and after optimization. These figures illustrate the increase in the root stresses in each wall for both flight conditions and show that these stresses are more critical in hover (Figs. 8.14 - 8.17) than in cruise (Figs. 8.18 - 8.21) . The increase in the stresses once again due to the reduction in cross-sectional area which is caused by the reductions in root chord. Although, the stresses are increased after optimization, the overall Tsai-Wu criterion is satisfied at each ply level at every corner for both flight conditions. In the absence of these stress constraints, it is likely that the optimizer would have further reduced the root chord in order to improve the aerodynamic performance.

To fully investigate the phenomenon of tilt-rotor aeroelastic stability, the combined problem of the wing/rotor/pylon assembly of the tilt-rotor aircraft should be investigated. Further, the use of a more comprehensive aerodynamic analysis, such as panel code, may be beneficial. If such measures were taken, it is believed the ply angles (particularly in the aircraft wing) would have played a more significant role on the overall performance and stability of tilt-rotors.

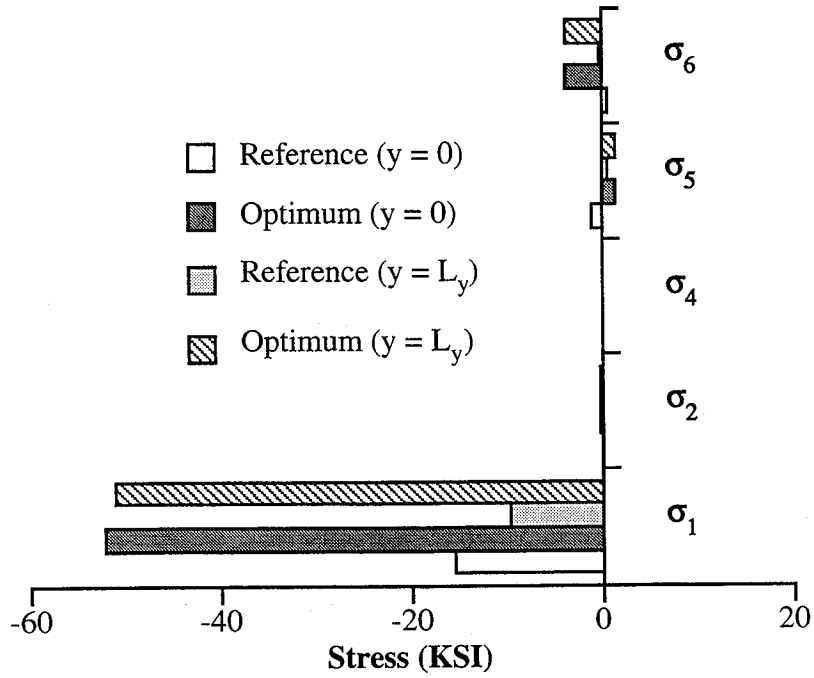

Fig. 8.14 Comparison of midplane stresses; top wall, hover.

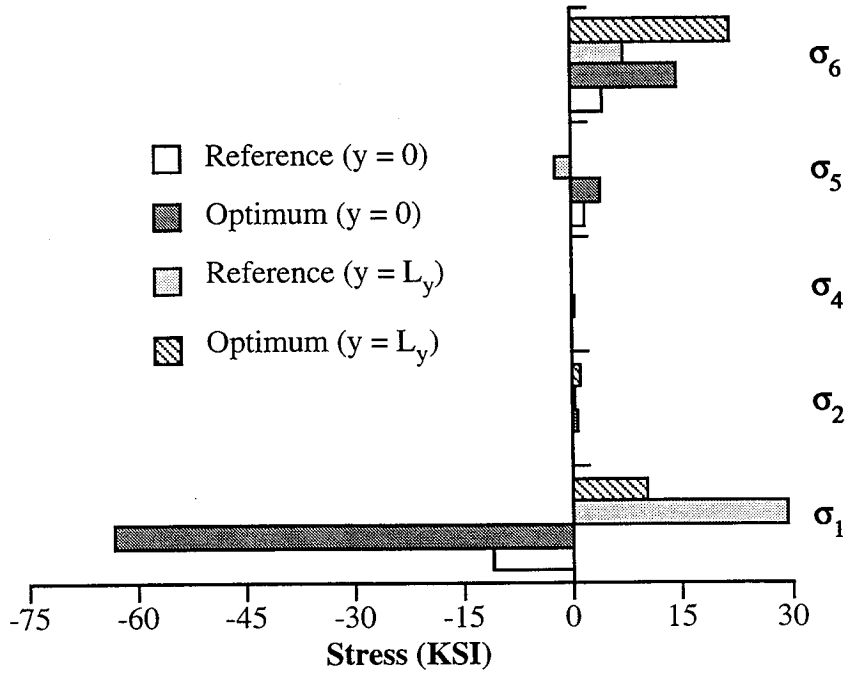

Fig. 8.15 Comparison of midplane stresses; right wall, hover.

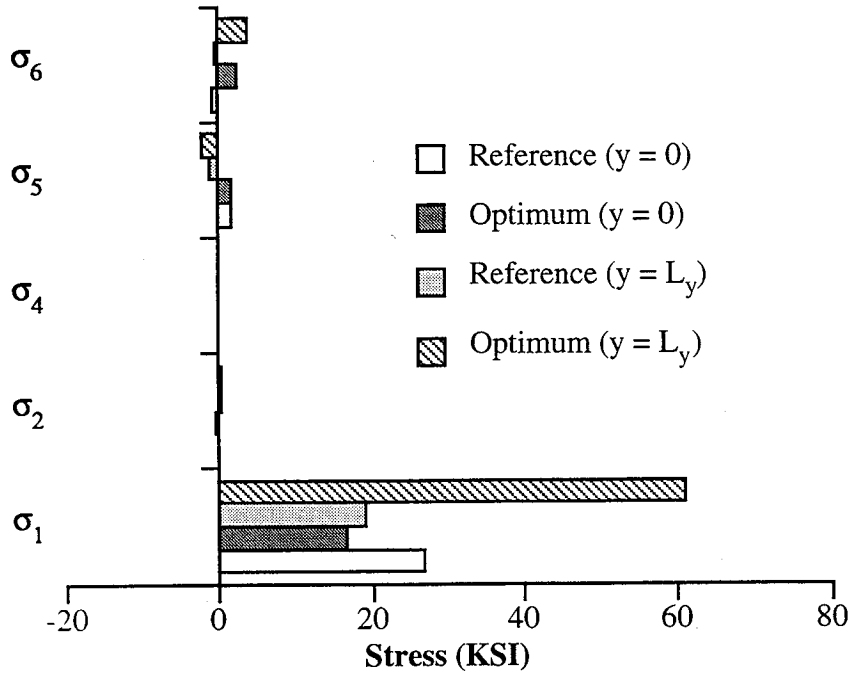

Fig. 8.16 Comparison of midplane stresses; bottom wall, hover.

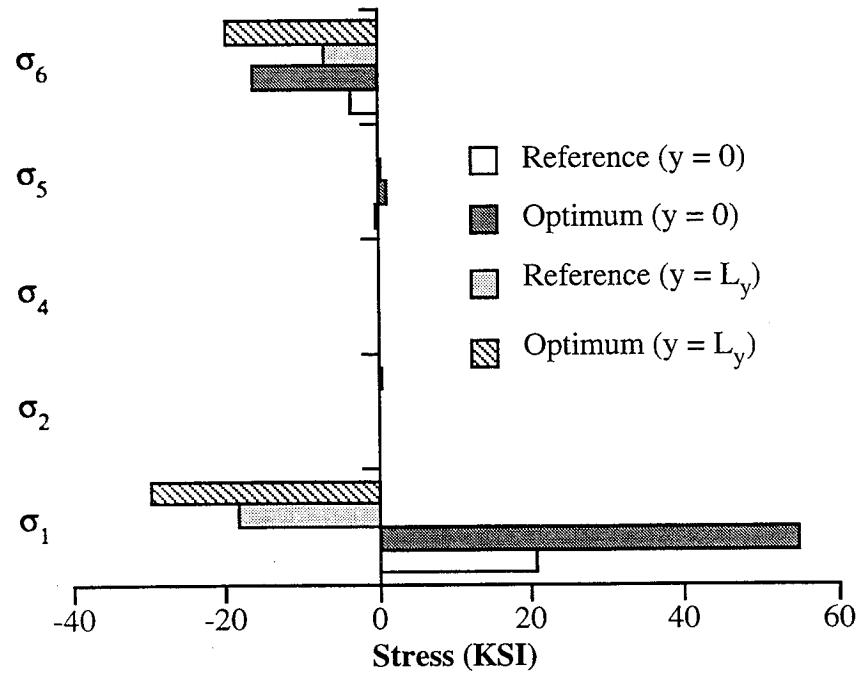

Fig. 8.17 Comparison of midplane stresses; left wall, hover.

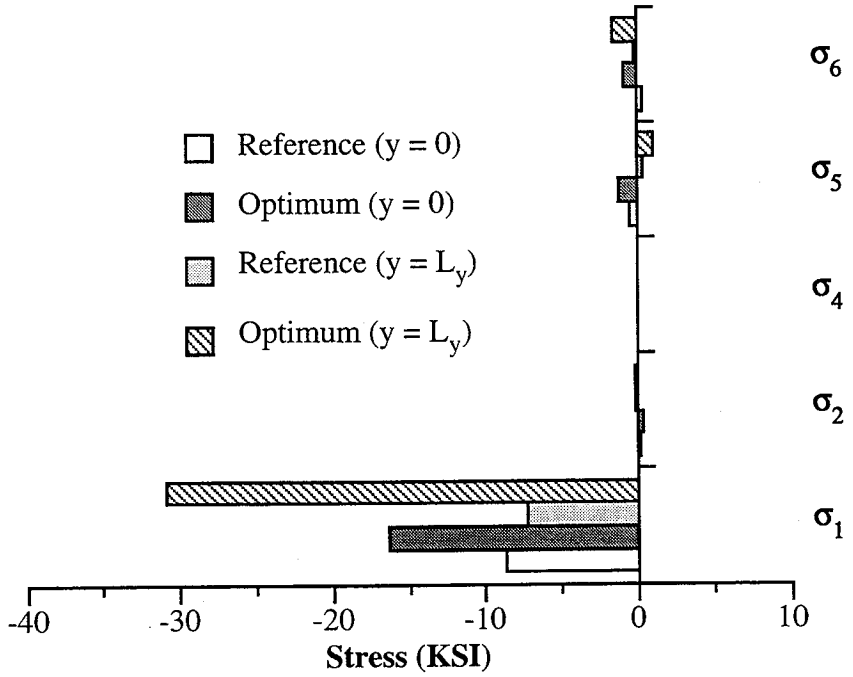

Fig. 8.18 Comparison of midplane stresses; top wall, high speed cruise.

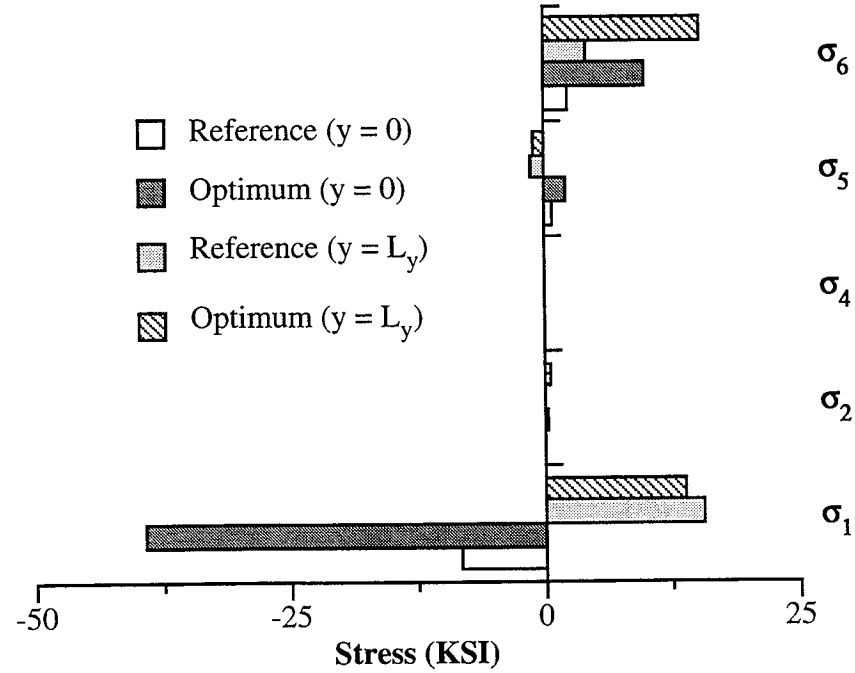

Fig. 8.19 Comparison of midplane stresses; right wall, high speed cruise.

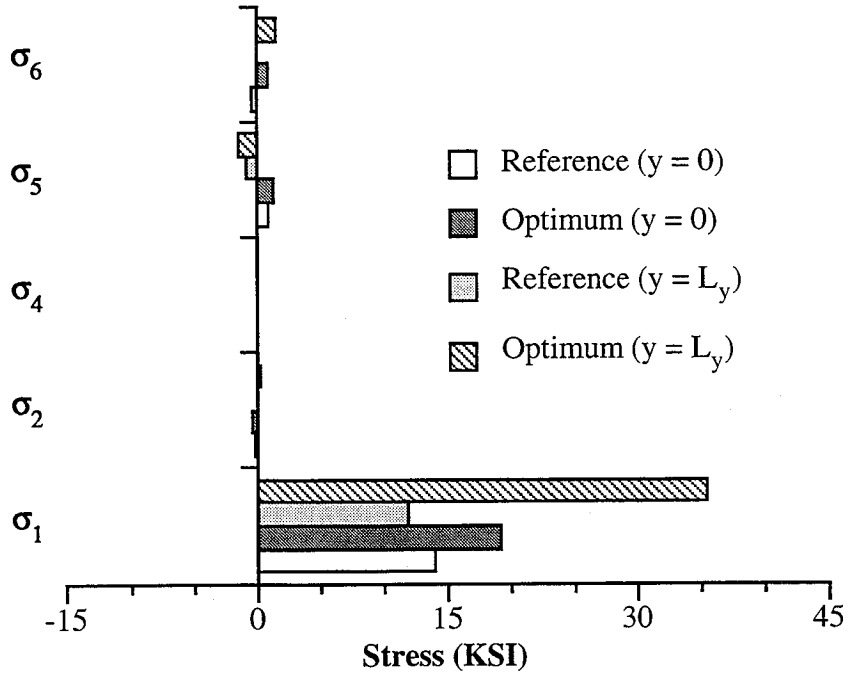

Fig. 8.20 Comparison of midplane stresses; bottom wall, high speed cruise.

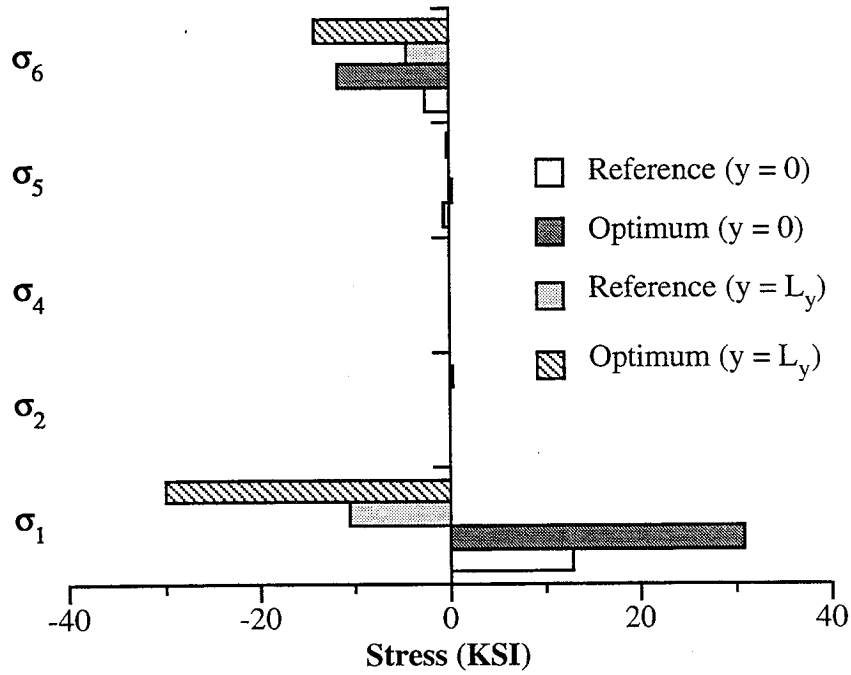

Fig. 8.21 Comparison of midplane stresses; left wall, high speed cruise.

9. Concluding Remarks

A new beam theory has been developed to model composite box beams with arbitrary wall thicknesses. The theory, which is based on higher-order composite laminate theory, approximates the three-dimensional elasticity solution rather than reducing the cross-sectional properties to one-dimensional beam properties. Arbitrary spanwise distributions of blade twist, taper and sweep are included in the formulation. The developed theory satisfies the stress free boundary conditions on the inner and outer surfaces of the beam. Both inplane and out-of-plane warping are included in the formulation.

Next a procedure for the aeroelastic stability of prop-rotor blades has been developed. The aerodynamic loads are based on the classical blade element momentum theory. The coupled equations of motion are developed which represent a trimmed blade configuration. Finally, the developed structural, aerodynamic and aeroelastic procedure are integrated within an optimization procedure to investigate prop-rotor performance in both high speed cruise and hover. The optimization problem includes multiple objectives and the Kreisselmeier-Steinhauser (K-S) function is used to formulate the optimization problem. This function represents an envelope function of all of the objective functions and constraints and transforms the problem to an unconstrained optimization problem. The Broyden-Fletcher-Goldfarb-Shanno (BFGS) algorithm is used to determine the search direction. The procedure is coupled with a hybrid approximate expansion is used to reduce the computational effort. The following important observations are made.

1. Very good overall agreement is observed between the static results and available experimental data for thin-walled beams. The dynamic results correlate well with NASTRAN using both solid elements and shell elements.

2. For large angle ply laminates (e.g. 45°), the present approach predicts the behavior very well as shown by the correlation with experimental results. For these

laminates, the present approach represents a significant improvement from a previously developed quasi-analytical method.

3. The results from the symmetric beams have better overall correlation than the anti-symmetric beams. This is due to the fact that magnitude of the twist measured for the anti-symmetric beam correlation is very small and therefore is more difficult to determine experimentally.

4. The effect of transverse shear stresses is critical in case of thick-walled sections. This introduces large nonlinearities in the twist distribution. Further, the local twist in the individual walls is not equal as it is in case of thin-walled beams.

5. The "beam" twist is a local quantity which can only be defined at a point in the cross section. Arbitrary definition of the twist at a convenient point in the beam cross-section is inaccurate for thick-walled cross sections.

6. The modes shapes often display a significant amount of bending-twist coupling and/or extension-shear coupling. The coupling is more noticeable in beams with thicker wall sections.

7. The present beam theory captures the effects of inplane and out-of-plane warping. For thick-walled beams with low aspect ratios, the warping terms are significant even at the lower modes. For the thin-walled beams, the inplane warping is more important than the out-of-plane warping. Results obtained using NASTRAN tend not to capture the lower warping modes.

8. The increased warping in beams with thicker walls is due to the presence of transverse shear stresses through the thickness of the walls which increases with laminate thickness.

9. The multidisciplinary optimization developed yields significant improvements in the aerodynamic performance without any degradation of the structural response and aeroelastic stability.

10. Improvements in the aerodynamic performance are obtained largely through changes in the blade chord, twist and thickness distribution. By changing the chord and twist, the load is redistributed to the outboard sections of the blade. Reductions in the blade thickness reduce the profile drag thereby increasing the performance.

11. The optimizer does not significantly alter the blade sweep due to the conflicting requirements between the two flight conditions.

12. Changes in the ply angles are negligible due to the fact that aeroelastic stability constraints are never critical to optimization.

13. Using the current aerodynamic analysis, the aeroelastic stability of prop-rotor blades is not a significant issue due to the fact blade must be extremely stiff in order to withstand bending stresses and the fact that the blade is trimmed to a constant thrust value. A more complete representation of the aircraft, including the wing/rotor/pylon assembly is recommended in order to better evaluate the aeroelastic stability of tilt-rotor aircraft.

10. References

1. Wilkerson, J. B., Schneider, J. J. and Bartie, K. M., "Technology Needs for High-Speed Rotorcraft (1)", NASA CR 177585, May 1991.

2. Scott, M. W., "Technology Needs for High-Speed Rotorcraft (2)", NASA CR 177590, August 1991.

3. Rutherford, J. et al., "Technology Needs for High-Speed Rotorcraft," NASA CR 177578, April 1991.

4. Detore, J. and Conway, S., "Technology Needs for High Speed Rotorcraft (3)," NASA CR XXXX, NAS2 - 13072, 1991.

5. Dadone, L., Lui, J., Wilkerson, J. and Acree, C. W., "Proprotor Design Issues for High Speed Tiltrotors," Proc. 50th Annual Forum of the American Helicopter Society, Washington, DC, May 1994.

6. Felker, F. F., "Wing Download Results from a Test of a 0.658-Scale V-22 Rotor and Wing," Journal of the American Helicopter Society, Vol. 37, No. 4, October 1992, pp. 58-63.

7. Chattopadhyay, A. and Narayan, J., "Optimum Design of High Speed Prop-Rotors Using a Multidisciplinary Approach," *Engineering Optimization*, Vol. 22, pp. 1-17, 1993. Also presented *at the 48th Annual Forum of the American Helicopter Society*, June 3 - 5, 1992, Washington DC.

8. McCarthy, T. R., An Integrated Multidisciplinary Optimization Approach For Rotary Wing Design, Master's Thesis, Arizona State University, July 1992.

9. McCarthy, T. R. and Chattopadhyay, A, "Design of High Speed Proprotors Using Multiobjective Optimization Techniques," *Engineering Optimization*, Vol. 23, pp. 155-172, 1994.

10. Chattopadhyay, A., McCarthy, T. R. and Madden, J. F., "Structural Optimization of High Speed Prop Rotors Including Aeroelastic Stability Constraints," *Mathematical and Computer Modelling*, Special Issue on Rotorcraft, Vol. 18, No. 3/4, pp. 101-113, 1993.

11. Chattopadhyay, A., McCarthy, T. R. and Madden, J. F., "A Design Optimization Procedure for Minimizing Drive System Weight of High Speed Prop-Rotors," *Engineering Optimization*, Vol. 23, pp. 239-254, 1995.

12. Chattopadhyay, A., McCarthy, T. R. and Madden, J. F., "An Optimization Procedure for the Design of Prop Rotors In High Speed Cruise Including the Coupling of Performance, Aeroelastic Stability and Structures" *Mathematical and Computer Modelling*, Special Issue on Rotorcraft, Vol. 19, No. 3/4, pp. 75-88, 1994.

13. McCarthy, T. R., Chattopadhyay, A., Talbot, P. D., and Madden, J. F., "A Performance Based Optimization of High Speed Prop-Rotors," *Journal of the American Helicopter Society*, Vol. 40, No. 3, pp. 92-100, July 1995.

14. Chattopadhyay, A., McCarthy, T. R. and Seeley, C. E., "A Decomposition Based Optimization Procedure for High Speed Prop-Rotors using Composite Tailoring and Simulated Annealing," *Journal of Aircraft*, Vol. 32, No. 5, pp. 1026-1033, Oct. 1995.

15. Chattopadhyay, Aditi, McCarthy, Thomas R. and Seeley, Charles E., "A Multiple Design Point Optimization of High Speed Proprotors," *Journal of Aircraft*, Vol. 33,

No. 3, pp 625 - 627, June 1996. Also *Proc.* Twentieth European Rotorcraft Forum, paper no. 47, Amsterdam, The Netherlands, October 1994.

16. McCarthy, Thomas R. and Chattopadhyay, Aditi, "A Coupled Rotor/Wing Optimization Procedure for High Speed Tilt Rotor Aircraft," *Journal of the American Helicopter Society* (in press, 1996).

17. Reed, W. H., "Propeller-Rotor Whirl Flutter: A State-Of-The-Art Review," Journal of Sound and Vibration, Vol. 4, No. 3, 1966, pp. 526-544.

18. Kvaternik, R. G., "A Review of Some Tilt-Rotor Aeroelastic Research at NASA-Langley," Journal of Aircraft, Vol. 13, No. 5, May 1976, pp. 357-363.

19. Friedmann, P. P, "Helicopter Rotor Dynamics and Aeroelasticity: Some Key Ideas and Insights," Vertica, Vol. 14, No. 1, 1991, pp. 101-121.

20. Edenborough, H. K., "Investigation of Tilt-Rotor VTOL Aircraft Rotor-Pylon Stability," Journal of Aircraft, Vol. 5, No. 2, March 1968, pp. 97-105.

21. Kaza, K. R. V., "Effect of Steady State Coning Angle and Damping on Whirl Flutter Stability," Journal of Aircraft, Vol. 10, No. 11, Nov. 1973, pp. 660-669.

22. Johnson, W., "Dynamics of Tilting Proprotor Aircraft in Cruise Flight," NASA TN D-7677, May 1974.

23. Johnson, W., "Analytical Modeling Requirements for Tilting Proprotor Aircraft Dynamics," NASA TN D-8013, July 1975.

24. Johnson, W., "An Assessment of the Capability To Calculate Tilting Prop-Rotor Aircraft Performance Loads, and Stability," NASA TP 2291, March 1984.

25. Johnson, W., "Recent Developments in the Dynamics of Advanced Rotor Systems," NASA TM 86669, March 1985.

26. Mansfield, E. H. and Sobey, A. J., "The Fibre Composite Helicopter Blade," Aeronautical Quarterly, May 1979, pp. 413-449.

27. Chopra, I. and Sivaneri, N. T., "Aeroelastic Stability of Rotor Blades Using Finite Element Analysis," NASA CR 166389, Aug. 1982.

28. Hong, C. H. and Chopra, I., "Aeroelastic Stability Analysis of a Composite Rotor Blade," Journal of the American Helicopter Society, Vol. 30, No. 2., April 1985, pp. 57-67.

29. Hong, C. H. and Chopra, I., "Aeroelastic Stability Analysis of a Composite Bearingless Rotor Blade," Journal of the American Helicopter Society, Vol. 31, 1986, pp. 29-35.

30. Rosen, A. and Rand, O., "Static Aeroelastic Behavior of Curved Helicopter Blades in Hovering and Axial Flight," Vertica, Vol. 7, No. 3, 1983, pp. 241-257.

31. Nasu, K., "Tilt-Rotor Flutter Control in Cruise Flight," NASA TM 88315, Dec. 1986.

32. Torok, M. S. and Chopra, I., "Hingeless Rotor Aeroelastic Stability Analysis with Refined Aerodynamic Modeling," Journal of the American Helicopter Society, Vol. 36, 1991, pp. 48-56.

33. Smith, E. C. and Chopra, I., "Aeroelastic Response and Blade Loads of a Composite Rotor in Forward Flight," Paper No. AIAA 92-2466-CP, Proc. 33rd

Structures, Structural Dynamics, and Materials Conference, Dallas, Texas, April 1992, pp. 1996-2014.

34. Smith, E. C., "Vibration and Flutter of Stiff-Inplane Elastically Tailored Composite Rotor Blades," Paper No. AIAA 93-1302-CP, Proceedings, 34th Structures, Structural Dynamics, and Materials Conference, La Jolla, California, April 1993, pp. 26-37.

35. Nixon, M. W., "Parametric Studies for Tiltrotor Aeroelastic Stability in High-Speed Flight," Paper No. AIAA-92-2568-CP, Proceedings, 33rd Structures, Structural Dynamics, and Materials Conference, Dallas, Texas, April 1992, pp. 2027-2037.

36. Nixon, M. W., Aeroelastic Response and Stability of Tiltrotors with Elastically-Coupled Composite Rotor Blades, Ph.D. Thesis, Department of Aerospace Engineering, University of Maryland, College Park, Maryland, 1993.

37. Bir, G. S. and Chopra, I., "Aeromechanical Stability of Rotorcraft with Advanced Geometry Blades," Paper No. AIAA 93-1304-CP, Proceedings, 34th Structures, Structural Dynamics, and Materials Conference, La Jolla, California, April 1993, pp. 38-62.

38. Tracy, A. L. and Chopra, I., "Aeromechanical Stability of a Bearingless Composite Rotor in Forward Flight," Paper No. AIAA 93-1305-CP, Proceedings, 34th Structures, Structural Dynamics, and Materials Conference, La Jolla, California, April 1993, pp. 63-79.

39. Kim, T. and Dugundji, J., "Nonlinear Large Amplitude Aeroelastic Behavior of Composite Rotor Blades," AIAA Journal, Vol. 31, No. 8, Aug. 1993, pp. 1489-1497.

40. Yen, J. G., "Effect of Blade Tip Shape on Rotor Dynamics and Aeroelastic Response," Proceedings, 19th European Rotorcraft Forum, Cernobbio, Italy, Sep. 1993, Paper No. G8.

41. Nibbeling, B. D and Peters, D. A., "Flutter Calculations for Fixed and Rotating Wings with State-Space Inflow Dynamics," Paper No. AIAA 93-1300-CP, Proceedings, 34th Structures, Structural Dynamics, and Materials Conference, La Jolla, California, April 1993, pp. 1-11.

42. Yuan, K. A. and Friedmann, P. P., "Aeroelastic Stability, Response and Loads of Swept Tip Composite Rotor Blades in Forward Flight," Paper No. AIAA-94-1309-CP. Proc. 35th Structures, Structural Dynamics and Materials Conference, Hilton Head, SC, April 1994, pp. 23-42.

43. Ganguli, R. and Chopra, I., "Aeroelastic Optimization of a Composite Helicopter Rotor," Paper No. 92-4780, Proceedings, 4th AIAA/USAF/NASA/OAI Symposium on Multidisciplinary Analysis and Optimizations, Cleveland, Ohio, Sep. 1992.

44. Ganguli, R. and Chopra, I., "Aeroelastic Optimization of a Helicopter Rotor with Composite Tailoring," Proceedings, 49th Annual Forum of the American Helicopter Society, St. Louis, Missouri, May 1993, pp. 1335-1354.

45. Hodges, D. H. and Dowell, E. H., "Nonlinear Equations of Motion for the Elastic Bending and Torsion of Twisted Nonuniform Rotor Blades," NASA TN D-7818, Dec. 1974.

46. Hodges, D. H., Ormiston, R. A. and Peters, D. A., "On the Nonlinear Deformation Geometry of Euler-Bernoulli Beams," NASA TP-1566, April 1980.

47. Wörndle, R., "Calculation of the Cross Section Properties and the Shear Stresses of Composite Rotor Blades," Vertica, Vol. 6, 1982, pp. 111-129.

48. Giavotto, V., et al., "Anisotropic Beam Theory and Applications," Computers and Structures, Vol. 16, No. 1-4, 1983, pp. 403-413.

49. Krenk, S. and Gunneskov, O., "Pretwist and Shear Flexibility in the Vibrations of Turbine Blades," Journal of Applied Mechanics, Vol. 52, June 1985, pp. 409-415.

50. Bauchau, O. A., "A Beam Theory for Anisotropic Materials," Journal of Applied Mechanics, Vol. 52, June 1985, pp. 416-422.

51. Bauchau, O. A. and Hong, C. H., "Large Displacement Analysis of Naturally Curved and Twisted Composite Beams," AIAA Journal, Vol. 25, No. 11, Nov. 1987, pp. 1469-1475.

52. Bauchau, O. A. and Hong, C. H., "Finite Element Approach to Rotor Blade Modeling," Journal of the American Helicopter Society, Vol. 32, No. 1, Jan. 1987, pp. 60-67.

53. Bauchau, O. A. and Hong, C. H., "Nonlinear Composite Beam Theory," Journal of Applied Mechanics, Vol. 55, March 1988, pp. 156-163.

54. Bauchau, O. A., Coffenberry, B. S., Rehfield, L. W., "Composite Box Beam Analysis Theory and Experiments," Journal of Reinforced Plastics and Composites, Vol. 6, Jan. 1987, pp. 25-35.

55. Rosen, A., Loewy, R. G. and Mathew, M. B., "Nonlinear Analysis of Pretwisted Rods Using 'Principal Curvature Transformation' Part I: Theoretical Derivation," AIAA Journal, Vol. 25, No. 3, March 1987, pp. 470-478.

56. Rosen, A. and Rand, O., "A General Model of the Dynamics of Moving and Rotating Rods," Computers and Structures, Vol. 21, No. 3, 1985, pp. 543-561.

57. Rosen, A. and Rand, O., "Numerical Model of the Nonlinear Behavior of Curved Rods," Computers and Structures, Vol. 22, No. 5, 1986, pp. 785-799.

58. Stemple, A. D. and Lee, S. W., "Finite-Element Model for Composite Beams with Arbitrary Cross-Sectional Warping," AIAA Journal, Vol. 26, No. 12, Dec. 1988, pp. 1512-1520.

59. Smith, E. C. and Chopra, I., "Formulation and Evaluation of an Analytical Model for Composite Box-Beams," Journal of the American Helicopter Society, Vol. 36, July 1991, pp. 23-35.

60. Hodges, D. H., "Finite Rotation and Nonlinear Beam Kinematics," Vertica, Vol. 11, No. 1/2, 1987, pp. 297-307.

61. Hinnant, H. E. and Hodges, D. H., "Nonlinear Analysis of a Cantilever Beam," AIAA Journal, Vol. 26, No. 12, Dec. 1988, pp. 1521-1527.

62. Hodges, D. H., "A Mixed Variational Formulation Based on Exact Intrinsic Equations for Dynamics of Moving Beams," International Journal of Solids and Structures, Vol. 26, No. 11, 1990, pp. 1253-1273.

63. Rehfield, L. W., Atilgan, A. R. and Hodges, D. H., "Nonclassical Behavior of Thin-Walled Composite Beams with Closed Cross Sections," Journal of the American Helicopter Society, Vol. 35, May 1990, pp. 42-50.

64. Berdichevskii, V. L., "Variational-Asymptotic Method of Constructing a Theory of Shells," PMM, Vol. 43, No. 4, 1979, pp. 664 - 687.

65. Danielson, D. A. and Hodges, D. H., "Nonlinear Beam Kinematics by Decomposition of the Rotation Tensor," Journal of Applied Mechanics, Vol. 54, June 1987, pp. 258-262.

66. Cesnik, C. E. S., Sutyrin, V. G. and Hodges, D. H., "A Refined Composite Beam Theory Based on the Variational-Asymptotical Method," Paper No. AIAA 93-1616-CP, Proceedings, 34th Structures, Structural Dynamics, and Materials Conference, La Jolla, California, April 1993, pp. 2710-2720.

67. Cesnik. C. E. S., Sutyrin, V. G. and Hodges, D. H., "Refined Theory of Twisted and Curved Composite Beams: The Role of Short-Wavelength Extrapolation," Proc. 35th Structures, Structural Dynamics and Materials Conference, Hilton Head, SC, April 1994.

68. Cesnik. C. E. S., Sutyrin, V. G. and Hodges, D. H., "Stiffness Constants for Composite Beams Including Large Initial Twist and Curvature Effects," Proc. 36th Structures, Structural Dynamics and Materials Conference, New Orleans, LA, April 1995.

69. Cesnik, C. E. S. and Hodges, D. H., "VABS: A New Concept for Composite Rotor Blade Cross-Sectional Modeling," Proc. 51st Annual Forum of the American Helicopter Society, Fort Worth, TX, May 1995.

70. Cesnik. C. E. S., Hodges, D. H., Popescu, B and Harursampath, D., "Composite Beam Cross-Sectional Modeling Including Obliqueness and Trapeze Effects," Proc. 37th Structures, Structural Dynamics and Materials Conference, Salt Lake City, Utah, April 1996.

71. Kosmatka, J. B., "Extension, Bending, and Torsion of Anisotropic Beams with Initial Twist," Paper No. 89-1364-CP. Proceedings, 30th Structures, Structural Dynamics, and Materials Conference, Mobile, Alabama, April 1989, pp. 911-920.

72. Kosmatka, J. B. and Friedmann, P. P., "Vibration Analysis of Composite Turbopropellers Using a Nonlinear Beam-Type Finite-Element Approach," AIAA Journal, Vol. 27, No. 11, Nov. 1989, pp. 1606-1614.

73. Kosmatka, J. B. and Dong, S. B., "Saint-Venant Solutions for Prismatic Anisotropic Beams," International Journal of Solids and Structures, Vol. 28, No. 7, 1991, pp. 917-938.

74. Kosmatka, J. B., "Extension-Bend-Twist Coupling Behavior of Nonhomogeneous Anisotropic Beams with Initial Twist," AIAA Journal, Vol. 30, No. 2, Feb. 1992, pp. 519-527.

75. Kosmatka, J. B., "Flexure-Torsion Behavior of Prismatic Beams, Part I: Section Properties via Power Series," AIAA Journal, Vol. 31, No. 1, Jan. 1993, pp. 170-179.

76. Rand, O., "Theoretical Modeling of Composite Rotating Beams," Vertica, Vol. 14, No. 3, 1990, pp. 329-343.

77. Rand, O., "Periodic Response of Thin-Walled Composite Helicopter Rotor Blades," Journal of the American Helicopter Society, Vol. 36, Oct. 1991, pp. 4-11.

78. Rand, O., "Nonlinear Analysis of Orthotropic Beams of Solid Cross-Sections," To appear in the Journal of Composite Structures.

79. Kalfon, J. P. and Rand, O., "Nonlinear Analysis of Composite Thin-Walled Helicopter Blades," Proc. 48th Annual Forum of the American Helicopter Society, Washington, D.C., 1992, pp. 1465-1478.

80. Chandra, R. and Chopra, I., "Vibration Characteristics of Composite I-Beams with Elastic Couplings Under Rotation," Proceeding, 47th Annual Forum of the American Helicopter Society, Phoenix, Arizona, May, 1991.

81. Whitney, J. M and Pagano, N. J., "Shear Deformation in Heterogeneous Anisotropic Plates," Journal of Applied Mechanics, Vol. 37, 1970, pp. 1031-1036.

82. Reissner, E., "On Finite Deflections of Anisotropic Laminated Elastic Plates," International Journal of Solids and Structures, Vol. 22, No. 10, 1986, pp. 1107-1115.

83. Kosmatka, J. B., "A Reliable Six-Node Triangular Plate/Shell Element for the Analysis of Laminated Composite Structures," Paper No. AIAA 88-2319. Proceedings, 29th Structures, Structural Dynamics, and Materials Conference, Williamsburg, Virginia, April 1988, pp. 911-920.

84. Bhumbla, R., Kosmatka, J. B. and Reddy, J. N., "Free Vibration Behavior of Spinning Shear-Deformable Plates Composed of Composite Materials," AIAA Journal, Vol. 28, No. 11, Nov. 1990, pp. 1962-1970.

85. Bhumbla, R. and Kosmatka, J. B., "Stability of Spinning Shear-Deformable Laminated Composite Plates," Journal of Sound and Vibration, Vol. 163, No. 1, 1993, pp. 83-99.

86. Rehfield, L. W. and Valisetty, R. R., "A Simple, Refined Theory for Bending and Stretching of Homogeneous Plates," AIAA Journal, Vol. 22, No. 1, Jan. 1984, pp. 90-95.

87. Valisetty, R. R. and Rehfield, L. W., "A Theory for Stress Analysis of Composite Laminates," AIAA Journal, Vol. 23, No. 7, July 1985, pp. 1111-1117.

88. Atilgan, A. R. and Hodges, D. H., "On the Strain Energy of Laminated Composite Plates," International Journal of Solids and Structures, Vol. 29, No. 20, 1992, pp. 2527-2543.

89. Lee, B. W., Sutyrin, V. G. and Hodges, D. H., "A Variable-Order Laminated Plate Theory Based on the Variational-Asymptotical Method," Paper No. AIAA 93-1617-CP, Proceedings, 34th Structures, Structural Dynamics, and Materials Conference, La Jolla, California, April 1993, pp. 2721-2732.

90. Hodges, D. H., Atilgan, A. R. and Danielson, D. A., "A Geometrically Nonlinear Theory of Elastic Plates," Journal of Applied Mechanics, Vol. 60, March 1993, pp. 109-116.

91. Lo, K. H., Christensen, R. M. and Wu. E. M., "A Higher-Order Theory of Plate Deformation, Part 2: Laminated Plates," Journal of Applied Mechanics, Vol. 44, Dec. 1977, pp. 669-676.

92. Reddy, J. N., "A Simple Higher-Order Theory for Laminated Composite Plies," Journal of Applied Mechanics, Vol. 51, Dec. 1984, pp. 745-752.

93. Reddy, J. N., Energy and Variational Principles in Applied Mechanics, John Wiley and Sons, New York, 1984.

94. Reddy, J. N., "A General Non-Linear Third-Order Theory of Plates with Moderate Thickness," International Journal of Non-Linear Mechanics, Vol. 25, No. 6, 1990, pp. 677-686.

95. Khdeir, A. A. and Reddy, J. N., "Analytical Solutions of Refined Plate Theories of Cross-Ply Composite Laminates," Journal of Pressure Vessel Technology, Vol. 113, Nov. 1991, pp. 570-578.

96. Murakami, H., "Laminated Composite Plate Theory with Improved In-Plane Responses," Journal of Applied Mechanics, Vol. 53, Sep. 1986, pp. 661-666.

97. Toledano, A. and Murakami, H., "A Composite Plate Theory for Arbitrary Laminate Configurations," Journal of Applied Mechanics, Vol. 54, March 1987, pp. 181-189.

98. Toledano, A. and Murakami, H., "A Higher-Order Laminated Plate Theory with Improved In-Plane Responses," International Journal of Solids and Structures, Vol. 23, No. 1, 1987, pp. 111-131.

99. Cho, M. and Parmerter, R. R, "An Efficient Higher Order Plate Theory for Laminated Composites," Composite Structures, Vol. 20, 1992, pp. 112-123.

100. Cho, M. and Parmerter, R. R, "Efficient Higher Order Composite Plate Theory for General Lamination Configurations," AIAA Journal, Vol. 31, No. 7, July 1993, pp. 1299-1306.

101. Gu, H. and Chattopadhyay, A., "A New Higher Order Plate Theory in Modeling Delamination Buckling of Composite Laminates," AIAA Journal, Vol. 32, No. 8, Aug. 1994, pp. 1709-1716.

101. Robbins, D. H. and Reddy, J. N., "Modelling of Thick Composites Using a Layerwise Laminate Theory," International Journal for Numerical Methods, Vol. 36, 1993, pp. 655-677.

102. Chattopadhyay, A. and Gu. H., "Exact Elasticity Solution for Buckling of Composite Laminates," Composite Structures, Vol. 34, No. 3, 1996, pp. 291-299.

102. Chattopadhyay, A. and Gu. H., "Modeling of Delamination Buckling in Composite Cylindrical Shells with a New Higher-Order Theory," Composite Science and Technology, Vol. 54, 1995, pp. 223-232.

105. MacNeal, R. H., ed., "The NASTRAN Theoretical Manual," NASA SP 221 (06), January 1981.

106. Srinivas, S. and Rao, A. K., "Bending, Vibration and Buckling of Simply Supported Thick Orthotropic Rectangular Plates and Laminates," International Journal of Solids and Structures, " Vol. 6, 1970, pp. 1463-1481.

107. MacBain, J. C., "Vibratory Behavior of Twisted Cantilevered Plates," Journal of Aircraft, Vol. 12, No. 4, April 1975, pp. 343-349.

108. Barton, M. V., "Vibration of Rectangular and Skew Cantilever Plates," Journal of Applied Mechanics, Vol. 18, June 1951, pp. 120-134.

109. McGee, O. G. and Leissa, A. W., "Three-Dimensional Free Vibrations of Thick Skewed Cantilevered Plates," Journal of Sound and Vibration, Vol. 144, No. 2, 1991, pp. 305-322.

110. Chandra, R., Stemple, A. D. and Chopra, I., "Thin-Walled Composite Beams Under Bending, Torsional and Extensional Loads," Journal of Aircraft, Vol. 27, No. 7, July 1990, pp. 619 - 626.

111. Smith, R. L., "Closed Form Equations for the Lift, Drag, and Pitching-Moment Coefficients of Airfoil Sections in Subsonic Flow," NASA TM 78492

112. Talbot, P. D., "Propeller Performance Program Using Blade Element Momentum Theory," Draft Working Paper, NASA Ames Research Center, September 1989.

113. Felker, F. F., Young, L. A. and Signor, D. B., "Performance and Loads Data from a Hover Test of a Full-Scale Advanced Technology XV-15 Rotor," NASA TM-86854, January 1986.

114. Arrington, W. L., Kumpel, M., Marr, R. L., and McEntire, K. G.., "XV-15 Tilt Rotor Research Aircraft Flight Test Data Report," NASA CR 177406, June 1985.

115. Corrigan, J. and Schillings, J., "Empirical Model for Stall Delay Due to Rotation," *Proc. of the AHS Aeromechanics Specialists Conference*, San Francisco, January 19-21, 1994.

116. Glauert, H., The Elements of Airfoil and Airscrew Theory, Cambridge University Press, Second Edition, 1948.

117. Gessow, A. and Myers, G. C., Jr., Aerodynamics of the Helicopter, College Park Press, 1952.

118. Tsai, S. W. and Wu, E. M., "A General Theory of Strength for Anisotropic Materials," *Journal of Composite Materials*, **5**, pp. 58-80, 1971.

119. Kreisselmeier, A. and Steinhauser, R., "Systematic Control Design by Optimizing a Vector Performance Index," *Proc.* of IFAC Symposium on Computer Aided Design of Control Systems, Zurich, Switzerland, August 1979, pp. 113-117.

120. Haftka, R. T., Gürdal, Z. and Kamat, M. P., Elements of Structural Optimization, Kluwer Academic Publishers, Dordrecht, The Netherlands, 1990.

121. Fadel, G. M., Riley, M. F. and Barthelemy, J. M., "Two Point Exponential Approximation method for Structural Optimization," *Structural Optimization*, Vol. 2., 1990, pp117-224.

122. Walsh, J. L., Young, K. C, Pritchard, J. I., Adelman, H. M.. and Mantay, W., "Multilevel Decomposition Approach to Integrated Aerodynamic/Dynamic/ Structural Optimization of Helicopter Rotor Blades," *Proc.* of the American Helicopter Society Aeromechanics Specialists Conference, San Francisco, Jan. 1994.

123. Thomas, H. L., Vanderplaats, G. N., Shyy, Y-K, "A Study of Move Limit Adjustment Strategies in the Approximation Concepts Approach to Structural Synthesis," *Proc.* 4th AIAA/USAF/NASA/OAI Symposium on Multidisciplinary Analysis and Optimizations, Cleveland, OH, September 1992. AIAA Paper No. 92-4750-CP.

124. Agarwal, B. D and Broutman, L. J., Analysis and Performance of Fiber Composites, John Wiley and Sons, Inc., 1990, p. 437.

Appendix A

Coordinate System Relations

The transformation between the untwisted global coordinate system and the rotated coordinate system is expressed as follows.

$$\begin{Bmatrix} X' \\ Y' \\ Z' \end{Bmatrix} = \begin{bmatrix} 1 & 0 & 0 \\ 0 & \cos\theta & \sin\theta \\ 0 & -\sin\theta & \cos\theta \end{bmatrix} \begin{Bmatrix} X \\ Y \\ Z \end{Bmatrix} \tag{A1}$$

The two unswept wall coordinate systems are written in terms of the two beam coordinate systems as

$$\begin{Bmatrix} x_i \\ y_i \\ z_i \end{Bmatrix} = \begin{Bmatrix} X_i \\ Y_i + Y_{o_i} \\ Z_i + Z_{o_i} \end{Bmatrix}, \tag{A2}$$

and

$$\begin{Bmatrix} x_i^* \\ y_i^* \\ z_i^* \end{Bmatrix} = \begin{Bmatrix} X_i' \\ Y_i' + Y_{o_i}' \\ Z_i' + Z_{o_i}' \end{Bmatrix}, \tag{A3}$$

where the global coordinate system (X_i, Y_i, Z_i) is written with the subscript 'i' to indicate the fact that Y_i is always aligned with the reference (untwisted) width of the individual walls. Similarly, the rotated coordinate system (X_i', Y_i', Z_i') is always aligned such that Y_i' is parallel to the rotated width of the individual wall. This notation is adopted so that the relationship between the global and local coordinate systems can be expressed using only a single set of equations. The quantities, Y_{o_i}, Z_{o_i}, Y_{o_i}' and Z_{o_i}' correspond to distances from the axis of rotation to the edge of the individual walls within which the wall coordinate systems are defined. Finally, the relationship between the local, swept and twisted coordinate system and the local, unswept and twisted coordinate system is written as

$$\begin{Bmatrix} \chi_i \\ \eta_i \\ \zeta_i \end{Bmatrix} = \begin{Bmatrix} x_i^* \\ y_i^* \\ z_i^* - z_{o_i}^* \end{Bmatrix}, \tag{A4}$$

where $z^*_{o_i}$ is the offset between the swept and unswept coordinate systems. Note that in the horizontal walls (i = 1 and 3), this offset is zero. Using Eqns. A1 - A4, the local wall, twisted coordinate system is written as

$$\begin{Bmatrix} \chi_i \\ \eta_i \\ \varsigma_i \end{Bmatrix} = \begin{bmatrix} 1 & 0 & 0 \\ 0 & \cos\theta & \sin\theta \\ 0 & -\sin\theta & \cos\theta \end{bmatrix} \begin{Bmatrix} x_i \\ y_i - Y_{o_i} \\ z_i - Z_{o_i} \end{Bmatrix} + \begin{Bmatrix} 0 \\ Y'_{o_i} \\ Z'_{o_i} + z^*_{o_i} \end{Bmatrix}. \tag{A5}$$

It must be noted that in the above relationship, both θ and $z^*_{o_i}$ are functions of x and vary along the span. The Jacobian matrix between the local untwisted and local twisted coordinate systems is then expressed as

$$\mathbf{J} = \begin{bmatrix} \frac{\partial\chi}{\partial x} & \frac{\partial\eta}{\partial x} & \frac{\partial\zeta}{\partial x} \\ \frac{\partial\chi}{\partial y} & \frac{\partial\eta}{\partial y} & \frac{\partial\zeta}{\partial y} \\ \frac{\partial\chi}{\partial z} & \frac{\partial\eta}{\partial z} & \frac{\partial\zeta}{\partial z} \end{bmatrix} = \begin{bmatrix} 1 & (\zeta - Z'_o)\frac{\partial\theta}{\partial x} & -(\eta - Y'_o)\frac{\partial\theta}{\partial x} + \frac{\partial z^*_o}{\partial x} \\ 0 & \cos\theta & -\sin\theta \\ 0 & \sin\theta & \cos\theta \end{bmatrix}, \tag{A6}$$

where the subscript 'i' has been omitted for convenience. It is seen from Eqn. A6, that the determinant of the Jacobian is equal to one.

Appendix B

Strain definitions

The zeroth order inplane strains in the absence of pre-twist are defined as follows.

$$\begin{Bmatrix} e_1^o \\ e_2^o \\ e_6^o \end{Bmatrix} = \begin{Bmatrix} u_{o,\chi} \\ v_{o,\eta} \\ u_{o,\eta} + v_{o,\chi} \end{Bmatrix} \tag{B1}$$

The first order inplane strains are

$$\begin{Bmatrix} \kappa_1^1 \\ \kappa_2^1 \\ \kappa_6^1 \end{Bmatrix} = \begin{Bmatrix} -w_{o,\chi\chi} + \psi_{x,\chi} \\ -w_{o,\eta\eta} + \psi_{y,\eta} \\ -2w_{o,\chi\eta} + \psi_{x,\eta} + \psi_{y,\chi} \end{Bmatrix}, \tag{B2}$$

and the third components of the inplane strain are

$$\begin{Bmatrix} \kappa_1^3 \\ \kappa_2^3 \\ \kappa_6^3 \end{Bmatrix} = -\frac{4}{3h^2} \begin{Bmatrix} \psi_{x,\chi} \\ \psi_{y,\eta} \\ \psi_{x,\eta} + \psi_{y,\chi} \end{Bmatrix}. \tag{B3}$$

The zeroth and the second order components of the out-of-plane strains are defined as follows.

$$\begin{Bmatrix} e_4^o \\ e_5^o \end{Bmatrix} = \begin{Bmatrix} \psi_y \\ \psi_x \end{Bmatrix} \tag{B4}$$

$$\begin{Bmatrix} \kappa_4^2 \\ \kappa_5^2 \end{Bmatrix} = -\frac{4}{h^2} \begin{Bmatrix} \psi_y \\ \psi_x \end{Bmatrix} \tag{B5}$$

The additional non-zero inplane strain components due to pre-twist are written as

$$\begin{Bmatrix} \mu_1^o \\ \mu_6^o \end{Bmatrix} = -\begin{Bmatrix} Z'_o u_{o,\eta} + (\eta - Y'_o)(-w_{o,\chi} + \psi_x) \\ Z'_o v_{o,\eta} + (\eta - Y'_o)(-w_{o,\eta} + \psi_y) + w_o \end{Bmatrix}, \tag{B6}$$

$$\begin{Bmatrix} \mu_1^1 \\ \mu_6^1 \end{Bmatrix} = \begin{Bmatrix} u_{o,\eta} - Z'_o(-w_{o,\chi\eta} + \psi_{x,\eta}) \\ v_{o,\eta} - Z'_o(-w_{o,\eta\eta} + \psi_{y,\eta}) \end{Bmatrix}, \tag{B7}$$

$$\begin{Bmatrix}\mu_1^2\\ \mu_6^2\end{Bmatrix} = \begin{Bmatrix}-w_{o,\chi\eta} + \psi_{x,\eta} + \frac{4}{h^2}(\eta - Y_o')\psi_x\\ -w_{o,\eta\eta} + \psi_{y,\eta} + \frac{4}{h^2}(\eta - Y_o')\psi_y\end{Bmatrix}, \tag{B8}$$

$$\begin{Bmatrix}\mu_1^3\\ \mu_6^3\end{Bmatrix} = \begin{Bmatrix}\frac{4}{3h^2}Z_o'\psi_{x,\eta}\\ \frac{4}{3h^2}Z_o'\psi_{y,\eta}\end{Bmatrix}, \tag{B9}$$

$$\begin{Bmatrix}\mu_1^4\\ \mu_6^4\end{Bmatrix} = \begin{Bmatrix}-\frac{4}{3h^2}\psi_{x,\eta}\\ -\frac{4}{3h^2}\psi_{y,\eta}\end{Bmatrix}. \tag{B10}$$

The non-zero out-of-plane components of the strain due to presence of pre-twist are written as

$$\mu_5^o = v_o - Z_o'w_{o,\eta}, \tag{B11}$$

$$\mu_5^1 = \psi_x, \tag{B12}$$

$$\mu_5^3 = -\frac{4}{3h^2}\psi_x, \tag{B13}$$

Finally, the nonzero strain terms associated with sweep (which exist only in the vertical walls) are written as follows.

$$\begin{Bmatrix}\vartheta_1^o\\ \vartheta_6^o\end{Bmatrix} = \begin{Bmatrix}-w_{o,\chi} + \psi_x\\ -w_{o,\eta} + \psi_y\end{Bmatrix} \tag{B14}$$

$$\begin{Bmatrix}\vartheta_1^2\\ \vartheta_6^2\end{Bmatrix} = -\frac{4}{h^2}\begin{Bmatrix}\psi_x\\ \psi_y\end{Bmatrix} \tag{B15}$$

Next, the convergence study is conducted in the natural frequencies and a nondimensional natural frequency parameter, λ_i, is used where

$$\lambda_i = \omega_i \sqrt{\frac{\rho h L^4}{D}}, \tag{C.1}$$

$$D = Eh^3/12(1-\nu^2). \tag{C.2}$$

The natural frequency parameters, λ_i, for the first six modes are presented for a range of mesh sizes in Figs C.2 - C.7. From these figures it is again noted that although convergence can be achieved with only one or two chordwise elements, often the converged results are significantly different from the actual results. This is particularly evident in the third flapping mode (Fig. C.5), the second torsional mode (Fig. C.6) and the first plate mode (Fig. C.7). For a mesh with three or more chordwise elements, convergence is achieved very quickly. In general for such chordwise discretizations, convergence is achieved with 10 - 12 spanwise elements.

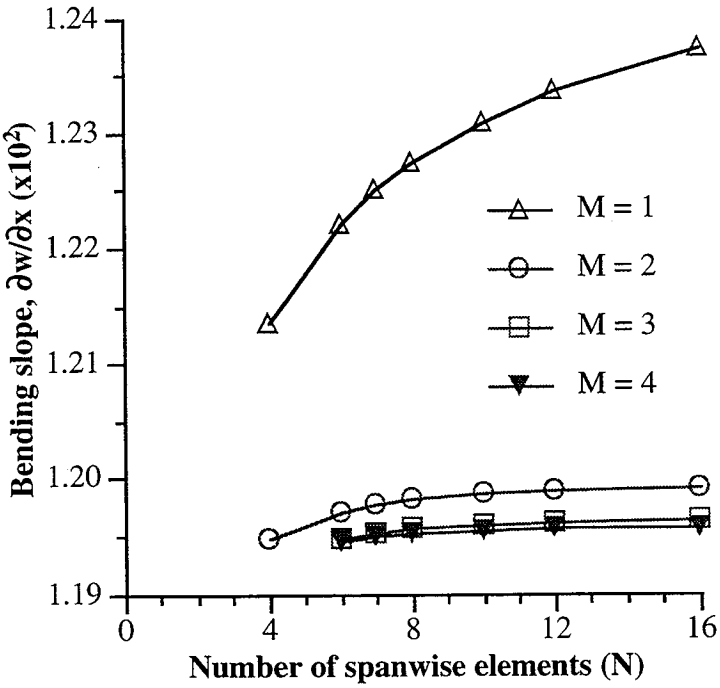

Fig. C.1 Bending slope for 30° twisted, isotropic plate subjected to 1 lb. tip bending load.

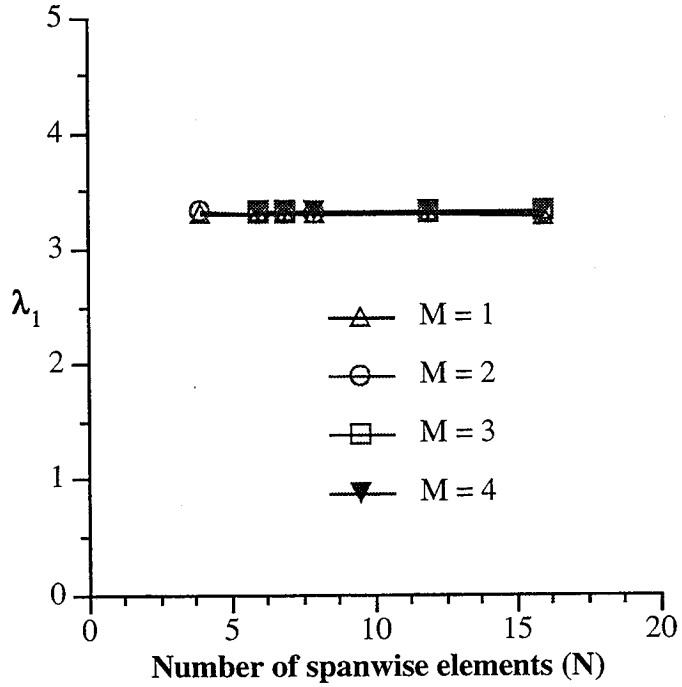

Fig. C.2 Natural frequency parameter for the first flapping mode; 30° twisted, isotropic plate.

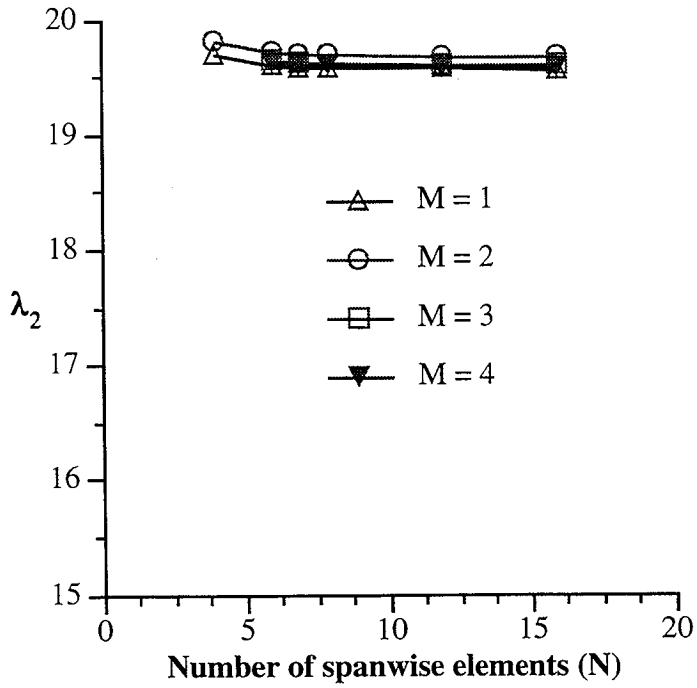

Fig. C.3 Natural frequency parameter for the second flapping mode; 30° twisted, isotropic plate.

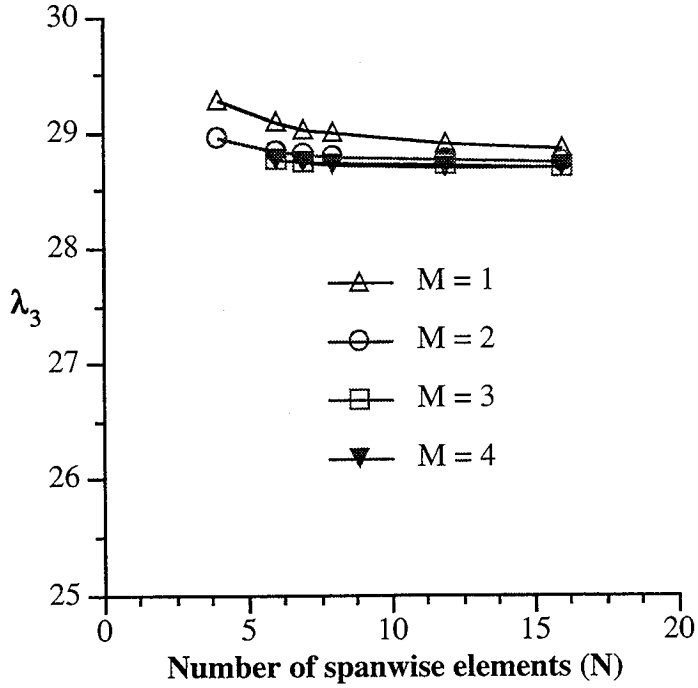

Fig. C.4 Natural frequency parameter for the first torsion mode; 30° twisted, isotropic plate.

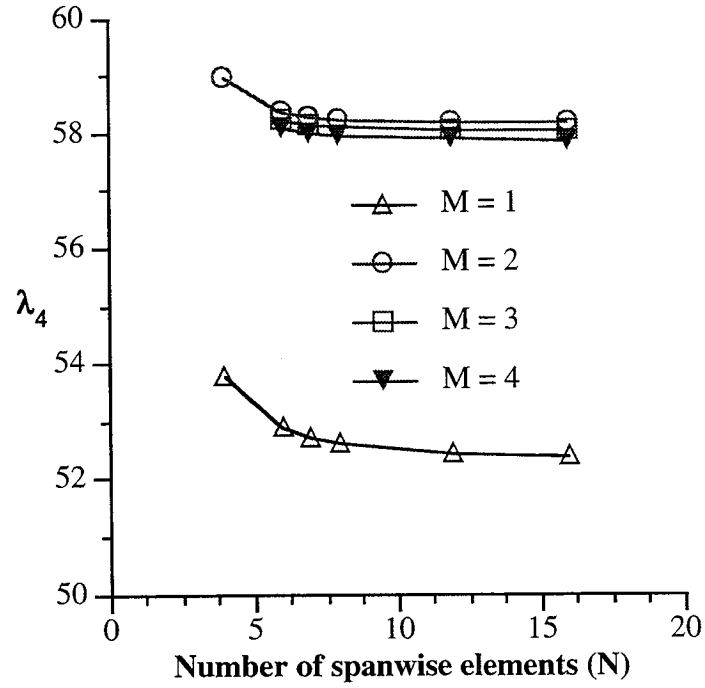

Fig. C.5 Natural frequency parameter for the third flapping mode; 30° twisted, isotropic plate.

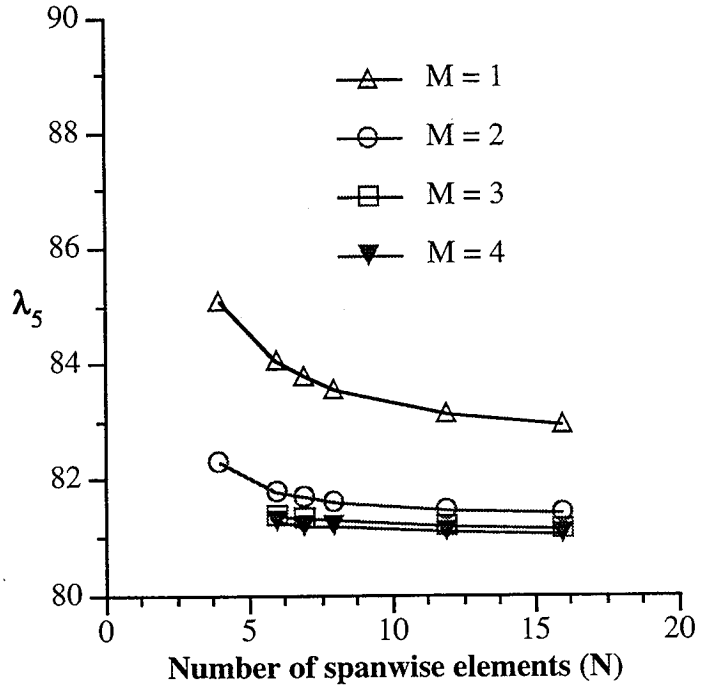

Fig. C.6 Natural frequency parameter for the second torsion mode; 30° twisted, isotropic plate.

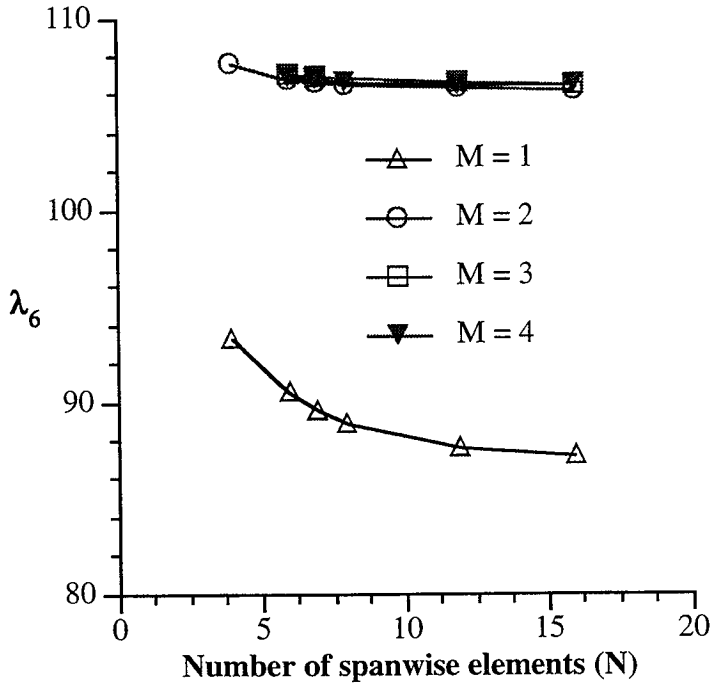

Fig. C.7 Natural frequency parameter for the first plate mode; 30° twisted, isotropic plate.

C.2 Composite, 45° symmetric beam

Convergence tests for the beam are performed for both a static case with a 1 lb. tip bending load as well as for the first several natural frequencies. The beam used for this study is a symmetric 45° graphite/epoxy composite beam for which the properties are listed in Table. C.2. Figures C.8 - C.10 present the static deflections at the tip. It must be noted that the values presented in these figures represent the average value for the entire cross section. Since the developed theory does not rely on reducing the beam behavior to one-dimensional parameters, values of the cross-sectional flap, lag and twist are not explicitly calculated. However, in case of thin-walled beams, the values in each of the walls are very close to each other, therefore, in such cases the approximation of the cross-sectional twist being equal to average twist of all four walls is valid. It is observed in Figs. C.8 - C.10 that convergence is achieved with approximately 10 spanwise elements. More importantly it is noted that this convergence is independent of the number of chordwise elements. This is largely due to the fact that the beam is decomposed into the individual walls which make up the beam and as a result, a single chordwise element in each wall results in four chordwise element for the beam cross section.

Table C.2 Details of symmetric 45° composite beams

Flanges		**Webs**	
Top	Bottom	Left	Right
$[45^\circ]_6$	$[45^\circ]_6$	$[45^\circ/-15^\circ]_3$	$[45^\circ/-45^\circ]_3$

Material Properties

$E_L = 20.59 \times 10^6$ p.s.i., $E_T = 1.42 \times 10^6$ p.s.i.,
$G_{LT} = 0.89 \times 10^6$ p.s.i., $\nu_{LT} = 0.42$.

Beam Dimensions

Length = 30 in., width = 0.953 in., depth = 0.53 in.,
ply thickness = 0.005 in, number of plies = 6,
wall thickness = 0.030 in.

Similar trends are observed in the convergence rates of the natural frequencies which are presented in Figs. C.11 - C.17. It is seen from these figures that once again convergence is independent of the number of chordwise elements. For the lower frequencies, convergence is obtained with approximately 10 spanwise elements. For the higher frequencies, convergence is a little slower and although the results are not truly converged with 10 spanwise elements, they are quite close to the converged values.

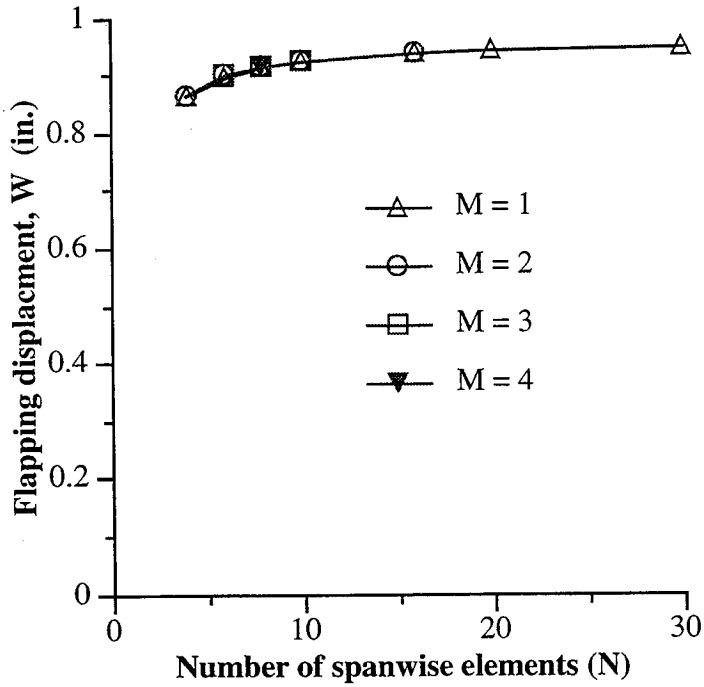

Fig. C.8 Flapping displacement for 45° symmetric beam subjected to 1 lb. tip bending load.

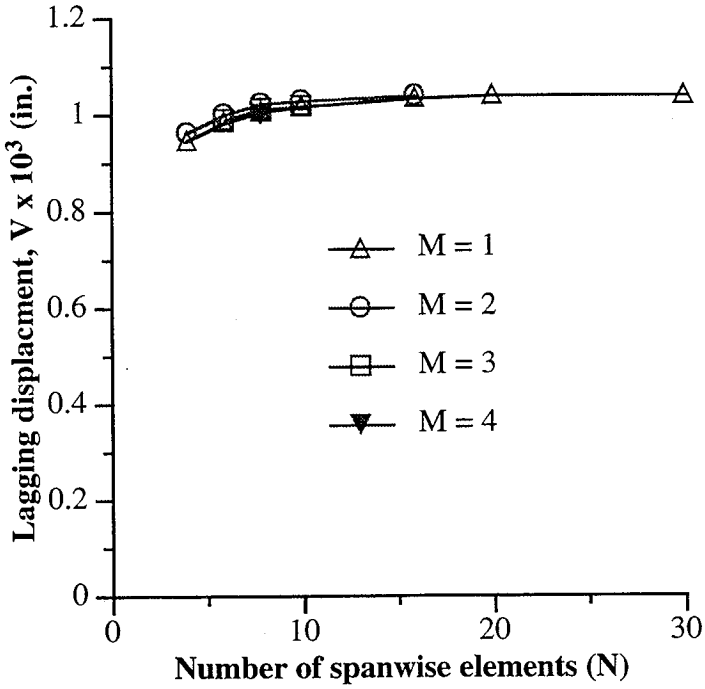

Fig. C.9 Lagging displacement for 45° symmetric beam subjected to 1 lb. tip bending load.

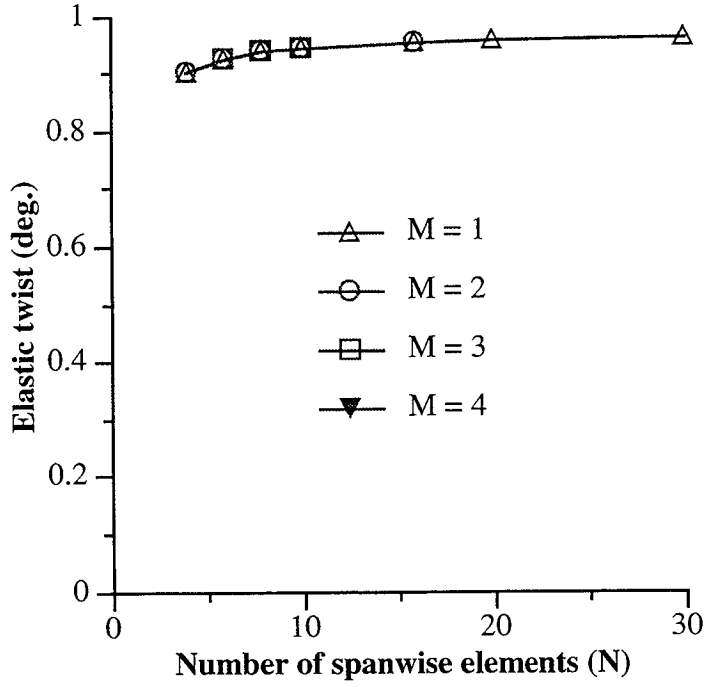

Fig. C.10 Elastic twist for 45° symmetric beam subjected to 1 lb. tip bending load.

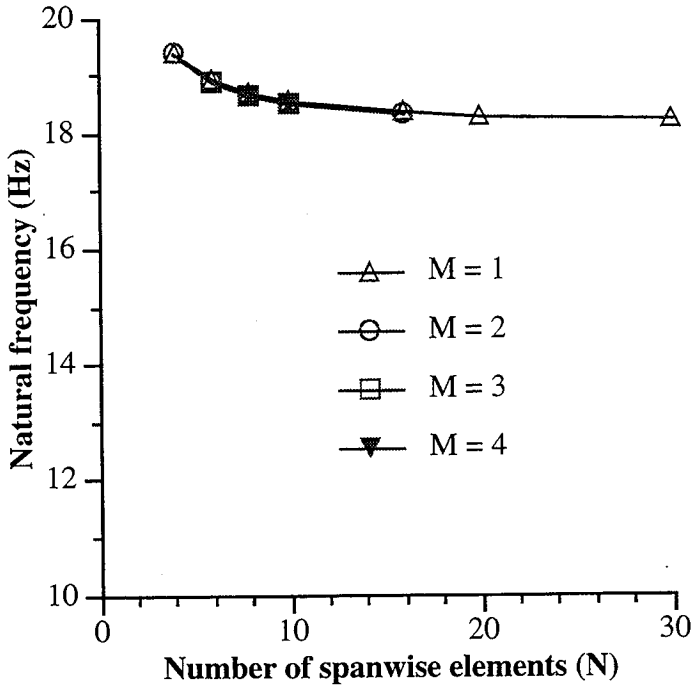

Fig. C.11 First flapping frequency (1F) of 45° symmetric beam.

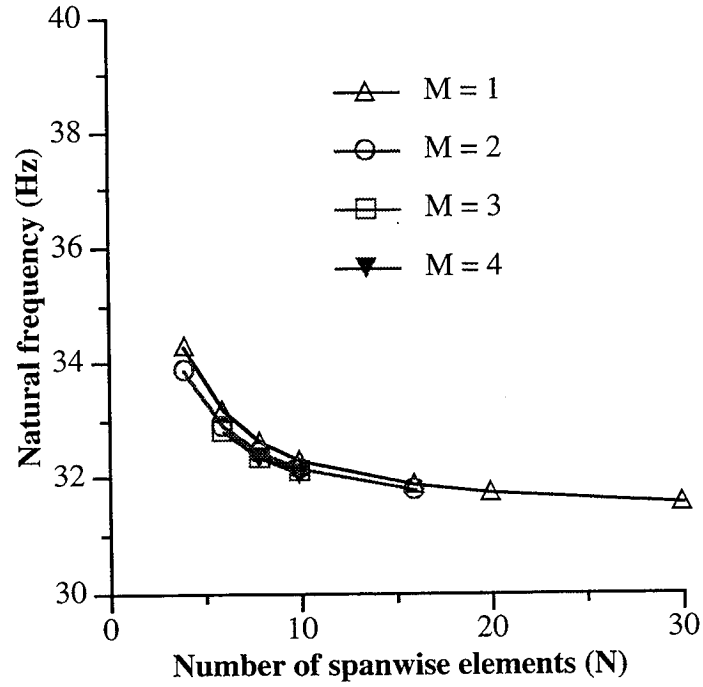

Fig. C.12 First lagging frequency (1L) of 45° symmetric beam.

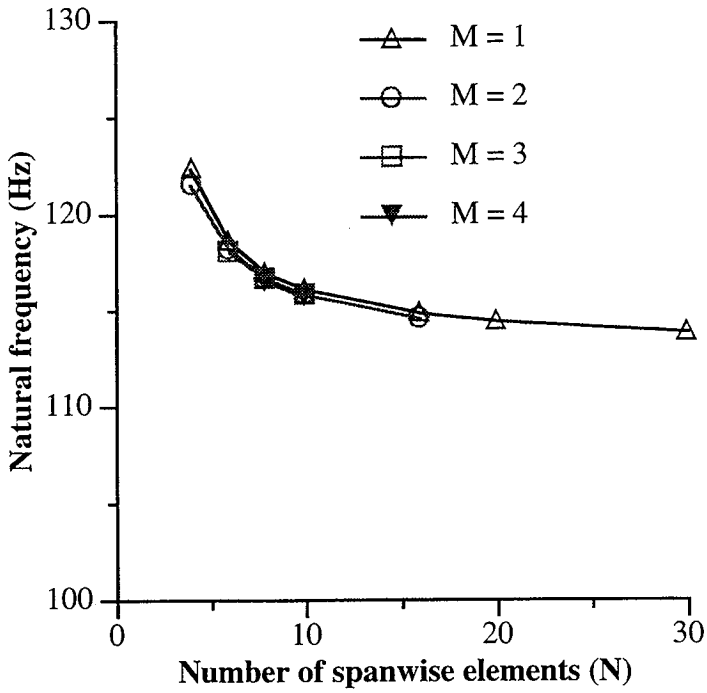

Fig. C.13 Second flapping frequency (2F) of 45° symmetric beam.

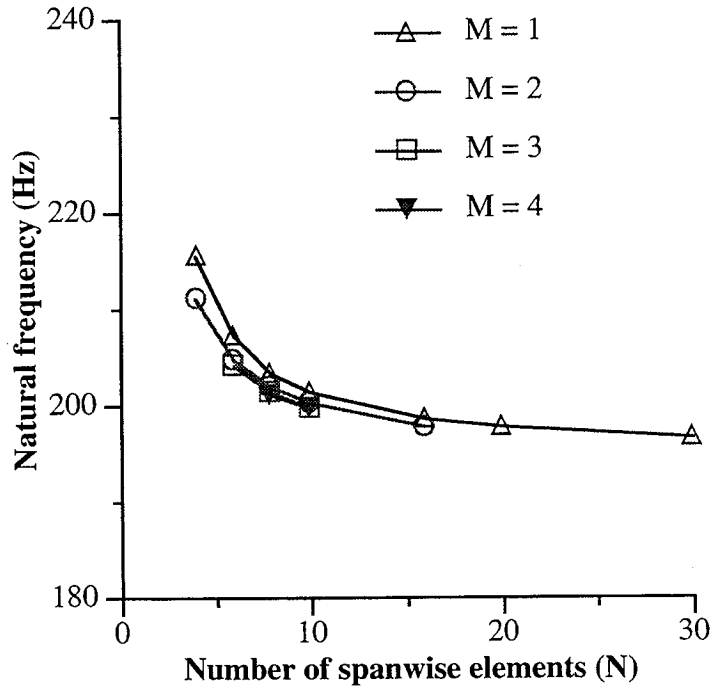

Fig. C.14 Second lagging frequency (2L) of 45° symmetric beam.

REPORT DOCUMENTATION PAGE

Form Approved
OMB No. 0704-0188

1. AGENCY USE ONLY *(Leave blank)*	2. REPORT DATE	3. REPORT TYPE AND DATES COVERED
	October 1996	Contractor Report

4. TITLE AND SUBTITLE

A New Higher-Order Composite Theory for Analysis and Design of High Speed Tilt-Rotor Blades

5. FUNDING NUMBERS

NAG2-771

6. AUTHOR(S)

Thomas Robert McCarthy

7. PERFORMING ORGANIZATION NAME(S) AND ADDRESS(ES)

Arizona State University
Department of Mechanical and Aerospace Engineering
P. O. Box 876106
Tempe, AZ 85287-6106

8. PERFORMING ORGANIZATION REPORT NUMBER

A-962808

9. SPONSORING/MONITORING AGENCY NAME(S) AND ADDRESS(ES)

National Aeronautics and Space Administration
Washington, DC 20546-0001

10. SPONSORING/MONITORING AGENCY REPORT NUMBER

NASA CR-196703

11. SUPPLEMENTARY NOTES

Point of Contact: Sesi Kottapalli, Ames Research Center, MS T12-B, Moffett Field, CA 94035-1000
(415) 604-3092

12a. DISTRIBUTION/AVAILABILITY STATEMENT

Unclassified-Unlimited
Subject Category – 05

12b. DISTRIBUTION CODE

13. ABSTRACT ***(Maximum 200 words)***

A higher-order theory is developed to model composite box beams with arbitrary wall thicknesses. The theory, based on a refined displacement field, represents a three-dimensional model which approximates the elasticity solution. Therefore, the cross-sectional properties are not reduced to one-dimensional beam parameters. Both inplane and out-of-plane warping are automatically included in the formulation. The model accurately captures the transverse shear stresses through the thickness of each wall while satisfying all stress-free boundary conditions. Several numerical results are presented to validate the present theory. The developed theory is then used to model the load carrying member of a tilt-rotor blade which has thick-walled sections. The composite structural analysis is coupled with an aerodynamic analysis to compute the aeroelastic stability of the blade. Finally, a multidisciplinary optimization procedure is developed to improve the aerodynamic, structural and aeroelastic performance of the tilt-rotor aircraft. The Kreisselmeier-Steinhauser function is used to formulate the multiobjective function problem and a hybrid approximate analysis is used to reduce the computational effort. The optimum results are compared with the baseline values and show significant improvements in the overall performance of the tilt-rotor blade.

14. SUBJECT TERMS	15. NUMBER OF PAGES
Tilt-rotor, Composite beam theory, Multidisciplinary optimization	184
	16. PRICE CODE A09

17. SECURITY CLASSIFICATION OF REPORT	18. SECURITY CLASSIFICATION OF THIS PAGE	19. SECURITY CLASSIFICATION OF ABSTRACT	20. LIMITATION OF ABSTRACT
Unclassified	Unclassified		